Investigation of the effect of process parameters on bond strength of thermoplastic composite rings manufactured using fiber laser

Mehran Eimanlou

A Thesis

In

The Department

Of

Mechanical, Industrial, and Aerospace Engineering

Presented in Partial Fulfillment of the Requirements

For the Degree of

Master of Applied Science (Mechanical Engineering) at

Concordia University

Montréal, Québec, Canada

February 2018

CONCORDIA UNIVERSITY

School of Graduate Studies

This is to certify that the thesis prepared

By: Mehran Eimanlou

Entitled: Investigation of process parameters on bond strength of thermoplastic composite rings manufactured using fiber laser

and submitted in partial fulfillment of the requirements for the degree of

Master of Applied Science (Mechanical Engineering)

complies with the regulations of the University and meets the accepted standards with respect to originality and quality.

Signed by the final Examining Committee:

Dr. Mamoun Medraj	Chair
Dr. Suong Van Hoa	Examiner
Dr. Saifur Rahaman	Examiner
Dr. Mehdi Hojjati	Supervisor

Approved by:

Dr. Martin D. Pugh	Chair of the Department of Mechanical, Industrial and Aerospace Engineering
Dr. Amir Asif	Dean of Faculty of Engineering and Computer Science

Date: _____

Abstract

The competitive advantage of an automated, true out-of-autoclave composite manufacturing process is realized. Decades of research has been directed toward enhancing technologies and processes such as the automated fiber placement AFP of carbon fiber reinforced thermoplastic CFRTP composite materials. One of the latest technological advancement in the AFP process is the introduction of continuous-wave high power fiber lasers. Together with the development of thermoplastic material systems, it is now possible to in-situ consolidate parts at efficient rates with promising quality. A ring manufacturing setup capable of in-situ consolidation of thermoplastic composite tape is developed for the following study. A set of collimating focusing and beam shaping lens are used to transform a Gaussian beam of a high power continuous-wave fiber laser to a square, top-hatted beam, with uniform intensity profile at the desired working distance. 20-Ply CFRTP PEEK rings, 152 mm in diameter, are manufactured for the experimental studies. Design of Experiments using Taguchi approach is employed to investigate the effect of major process parameters on the mechanical properties of the rings. Effect of placement rate, laser power, and compaction force is evaluated against ILSS of samples. Influence of parameters and a near-optimum point within the processing window is obtained. Compaction force beyond a certain limit is deemed to have the least impact amongst others on ILSS. An optimum set of parameters are then used to produce rings at a 50% higher placement rate compared to those made using hot-gas-torch process. To investigate further increase in placement rates variation of ILSS with laser power is studied for up to 152 mm/s. A decline in ILSS is observed with the increase in placement rate as the degree of intimate contact diminutions. The use of a conformable roller, with transparent to NIR light material, sufficient hardness, and internal cooling is necessary to maintain the degree of intimate contact at higher placement rates. To enhance the degree of autohesion a larger rectangular spot size could be used. However, it is shown that the thermal efficiency decreases as the spot size widens away from the nip point. Finally, the measurement of temperature at nip point suggests that the bonding of up to two preceding layers may be affected at each pass and that to keep a constant nip point temperature for the winding-like manufacturing process the laser power shall vary.

Keywords: automated fiber placement, fiber laser, carbon-fiber reinforced thermoplastic composites, process parameter optimization, Inter Laminar Shear Strength.

Acknowledgment

I wish to express my sincere gratitude to my supervisor, Dr. Mehdi Hojjati, for his continuous support, and aspiring guidance throughout this project.

I'm very grateful to Mr. Dainius Juras, Mr. Gilles Huard, Mrs. Maureen Thuringer, Mr. Jeffery Fortin Simpson, Mr. Dominic Ng, and my dear friends Mr. Vincent Mooney-Chopin, Mr. Mohamed El-Sawah, and Mr. Haqueem Sapuan. Without their precious support, and generous help it would not be possible to conduct this research.

A special gratitude goes out to Mr. Graham Carr: Vice-President Research and Graduate Studies, Dr. Amir Asif: Dean of Faculty of Engineering and Computer Science, and Dr. Martin Pugh: Professor and Chair of MIAE Department at Concordia University for providing the funding for the work.

I would also thank the examination committee for reading this thesis and providing critical comments.

Last but by no means least my deepest appreciation is expressed to my family for their encouragement, unconditional support, and the inspiration they gave me to persist forward during my study.

Table of Contents

List of Figures vi
List of Tables vii
Chapter 1: Introduction 1
Chapter 2: Literature Review 6
2.1 Material Systems 6
2.2 AFP/ATL Processing Heat Source 7
2.3 Thermoplastic Processing Model 9
2.3.1 Intimate Contact 9
2.3.2 Autohesion 13
2.3.3 Bonding 14
2.4 Crystallinity 15
2.5 Void Dynamics 16
2.6 Experimental Investigation 17
2.7 Mechanical Testing 20
2.8 Laser-assisted End-Effector Design 21
2.9 Research Objectives 22
Chapter 3: Design of The Ring Manufacturing Apparatus 23
3.1 Concept Generation 24
3.2 System Level Design 28
3.3 Sub-assembly Design 29
3.3.1 Mandrel Assembly 29
3.3.2 Actuator & Roller Assembly 31
3.3.3 Clutch and Tape Guide System 33
3.3.4 Pneumatic Valves and Regulators 35
3.3.5 Microcontroller 36
3.3.6 Thermal Camera 37
3.3.7 Infrared Cameras 37
3.3.8 Laser System and Chiller 38
3.3.9 Collimator Module 39

3.4 Overall Assembly 41
Chapter 4: Experimental investigation 42
4.1 DOE Parameter Optimization 43
4.1.1 Optimization Using the Taguchi Approach 43
4.1.2 Identification of the Process Window 44
4.1.3 Experimental Procedure 44
4.1.4 Reproducibility of Data 47
4.1.5 Studying the Factor Effects 47
4.1.6 Relative Influence of Parameters 49
4.1.7 Expected Response at Optimum Condition 50
4.2 Laser-Assisted vs. Hot Gas Torch Heating 50
4.2.1 Experimental Procedure 50
4.2.2 ILSS at Optimum Condition: laser heating vs. HGT 52
4.3 Increased Placement Rate and Its Effect on the Bond Strength 54
4.3.1 Experimental Procedure 54
4.3.2 Photomicrograph Analysis 57
4.3.3 Laser Power vs. Placement Rate at Optimum ILSS 58
4.4 Laser Light Delivery and Effectiveness 59
4.4.1 Diffractive Optical Element Lens 59
4.4.2 Experimental Procedure 59
4.4.3 Gaussian Beam Profile Intensity Variation 62
4.5 Silicone roller: Material Characterization and Fabrication 65
4.5.1 Silicone Roller Fabrication 66
4.5.2 Material Characterization Using Spectrophotometry 67
4.6 Nip Point Temperature Measurement 68
4.6.1 Experimental Procedure 68
4.6.2 Interpretation of the Thermocouple Measurements 72
Chapter 5: Conclusion and Future Work 74
References 77
Appendix A: Microcontroller code 82
Appendix B: Photo Micrograph 84
Appendix C: Spectrophotometry Result 87
Appendix D: list of items made available through cloud storage 88

LIST OF FIGURES

FIGURE 1: LASER-HEATING PLACEMENT SETUP 2
FIGURE 2: PARAMETERS INVOLVED IN THE LASER HEATING PLACEMENT PROCESS 4
FIGURE 3: PEEK, PEKK, AND PPS POLYMER BACKBONE 7
FIGURE 4: EVALUATION OF NUMEROUS AFP/ATL HEATING MECHANISMS [17] 8
FIGURE 5: LEE AND SPRINGER IDENTICAL RECTANGULAR MODEL AND 1-D FLOW MODEL [19] 10
FIGURE 6: YANG AND PITCHUMANI CANTOR SET FRACTAL SURFACE MODEL 12
FIGURE 7: REAL APC-2/PEEK TAPE ROUGHNESS PROFILE MESH [22] 12
FIGURE 8: AUTOHESION OR HEALING OF SEMI-CRYSTALLINE THERMOPLASTICS IN THE TAPE LAYUP PROCESS 13
FIGURE 9: CONCENTRIC VOID-RESIN SHELL MODEL [37] 17
FIGURE 10: REFLECTION OF INCIDENT LASER BEAM OF THE TAPE SURFACE AND SUBSTRATE [11] 19
FIGURE 11: HORIZONTAL SHEAR LOAD DIAGRAM FOR CURVED BEAMS – [ASTM D2344/D2344M - 00] 20
FIGURE 12: AUTOMATED DYNAMICS LIFT (PHOTO COURTESY FROM AUTOMATED DYNAMICS WEBSITE) [49] 22
FIGURE 13: END-EFFECTOR: CONCEPT 1 25
FIGURE 14: END-EFFECTOR CONCEPT 2 26
FIGURE 15: END-EFFECTOR CONCEPT 3 27
FIGURE 16: SYSTEM INTERACTION DIAGRAM 28
FIGURE 17: MANDREL ASSEMBLY 30
FIGURE 18: ACTUATOR AND ROLLER ASSEMBLY 32
FIGURE 19: CLUTCH AND TAPE GUIDE ASSEMBLY 34
FIGURE 20: PNEUMATIC ROUTING, VALVES, ACTUATORS, AND REGULATORS 35
FIGURE 21: MICROCONTROLLER BOX 36
FIGURE 22: MICROCONTROLLER DIAGRAM 37
FIGURE 23: MONITORING THE PROCESS USING FOUR INFRARED CAMERAS 38
FIGURE 24: YLS2000 LASER SYSTEM PLUGGED TO D50 WELDING HEAD 39
FIGURE 25: IPG STANDALONE D50 LASER WELDING HEAD 40
FIGURE 26: FINAL CAD MODEL OF THE RING MANUFACTURING SET-UP 41
FIGURE 27: DEFINITION OF TAGUCHI PROCESS 43
FIGURE 28: SHORT BEAM SHEAR TEST COUPON AND SETUP 46
FIGURE 29: MAIN EFFECT PLOTS: MEANS OF MEANS 48
FIGURE 30: MAIN EFFECT PLOT: MEANS OF SIGNAL TO NOISE RATIO 48
FIGURE 31: LEFT: LASER-HEATING SETUP; RIGHT: HOT GAS TORCH SETUP 51
FIGURE 32: TRIAL 7: MATERIAL "B" PROCESSED WITH FIBER LASER 53
FIGURE 33: TRAIL 9: MATERIAL "A" PROCESSED WITH HGT 53
FIGURE 34: TRAIL 10: MATERIAL "B" PROCESSED WITH HGT 53
FIGURE 35: ILSS RESULT FOR LASER POWER VS. PLACEMENT RATE 56
FIGURE 36: SBS SPECIMEN PREPARED FOR MICROGRAPH IMAGING 57
FIGURE 37: PLOT OF LASER POWER [W] VS PLACEMENT RATE [MM/S] AT OPTIMUM ILSS 58
FIGURE 38: COLLIMATING AND BEAM SHAPING MODULE FOR THE RING MANUFACTURING SETUP 60
FIGURE 39: TRANSFORMATION OF A GAUSSIAN BEAM (LEFT) TO TOP-HATTED BEAM (RIGHT) 60
FIGURE 40: CONVERSION SCREEN SURFACE TEMPERATURE AT VARIOUS DISTANCES FROM THE WORKING DISTANCE 61
FIGURE 41: GAUSSIAN BEAM AXIAL PROPAGATION AND THE LOCATION OF TWO UNIQUE, FOCUSED SPOTS 63
FIGURE 42: SILICONE ROLLER VS. RIGID STEEL ROLLER INSTALLED ON THE LASER HEATING SETUP 66
FIGURE 43: SILICONE ROLLER MOLDED AROUND A STEEL ROLLER CORE 67
FIGURE 44: TC CONNECTION TO OMB-DAQ-2408 [58] FIGURE 7 69
FIGURE 45: THERMOCOUPLE AND DAQ UNIT SET-UP 69

FIGURE 46: NIP TEMPERATURE MEASUREMENT - SILICONE ROLLER- 220W- 117 MM/S –TC 15HZ APART 70
FIGURE 47: NIP TEMPERATURE MEASUREMENT - STEEL ROLLER- 220W- 117 MM/S –TC 15HZ APART – TRIAL 1 70
FIGURE 48: NIP TEMPERATURE MEASUREMENT - STEEL ROLLER- 220W- 117 MM/S –TC 15HZ APART – TRIAL 2 71
FIGURE 49: NIP TEMPERATURE MEASUREMENT- STEEL ROLLER- 260W- 117 MM/S –TC 15HZ APART 71
FIGURE 50: RESPONSE TIME OF BARE WIRE THERMOCOUPLES [59].....72
FIGURE 51: NIP TEMPERATURE MEASUREMENT – SILICONE VS. STEEL ROLLER 220W -117MM/S.....73

LIST OF TABLES

TABLE 1: LIST OF FACTORS AFFECTING THE OUTCOME OF THE LASER-ASSISTED PLACEMENT PROCESS.....4
TABLE 2: MANDREL ASSEMBLY MAIN COMPONENTS DESCRIPTION, FUNCTION, AND INTERACTION.....30
TABLE 3: ACTUATOR AND ROLLER ASSEMBLY MAIN COMPONENTS DESCRIPTION, FUNCTION, AND INTERACTION....33
TABLE 4: CLUTCH AND TAPE GUIDE ASSEMBLY DESCRIPTION, FUNCTION, AND INTERACTION.....34
TABLE 5: MICROCONTROLLER BOX MAIN COMPONENTS DESCRIPTION, FUNCTION, AND INTERACTION 36
TABLE 6: IPG WELDING HEAD MAIN COMPONENTS: PART DESCRIPTION, FUNCTION, AND INTERACTION 40
TABLE 7: LIST OF FACTOR AND THEIR CORRESPONDING LEVELS AS INPUT OF L16 ORTHOGONAL ARRAY 45
TABLE 8: RESULT OF SBS TEST, STANDARD DEVIATION, AND COEFFICIENT OF VARIATION FOR ALL CONDITIONS....46
TABLE 9: AVERAGE EFFECTS OF FACTORS 48
TABLE 10: RINGS MANUFACTURED USING HGT AND FIBER LASER SOURCE HEATING 51
TABLE 11: RESULT OF ILSS FOR VARIOUS PLACEMENT RATES AND LASER POWER 55
TABLE 12: AXIAL POSITION OF THE LASER BEAM SPOT AWAY FROM THE WORKING DISTANCE.....61
TABLE 13: TEMPERATURES RECORDED FOR DIFFERENT RADIANCE PROFILES 62

CHAPTER 1: INTRODUCTION

Today automated placement of composite has found extensive application in aerospace and aeronautics industry with automotive catching up to the race. The demand for low cost, highly efficient manufacturing process is rising as cost competitiveness becomes an advantage, and production rates deem to increase; the benefits of fully automated placement technologies are realized.

Many aerospace OEMs are using fiber placement technology for their new products development and manufacturing including Bombardier Aerospace. One strip at a time, the rear pressure bulkhead of the CSeries fuselage is crafted using a pair of robots moving in a synchronized manner, meticulously placing a narrow tape on a curved mandrel. Design engineers take advantage of the anisotropic behavior of composites on the dome-shaped design to deliver yet lighter components. Through the use of AFP, higher productivity and lower manufacturing costs have been achieved. However the majority of AFP applications in the aerospace industry today is limited to pre-forming of thermoset based or dry-fiber composites. Upon pre-forming, these parts then need to be bagged, cured in an autoclave, de-bagged and trimmed; a process which despite producing good quality parts is time-consuming, costly, and requires a large capital. The use of autoclaves, therefore, remains as the major bottleneck in the manufacturing process of composite parts.

Thermoplastics, however, have a different chemical characteristic. Thermoplastics are referred to as “linear” polymers and do not require curing during consolidation as opposed to “cross-linkable” thermosets. Thermoplastics can be in-situ welded. Application of heat and local pressure allows dislocation of polymer chains and enables polymerization. Thermoplastics can be reprocessed, reshaped, and recycled. High-performance semi-crystalline PEEK, PEKK, and PPS composites, developed recently, offer better mechanical properties, higher service temperature, more resistance to chemical reactions, and infinite shelf life in comparison to conventional thermoset composites; making them an appealing material of choice for aerospace applications.

Automated placement is an in-situ consolidation process. The concept of in-situ consolidation is simple. Incoming impregnated tape once at contact with the substrate under

sufficient pressure and temperature above melting point consolidates, and crystallizes upon cooling at either controlled (heated mandrel [1] [2] [3]) or uncontrolled rate. To address the low production rate variety of heating mechanisms are developed: ultrasonic, direct flame, infrared heating and recently high power diode lasers, and flash lamps. A recent work reported placement rates as much as 400-mm/s and near autoclave properties for flat plates using laser-assisted process [4]. The drastic increase in placement rate mostly becomes possible with the use of large conformable rollers which extend the time material spends under pressure. The conformable rollers, often used, are large silicone rollers that are transparent to NIR light. However, a shortcoming of this setup is its ineffectiveness in processing high-curvature geometries. Moreover, void fraction of 4 to 5% is reported [3] [5]. A major challenge remains to attain aerospace-standard quality for complex parts with a large curvature at increased placement rates. For example, a cylindrical tail boom was manufactured using HGT AFP system at CONCOM with a 6.35-mm (½-inch) diameter steel roller to study the feasibility of the process. Less than 75-mm/s (3-in/s) disposition rate was used [6]; a placement rate which may not be economically attractive or would pace the production.

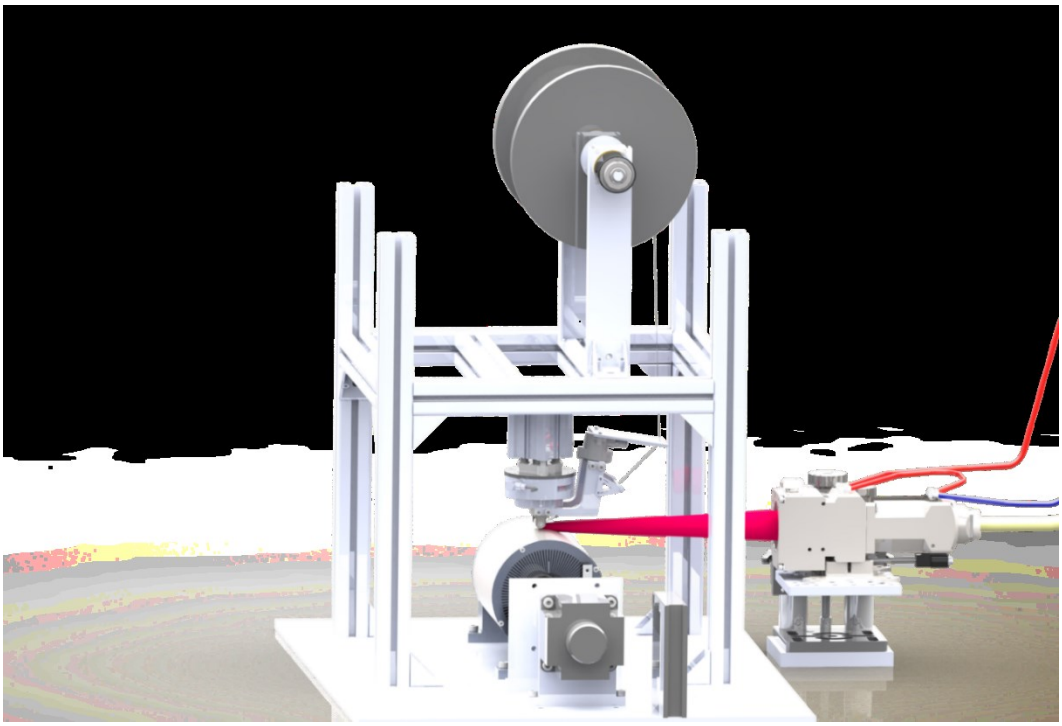

Figure 1: Laser-Heating Placement Setup

Moreover, the automated fiber placement is a form of additive manufacturing. Successive layers of a narrow tape are deposited once a time to construct the final part. As for all additive manufacturing processes, a major concern is to obtain uniform-quality parts which requires establishing a controlled, and a robust process. In the HGT heating process, the heat flux is difficult to control [6]. The main parameter affecting the heat flux is the volume flow rate of the nitrogen gas. It is not feasible to maintain a steady flow rate throughout the process. An unsteady flow rate of the nitrogen gas will vary the nip point temperature; since the optimum processing window is narrow, a slight variation in the nip point temperature will deteriorate the quality. On the other hand, the heat flux is controlled and sustained in the laser-heating process. Laser beams are spatial and temporal controlled. It is therefore expected to achieve more uniform quality parts made with laser-assisted process compared to that of HGT.

Another shortcoming of HGT process is the very inefficient convective heat transfer which makes the process less favorable for increased production rates. For a 75 mm placement rate, the nozzle temperature must be maintained as high as 975 degree Celsius to reach the processing temperature of PEEK tape at the nip point [6]. Further increase in the deposition rate aggravates the loss of energy resulting in the thermal deficiency. Due to the method of radiative heat transfer, the laser-assisted process is up to 80% more energy efficient. The fibers first absorb the heat from the emitted NIR light and then transfer it to the surrounding matrix through conduction.

The loss of energy, however, may occur during the amplification, delivery, and the processing of the beam. The beam delivered through fiber optic is extremely focused and must be expanded, to at least the width of the tape. The beam processing requires a set of collimating, focusing, and shaping optics which manipulate the inputted Gaussian beam to a rectangular, near-uniform irradiance density, top-hatted beam. About 5% to 10% of power loss may occur through optics. Moreover, it can be shown that the thermal efficiency is subject to the irradiated surface, its shape, and its distance from the focal point of the processed beam.

Overall the laser-assisted AFP process involves many parameters that affect the process outcome. Some of which are listed below.

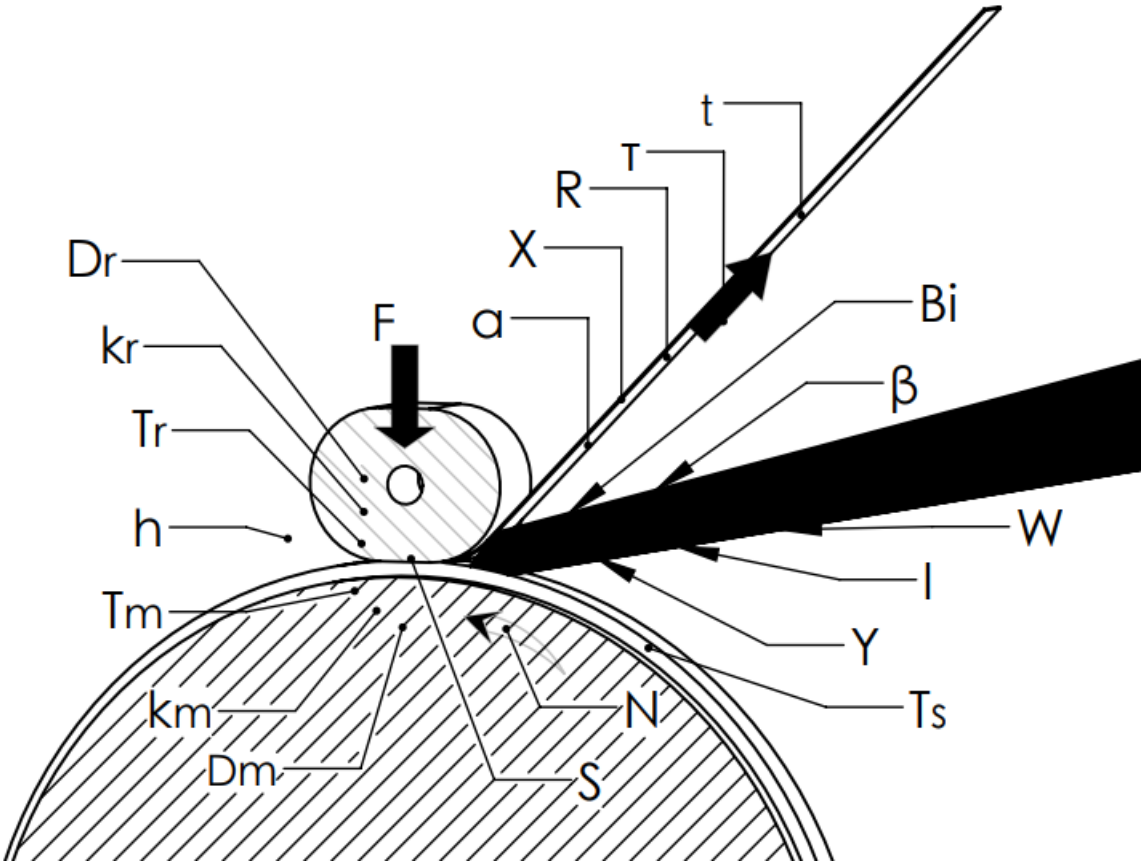

Figure 2: Parameters Involved in the Laser Heating Placement Process

Table 1: List of factors affecting the outcome of the laser-assisted placement process

Parameters Affecting Process Outcome			
F	Compaction Force	Y	Beam profile
S	Compaction Area	I	Beam intensity
D_r	Roller Diameter	W	Beam size and shape
k_r	Roller Thermal Conductivity	β	Beam angle
T_r	Roller interface Temperature	Bi	Spot position bias
h	Heat Transfer Coefficient	α	Incoming tape angle
T_s	Substrate Temperature	τ	Tape Tension
T_M	Mandrel Temperature	X	Tape impregnation quality
k_M	Mandrel Thermal Conductivity	R	Tape Surface Roughness
D_M	Mandrel Curvature	t_{tape}	Tape thickness
N	Placement Rate		

To obtain good quality parts the combination effect of the main process parameters must be studied. The work presented henceforth attempts to study and optimize the in-situ placement process of thermoplastic composite rings using laser heating such that both deposition rates and quality of the final product are improved in comparison to the HGT process.

CHAPTER 2: LITERATURE REVIEW

While the introduction of high power fiber lasers is recent, the application of laser technology in the placement process dates back to 1980's. Beyeler, Philips, and Guceri [7] investigated in-situ consolidation of thermoplastic tapes with an 80 Watt CO2 laser. Their findings, as well as later experimental works done by Agrawal et al. [8], Rosselli et al. [9] suggest a more uniform thermal profile with the application of wider beam with higher laser power is required for better consolidation. Mazumdar and Hoa [10] studied the effect of laser power, pressure, and feed-rate on bond strength with a similar CO_2 pulsed laser. They reported dominant effect of laser power and minimal effect of compaction force on the bond quality. In-situ consolidation modeling work by Grove [11] suggested poor crystallinity due to high cooling rates. Yousefpour and Ghasemi Nejhad [12] later proposed pre-heating of the tape below transition temperature Tg for enhanced laminate consolidation. By late 1990's however, due to lack of continuous-wave high power laser systems and popularity of hot-gas-torch, laser-assisted placement development work was stalled before being brought around a decade later.

Today, industries and scientific research bodies are boldly investing in the laser-assisted placement process. High power laser systems are commercially available up to 10 kW and even extended if needed. Application of uniform heat flux is feasible with the continuous-wave emission of the top-hatted beam. Moreover, engineering compaction pressure application is possible with the development of conformable rollers, made of silicone materials, transparent to 1064 nm NIR light. Hence recent work published by Compston and Stokes-Griffin [4] [5] report near autoclave inter-laminar shear strength are achieved for flat panels. However, reaching full consolidation with a robust process optimized for any size and shape geometry is yet to be realized.

2.1 Material Systems

Material system is the input to the process and is the most important process parameter. The manufacturing process of thermoplastic composites is affected dominantly by the viscosity of the resin, therefore making the impregnation the most critical phase in the processing of thermoplastics [13]. The characteristic of the tape, determined by its void content, fiber volume

fraction, the degree of fiber wet-out, uniformity, and surface roughness sets the potential of the process.

Solvent impregnated CFRTP matrix such as Polyethersulfone (PES) and Polyetherimide (PEI) were amongst the initial resin system developments. Advanced high performance, semi-crystalline thermoplastic matrix such as Polyetheretherketone (PEEK), Polyetherketoneketone (PEKK), and polyphenylene sulfide (PPS) were later developed for CFRTP and found a wide range of applications in the aerospace industry [13]. PEEK demonstrates relatively higher fracture toughness, higher service temperature; and is less prone to chemical reactions compared to amorphous polymers. However, due to its elevated T_g and viscosity, processing of PEEK demands the application of very localized heat and pressure. The aramid polymer backbones of PEEK, PEKK, and PPS are shown below.

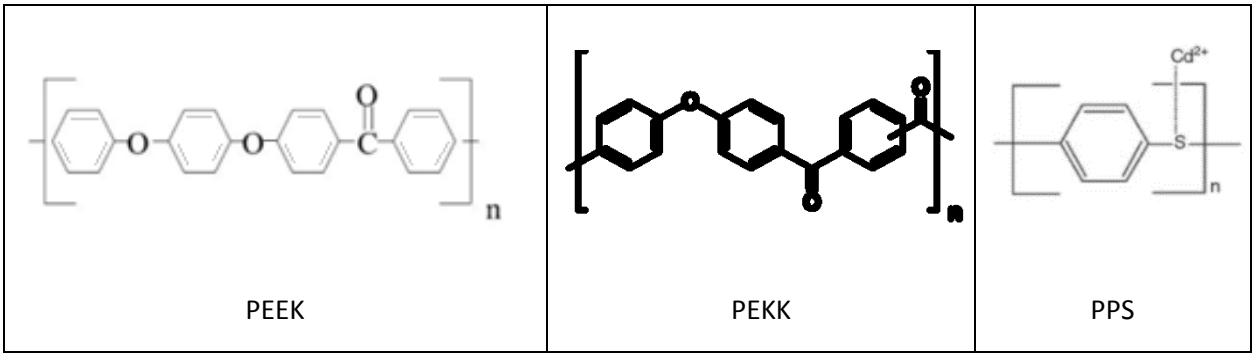

Figure 3: PEEK, PEKK, and PPS polymer backbone

Currently, CFRTP PEEK is the most popular material system in the aerospace AFP applications with PPS [7] [14], and PEKK [15] used less often. Regarding ATL and AFP tape systems, APC-2 CYTEC PEEK resin, and aerospace grade AS4 fibers are most commonly used. Other tape systems referred to in the literature are Hexcel HexTow IM6/PEEK, IM7/PEEK; TenCate Cetex AS4/PEEK; and more recently CF/PEEK tapes from Supreme [16]. The unidirectional tapes often used are 6.4-mm (¼-inch) to 51-mm (2.0-inch) in width and 0.13-mm (.005-inch) in thickness.

2.2 AFP/ATL Processing Heat Source

A significant pullback in the fiber placement in-situ process technology has been due to low production rates and below autoclave level quality. For the past three decades, researchers

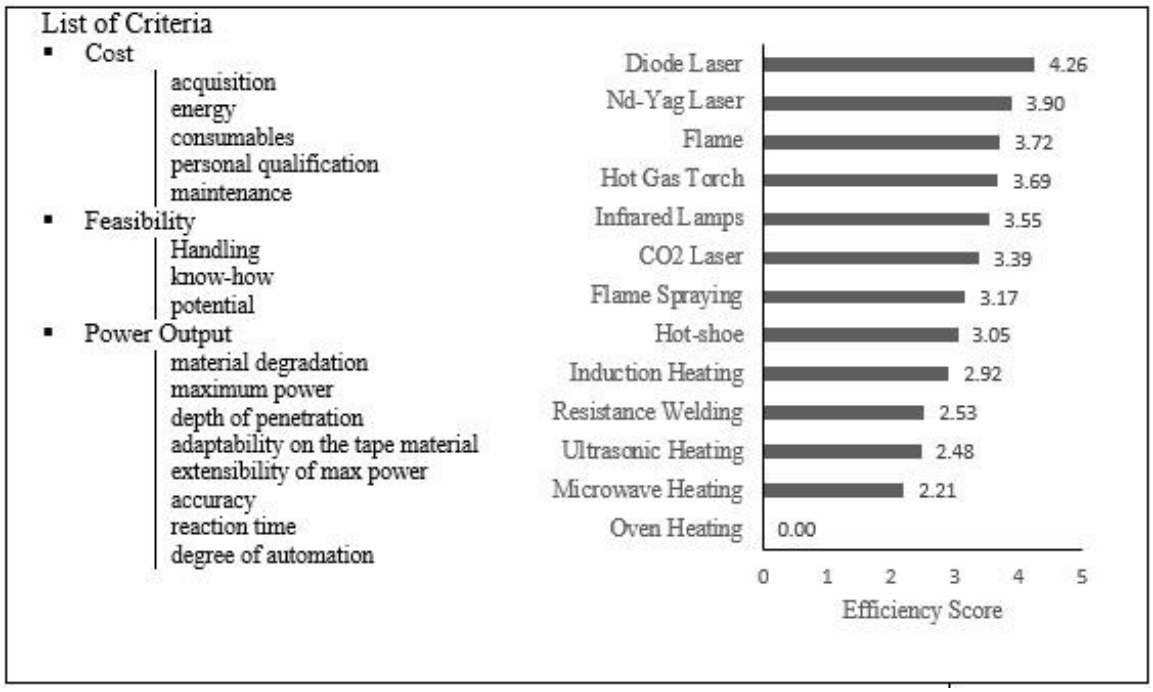

Figure 4: Evaluation of numerous AFP/ATL heating mechanisms [17]

have attempted to enhance the process and the material systems. Dozens of heating mechanisms and a numerous prepreg thermoplastic tape systems have been developed. Despite the recent advancement, the production rates and part quality is yet to be improved before commercializing the technology [17].

The concept of in-situ consolidation is simple. Incoming impregnated tape once at contact with the substrate under sufficient pressure and temperature above melting point consolidates, and crystallizes upon cooling at either controlled (heated mandrel [1] [2] [3]) or uncontrolled rate. To address the low production rate variety of heating mechanisms are developed: ultrasonic, direct flame, infrared heating and recently high power diode lasers, and flash lamps. A study done by P. Rinza and H. Schmitz uses criteria such as cost, feasibility, and power output, with higher weight given to more important parameters subjectively determined by experts, to rank numerous type of heating mechanism employed or studied for AFP/ATL. Laser-assisted AFP, specifically diode laser is rated to be the most efficient amongst 13 other heating mechanisms which are listed above. The efficiency of pulsed-heating flash lamps, such as the one developed by Xenon [18] in response to the safety hazards of laser-assisted heating, is yet to be explored.

2.3 Thermoplastic Processing Model

Lee and Springer presented a model of the thermoplastic composite manufacturing process. They described the process consisting of three main steps: Impregnation, consolidation, and crystallinity [19]. While impregnation is an uncontrolled parameter, consolidation and crystallinity can be controlled via the AFP process. The consolidation consists of two sub-processes: intimate contact and healing or autohesion. A good degree of intimate contact and healing is required to achieve better quality. Crystallinity also affects mechanical properties and is dependent on the thermal cycle and cooling rate above glass transition temperature. However, in most AFP applications the cooling rate is as high as 1000 ºC per minute. Parts produced with PEEK-based CFRTP tape systems will have a similar degree of crystallinity of 20% to 35%.

Both intimate contact and autohesion are a function of temperature, pressure, and time. At a given pressure, higher temperature and a longer time are required to achieve the optimum degree of intimate contact and bonding.

2.3.1 Intimate Contact

Inter-diffusion of polymers occurs only after the development of intimate contact. The intimate contact is measured using degree of intimate contact (D_{ic}), a term which was first introduced by Lee and Springer [19]. The general definition of D_{ic} is as follows:

$$D_{ic} = \frac{Surface\ in\ contact}{Total\ surface\ area} \tag{2.3.1}$$

The intimate contact development model is mostly dependent on the surface roughness characterization. The CFRTP PEEK tape has random irregularities on the surface. Since the tape is unidirectional, a 2D parameterization of irregularities is adequate. Two of the most known intimate contact development models are the identical rectangle model by Lee and Springer [19], and the fractal model by Yang and Pitchumani [20].

Lee and Springer's model is based on Dara and Loos model which describes the irregularities as statistically distributed rectangles with different height and width. Lee and springer simplified Dara and Loos surface model parameterization by assuming equally spaced

identical rectangles as shown in Figure 5. The simple parameterization further simplified implication of a flow model.

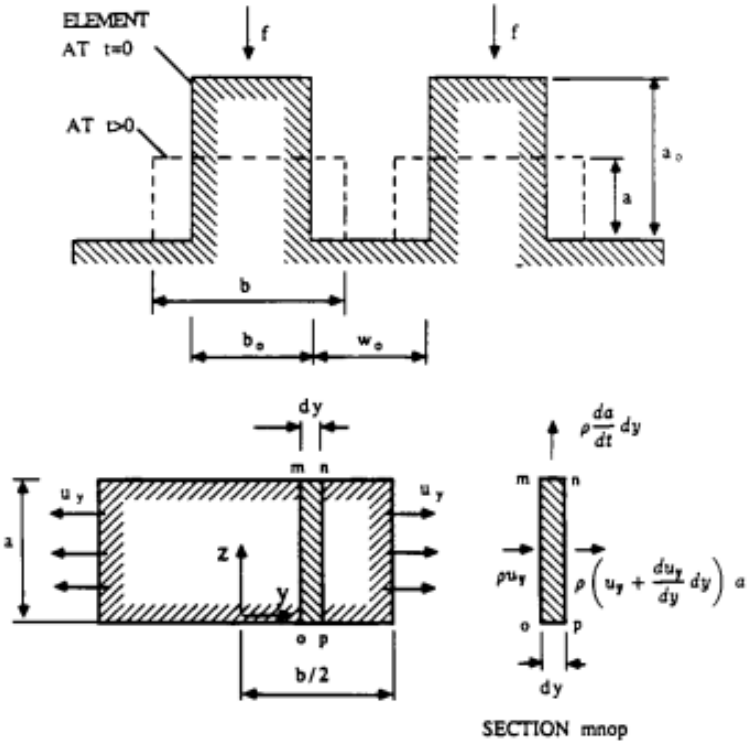

Figure 5: Lee and Springer Identical Rectangular Model and 1-D flow model [19]

A one-dimensional Newtonian flow model is proposed by Lee and Springer to simulate the squeezing effect of the asperities. The following expression of the degree of intimate contact is derived by applying the law of conservation of mass across a control volume of width dy, shown above, assuming a laminar flow, application of constant pressure, and temperature in isothermal condition [19]:

$$D_{ic} = \frac{1}{1+\frac{w_o}{b_o}}\left[1+\frac{5P_{app}}{\mu_{mf}}\left(1+\frac{w_o}{b_o}\right)\left(\frac{a_o}{b_o}\right)^2 t\right]^{\frac{1}{5}} \tag{2.3.2}$$

The above expression is a function of the applied pressure (P_{app}), temperature dependent matrix-fiber viscosity (μ_{mf}), time (t), and geometrical parameters (a_0, b_0, w_0) which are

determined experimentally. The time required to reach complete intimate contact, $D_{ic}$of unity, is therefore [19]:

$$t_{ic} = \frac{\mu_{mf}}{5P_{app}} \frac{1}{1+\frac{w_0}{b_0}} (\frac{b_0}{a_0})^2 [\left(1+\frac{w_0}{b_0}\right)^5 - 1] \tag{2.3.3}$$

Mantel and Springer extended the model for non-isothermal conditions in which the applied pressure and viscosity vary with time [21]:

$$D_{ic} = \frac{1}{1+\frac{w_o}{b_o}} [1 + 5\left(1+\frac{w_o}{b_o}\right)\left(\frac{a_o}{b_o}\right)^2 \int_0^{t_c} \frac{P_{app}}{\mu_{mf}} dt]^{\frac{1}{5}} \tag{2.3.4}$$

They further derived the above equation for the tape placement applications with rigid rollers of small contact area with an assumption that both temperature and applied pressure remain constant during the time of contact [21]:

$$D_{ic} = \frac{1}{1+\frac{w_o}{b_o}} [1 + 5\left(1+\frac{w_o}{b_o}\right)\left(\frac{a_o}{b_o}\right)^2 \frac{F}{\mu_{mf} V H_r}]^{\frac{1}{5}} \tag{2.3.5}$$

whereas F is the compaction force, V is the placement rate, and H_r is the width of the roller, or the tape, whichever the smaller.

Mantel later came up with an approximate version of the above expression in which he neglected the smaller first term compared to a much larger second term to arrive at the following:

$$D_{ic} = \frac{1}{w^*} [a^* \frac{F}{\mu_{mf} V H_r}]^{\frac{1}{5}} = R_c [\frac{F}{\mu_{mf} V H_r}]^{\frac{1}{5}} \tag{2.3.6}$$

$$w^* = 1 + \frac{w_o}{b_o} \tag{2.3.7}$$

$$a^* = 5w^* \left(\frac{a_o}{b_o}\right)^2 \tag{2.3.8}$$

$$R_c = \frac{a^{*\frac{1}{5}}}{w^*} \tag{2.3.9}$$

$$\mu_{mf} = 132.95(exp\frac{2969}{T(K)}) \tag{2.3.10}$$

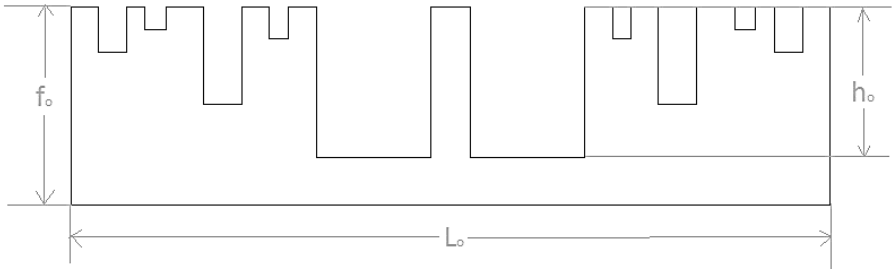

Figure 6: Yang and Pitchumani Cantor set Fractal Surface Model

Using micrograph images, Mantel determined surface asperity parameter coefficient $R_c = 0.29$ for CF/PEEK unidirectional tape. This coefficient has been adopted in several other works [16].

To present a more accurate model of the surface irregularities Yang and Pitchumani propose a Cantor set fractal model as opposed to the identical rectangular model shown below. Here it is assumed that the highest-order generation rectangle is squeezed without deformation of the lower-order generation. A complete intimate contact is achieved if all asperities have the same size of the largest repeating unit of the profile. The same 1-D Newtonian laminar squeeze flow model as Lee and Springer is assumed here.

Ultimately the degree of intimate contact was investigated using an FEA model with the real tape surface roughness model obtained from profilometer measurements [22]. The metrology indicated significant surface roughness on ACP-2/AS4 unidirectional tape. The squeeze flow is solved with Polyflow solver, and the surface geometry is meshed every ten iteration for convergence due to large deformations. The surface profile is shown below.

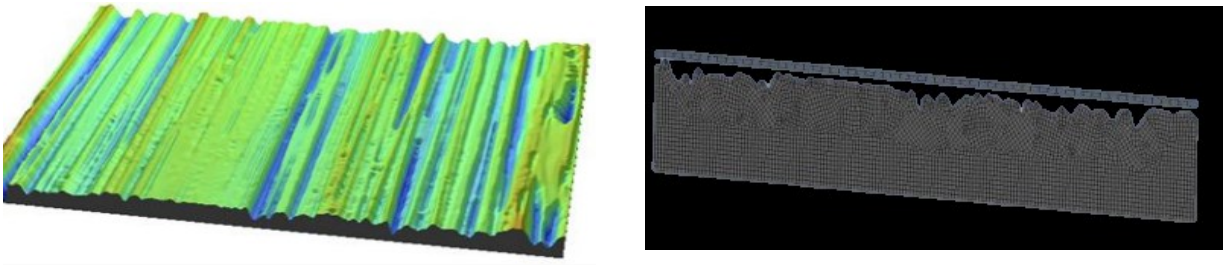

Figure 7: Real APC-2/PEEK tape roughness profile mesh [22]

The reported data showed good agreement with the Lee and Springer approximate model. The asperity coefficient R_c of 0.29 assumed by Mantel however, was found to be too smooth for APC-2/AS4 tape. R_c of 0.22 to 0.168 was suggested which better resembled the rougher tape surface profile.

2.3.2 Autohesion

Autohesion is the inter-diffusion of the polymer chains across two surfaces that have come into intimate contact. In semi-crystalline thermoplastics such as PEEK, the diffusion of molecules across the interface occurs upon heating the matrix beyond its melting temperature T_m.

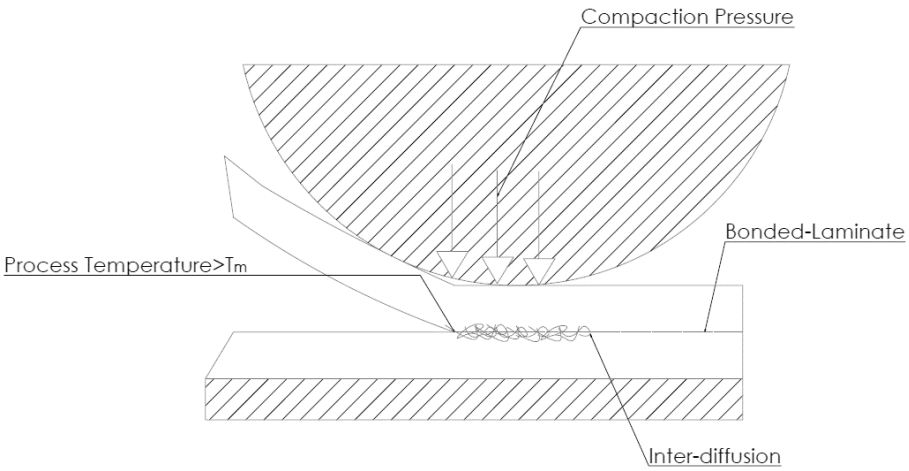

Figure 8: Autohesion or healing of semi-crystalline thermoplastics in the Tape Layup process

Degree of autohesion D_{au} increases with time and is characterized using the bond strength developed in an isothermal condition [19]:

$$D_h = \frac{S}{S_\infty} = (\frac{t}{t_r})^{\frac{1}{4}} \tag{2.3.11}$$

whereas S is the bond strength at time t and S_∞ is the ultimate bond strength at the reptation time t_r, which is temperature dependent and is described by an Arrhenius type equation [23].

Bastien and Gillespie attempted to extend the above model to a non-isothermal healing by dividing the process to small intervals of time at which isothermal fusion was considered at the average temperature interval t_i and t_{i+1}. The accumulative bond strength based on the reptation theory was the sum of isothermal bond strength within each interval.

$$D_h(t) = \frac{S}{S_\infty} = \sum_{i=0}^{\frac{t}{\Delta t}} \left[\frac{{t_{i+1}}^{\frac{1}{4}} - {t_i}^{\frac{1}{4}}}{{t_r}^{\frac{1}{4}}} \right] \tag{2.3.12}$$

Yang and Pitchumani doubted the above expression stating that the term in the bracket may be true only if the process was isothermal from time $t = 0$ to $t = i + 1$ for every interval i, at the average temperature T_i. Therefore the non-isothermal model above is not representative of the thermal history. They also noted that the reptation theory used in the development of the non-isothermal healing models [19] [24] [25] is not valid for large molecular weights of typical engineering thermoplastics. Hence, suggested replacing reptation time t_r with welding time t_w in equation 2.10 which would apply to either low or high molecular weights:

$$D_h = \frac{S}{S_\infty} = \left(\frac{t}{t_w}\right)^{\frac{1}{4}} \tag{2.3.13}$$

where the temperature dependent welding time for PEEK defined by Khan et al. [26] is as follows:

$$t_w(T) = 2 \times 10^{-5} e^{43000/RT} \tag{2.3.14}$$

whereas R is the universal gas constant.

2.3.3 Bonding

In thermoplastic processing, bonding is coupled to intimate contact and autohesion. Autohesion begins after initiation of intimate contact. Different bonding models are proposed in the literature depending on the process type [19] [21] [27] [28]. A model of bonding reported by Mantel and Springer [21] is as follows:

$$D_b = D_{ic} \cdot D_h \tag{2.3.15}$$

where the strength prediction is calculated by multiplying the degree of bonding by the ultimate strength which is assumed to be 89.16 MPa [29].

For processes such as resistance welding the degree of bonding is dominated by degree of intimate contact due to long processing time. However for the AFP or ATL process the polymer

temperature is raised to melting temperature before initiation of intimate contact. Therefore the welding time is shortened and can be of the same order of magnitude as the time to reach complete intimate contact and may not be neglected in equation (2.3.15) [16].

Stokes-Griffin and Compston later found that the bonding proceeds at temperatures below the melting and above glass transition temperature for CF/PEEK tape processed in ATL. They noted that the PEEK polymers are vastly amorphous during the consolidation due to the extreme cooling rates (plus 1000 ºC/s) and short processing time of ATL; given that the polymer is heated to above the melting temperature before initiation of intimate contact [30].

2.4 Crystallinity

Crystallinity can affect the mechanical properties of thermoplastic composites. A Higher degree of crystallinity enhances strength, and stiffness [31]. On the other hand lower degree of crystallinity increases impact resistance and fracture toughness [32] [33]. The degree of crystallinity depends on the thermal process history. Slow cooling rates result in higher degree of crystallinity and vice versa.

Hence the degree of crystallinity achieved through in-situ consolidation tape placement is limited due to extremely high cooling rates. Kumar et al. measured the degree of crystallinity of PEEK as well as spherulite growth rate for samples heated to a melt temperature of 380 ºC and 420 ºC, then cooled to the crystallization temperature of 300 ºC or 320 ºC at a rate of about 3 ºC/s [34]. At which point they measured the growth rate of spherulites. Their finding was that while the degree of crystallinity was not affected by the melt temperature, the size of crystals were larger for samples cooled from higher melt temperature. In other words, given a constant cooling rate, the spherulite size of the polymer is dependent on the peak processing temperature.

Sonmez and Hahn suggested the degree of crystallinity obtained for APC-2 is between 25% to 35% for in-situ consolidation process [35]. Similar levels of crystallinity are reported in other works suggesting that the degree of crystallinity of PEEK is not sensitive to cooling rates involved in the ATL/AFP process.

2.5 Void Dynamics

There are two types of voids inherent to the in-situ consolidation process: Intra-laminar, and inter-laminar. While intra-laminar void is set in during the tape impregnation phase, the inter-laminar void is mostly the result of the tape placement process.

The intra-laminar void is embedded in the tape. A micrograph of the incoming tape and the finished laminate revealed no change in the void fraction, shape, or size. Gruber et al. finding suggested that the ATP process is unable to reduce intra-laminar void content [22]. The result obtained here contradicts with earlier findings of Tierney and Gillespie on void dynamics of an HGT ATP process. They investigated intra-laminar void dynamics by employing microscopic and macroscopic models of void consolidation, and deconsolidation initially developed by Ranganathan et al. [36]; They cross-checked the models with experimental results and reported a good correlation between the models and the experimental data obtained from photomicrograph analysis. They found the dominant factor affecting the process is the deconsolidation of the void past the nip point. An expression for an instantaneous void fraction for the concentric void-resin shell can be derived from the governing equation for the microscopic void dynamics model as follows [37]:

$$4\mu\left(\frac{R^{*3}}{S^{*3}}-1\right)\frac{dR^*}{dt}+\left(P_g-P_fR^*\right)-\frac{2\sigma}{R_o}=0 \tag{2.5.1}$$

$$V_v=\frac{R^{*3}}{{S_o}^{*3}+R^{*3}-1} \tag{2.5.2}$$

whereas S is the outer radius of the surrounding resin sphere, R is the radius of the void sphere, P_g is the pressure inside the void, P_f is the pressure outside the void, σ is the surface tension between the air and the polymer melt, and μ is the resin viscosity. V_v is the instantaneous width-averaged void fraction, ${S_o}^*$and R^* are normalized by the initial void radius.

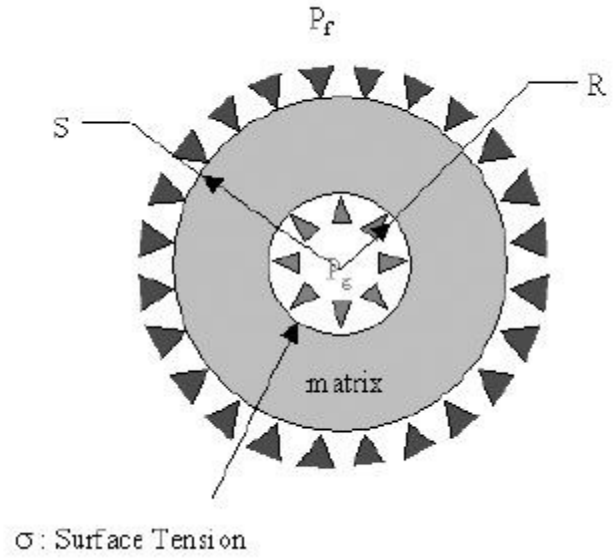

Figure 9: Concentric void-resin shell Model [37]

Deconsolidation occurs when the matrix temperature remains above T_g after the compaction pressure is released. To prevent void deconsolidation, it is suggested to anneal the surface [37] or cool the laminate below T_g before releasing the pressure [38].

The two studies show contradicting results. However, it is noted that the experiments are carried out using two fundamentally different end-effector designs. One with a double rigid roller [37] and the other using a compaction shoe [38] [39]. The double rigid roller may have facilitated the development of intimate contact as opposed to the compaction shoe. Also the result of both studies is analyzed using photomicrograph which may not be very accurate. 3D X-ray tomography is recently used to provide higher accuracy [40].

2.6 Experimental Investigation

The interest in the laser processing of thermoplastics initiated in the late 1990s. Biggs investigated thermoplastic welding of continuous CF/PEEK laminate using lasers in 1987. She observed significant matrix degradation without through melting of the lamina [41]. A year later Beyeler, Philips, and Güçeri used an 80 Watt CO_2 pulsed laser with a wavelength of 10.6 µm on a 6.35 mm (¼ inch) wide AC40-60 PPS carbon fiber prepreg tape to establish a process window for different materials [42]. A better mechanical bonding was obtained when least matrix

degradation occurred. They reported placement velocity and laser heat input to be the most important process parameters. Large inter-laminar voids were observed at higher placement rates. Beyeler et al. reported inconsistent results for the same set of processing parameters. They concluded that the process is highly sensitive to laser localized heating due to the small thermal inertia of the thin tape. They suggested decentralizing the heat input through pre-heating of the tape. Development of comprehensive modeling was also suggested for a more predictive approach to identify process window.

Agrawal attempted to validate the earlier heat transfer model suggested by Beyeler and Güçeri and finite element model by S.M. Grove later in 1992 [43]. He measured high cooling rate more than 1000˚C/s using thermocouples welded to the surface of the incoming tape. His result corresponded to short melt times of less than 0.1 second. He concluded to have longer melt times a delocalized radiative pre-heater, or a wider laser beam should be used. Having measured uneven temperature on the surface of the tape and the substrate Agarwal reported the uneven heating is due to the difference between roller and mandrel curvature and tape roughness. With roller usually having smaller curvature the feeding tape was heated to a higher temperature than the substrate.

Mazumdar and Hoa investigated process parameters using a 65 W CO_2 pulsed laser. They studied the effect of laser heat input, placement rate, and compaction force on the SBS of CF/PEEK tape. They used Taguchi approach to minimize the number of experiments. The L9 array was used for the three 3-level factor study. They found that after a certain threshold the compaction force has the least impact on the bond strength. Based on the ANOVA study they reported that the laser heat input to be the dominant factor, four times higher compared to the placement rate. However, the relation obtained here may be biased due to the wide laser power range and the process window defined for the effective consolidation.

Rosselli et al. found that the higher laser power results in better inter-laminar shear properties due to a higher degree of autohesion. They also reported that process is sensitive to transverse distance. “The transverse offsets consisted of aiming the beam from the original compaction point slightly towards the incoming tape (tape offset) or slightly towards the consolidated substrate (substrate offset).” Most reduction in inter-laminar strength was found

when the transverse offset was aimed toward the substrate than the tape given the angular offset of zero [44].

Grove presented an FEA thermal model of the process in which he determined lower laser incident angle will result in a more effective heating at the nip point. He identified that more direct incident will be achieved by lowering the laser incident from 15 to 10 degrees and that the intensity of irradiation would decrease on the substrate and increase on the tape. Grove also noted that the temperature falls rapidly near the nip point due to the shadowing effect of the roller [11]. He assumed a uniform heat source and a 2D anisotropic thermal model for the tape placement process.

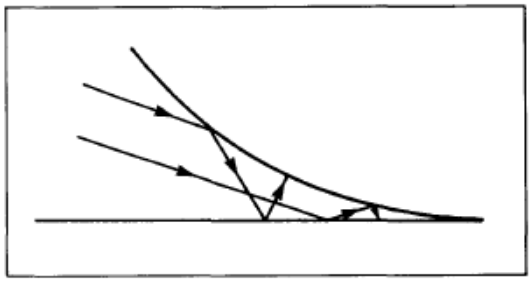

Figure 10: Reflection of incident laser beam of the tape surface and substrate [11]

New research interest was evolved in the laser-assisted processing field with the introduction of high power CW lasers, and advanced CFRTP tapes derived by increased demand in higher production rates. Nd-Yag and Diode lasers were already used extensively in material processing and welding applications. They offered a steady, and instantaneous heat input which was not attainable with the conventional CO_2 pulsed lasers. Also, the slow production rates reached using HGT setups did not meet production demand hence turning researcher's attention to alternative, more effective heat sources.

In 2013 Stokes-Griffin and Compston investigated the influence of consolidation force and laser power on bonding strength. Lap shear force was used to evaluate bonding strength. They monitored temperature and pressure history of the process. Given large conformable rollers, they only achieved a degree of intimate contact 0.39 or below. They suggested higher compaction force is required to attain increasedD_{ic}. They also observed better bonding at higher laser power and related it to enhanced degree of intimate achieved due to longer melt times [5]. In 2014 temperature history of the process was monitored using thermocouples embedded in the

laminates. The shadow region was identified and cooling rate was measured. The LATP processed parts were compared to those made in autoclave. Below optimum level crystallinity was reported due to incomplete through melting of the material, and fast cooling rates [45]. Comer et al. compared mechanical properties of laminates made using laser-assisted ATL and autoclave process. They reported higher inter-laminar toughness for the ATL samples. However, they reported higher ILSS, flexural strength, and flexural stiffness for autoclave samples. Their result yet confirms the higher void content of samples processed in ATL compared to the ones made in an autoclave. Stokes-Griffin and Compston later reached autoclave SBS levels for samples made using laser-assisted ATL process at placement rate of 100 mm/s. They reported optimum nip-point process temperature of about 550 to 600 ºC with no noticeable matrix degradation [46]. The processing temperature here is relevant to those suggested by Sonmez, and Hahn in which a maximum exposure time of 2 seconds is proposed for PEEK processed at 600 ºC. Higher processing temperatures without matrix degradation can be achieved at higher heating rates reported by Day et al. [47].

2.7 Mechanical Testing

Short beam shear (SBS) strength test is commonly used to measure the ILSS of multi layered flat or curved samples, such as rings, according to ASTM D2344. These tests are vastly used in the literature [16]. Width to thickness ratio of 2, Length to thickness ratio of 6, and span to thickness ratio of 4 is recommended for these samples.

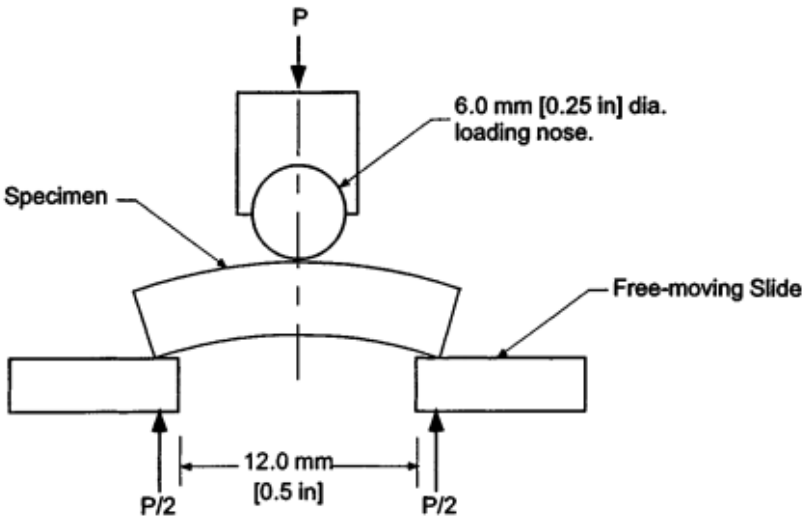

Figure 11: Horizontal Shear Load Diagram for Curved Beams – [ASTM D2344/D2344M - 00]

Rosselli and Santare compared SBS to an alternative method called Inter-laminar Shear Device (ISD) test which "involves shearing a specimen to failure along the direction of the fibers by applying compression loads to the end of the beam" [48]. They reported significantly different quantities of ILSS for the two methods but observed the same trend in the strength. They suggested ISD to provide a clear failure stress and more uniform shear stress distribution. However, SBS remains the standard method of ILSS evaluation for curved samples. The Double cantilever beam (DCB) is a similar test to SBS, carried out to evaluate bond strength according to ASTM D5528. Other tests such as lap shear test based on ASTM D5868 and wedge test based on ASTM D3762 are used as well to measure the ILSS for thinner laminates qualitatively.

Other mechanical tests reported in the literature include tension test, compression test, shear test, pendulum impact resistance test, three-point bending test, open-hole tension (OHT) and open-hole compression (OHC) test [16].

2.8 Laser-assisted End-Effector Design

The end-effector design of a laser-assisted AFP application is similar to that of HGT setup. The main difference, however, is the replacement of the gas torch with a laser beam processing module. Other modifications may be the use of air or water cooled conformable roller instead of a rigid metallic roller. Application of multiple roller and compaction shoe design is limited for laser-assisted end-effectors due to the localized heating of the beam, complexity, and cost. The laser-assisted setups are automated and are enclosed with safety barriers within a controlled nominal hazard zone (NHZ). Few commercial units are available in the market including Coriolis Laser Heating Device and Automated Dynamics Laser Heating System: *LIFT* Shown in Figure 12 [49].

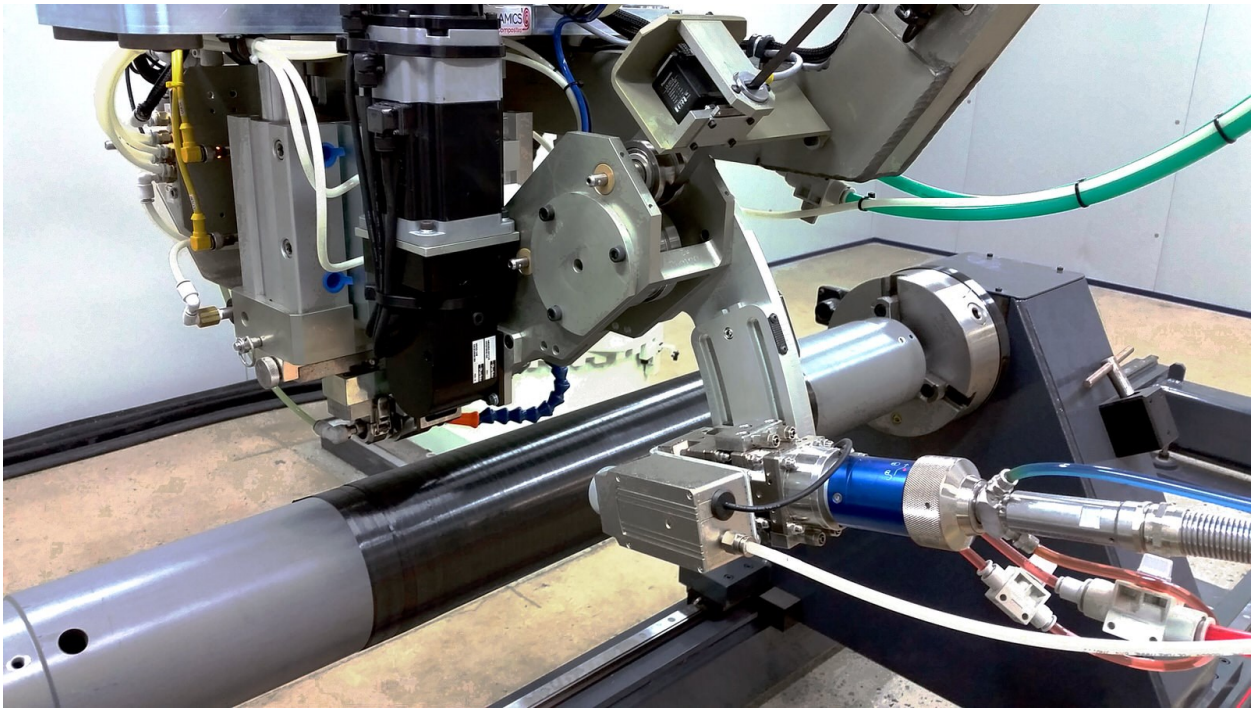

Figure 12: Automated Dynamics LIFT (Photo Courtesy from Automated Dynamics website) [49]

2.9 Research Objectives

The purpose of this work is to enhance the production rate of CFRTP PEEK unidirectional composite tape using a 2000 W continuous-wave Ytterbium fiber laser heating system compared to those processed with CONCOM HGT setup. Given similar processing parameters, higher processing temperatures at the increased heating rate are reachable with laser heating resulting in an enhanced degree of autohesion and bonding. Enhanced production rate without compromise in the mechanical properties of the final product is therefore anticipated.

To do so a laser-assisted system with collimator module is designed and built capable of producing process parameters similar to that of CONCOM HGT setup. The processing window is defined and optimized using the Taguchi approach. The bond strength is assessed by performing SBS test according to ASTM D 2344M standard. The effect of laser power, placement rate, compaction force, cooling rate and different tape system on ILSS is investigated.

CHAPTER 3: DESIGN OF THE RING MANUFACTURING APPARATUS

An apparatus capable of in-situ consolidating CFRTP unidirectional rings using a 2000W fiber laser is developed to carry out the experimental work presented in the proceeding chapters. The apparatus consists of a pneumatic powered end-effector, an electrically powered mandrel, and a laser processing module which are controlled remotely from a workstation outside of the nominal hazard zone (NHZ) using a set of relays and a microcontroller. The high power continuous-wave laser is delivered through fiber optic and coupled to a processing module. The processing module consists of a collimating, a focusing, and a shaping lens to output a uniform intensity beam. Any exposure to the laser light may cause serious or fatal injuries. The nominal hazard zone is therefore isolated from the operator zone by aluminum laser barriers, rated to withstand $3\ \mathrm{kW/cm^2}$ of irradiation. Moreover, the laser beam wavelength is outside the visible spectrum. The process is therefore monitored live using four infrared cameras which display the intense heat reflected off the roller and the tape as a visible violet light.

The main requirement of the laser-assisted setup is to manufacture six-inch diameter, quarter inch wide, and twenty-ply thick CFRTP rings safely and consistently. To conduct a valid comparison study, it must also replicate a similar setup used on the CONCOM HGT end-effector. Given the objectives of the apparatus, safety, simplicity, and robustness were the main pillars of the design work.

Aside from meeting functionality and safety requirements, both limited time and resources presented a substantial challenge, and risk to the completion of work which was managed through the implementation of concurrent engineering. Applying concurrent engineering techniques in the design and development process greatly reduced the time and cost of the project. Focusing on communication amongst involved parties from the beginning of the project allowed for identifying critical requirements, do proper planning and avoid surprises down the road. Design for assembly, design for manufacturing, safety, and accessibility considerations were simultaneously addressed through the use of accurate Computer-Aided Design (CAD) during the concept generation stage. The design and its requirements evolved and became clearer while creating multiple working concepts. Computer-Aided Modeling (CAM), Finite Element Analysis FEA, and testing of the subsystems too, eliminated the need for costly prototypes, guaranteed functionality and prevented unnecessary scrap and rework.

Detailed mechanical drawing of each component installed on the setup is provided in the Final Drawing Package booklet. About 30 or 10% of parts which are installed on the setup are custom made and machined either in-house or outsourced to other machine shops. It is therefore critical to keep an updated record of the latest design version of these parts. The rest of the parts are chosen from off the shelf to minimize cost and simplicity of the design. The final drawing package also contains information regarding pneumatic routings, electrical wiring, assembly drawings, bill of material (BOM), and other necessary information related to the setup. The purpose of the booklet is to enable the operator to repair, rebuild, or assemble the setup - if need be- from the ground-up.

3.1 Concept Generation

Brainstorming and clear identification of the requirement are the two central activities of this stage. The strategy is to be inclusive, innovative, and visionary when addressing the requirement in the design. The clearer the requirements, the simpler it will be to come up with a working solution for the problem. As mentioned above the requirements of the apparatus is identified by benchmarking available designs, and defining the scope of the work. A downward compaction force, a feeding mechanism, and a heating source are the main elements of the process. Other systems are built around these mechanisms.

Three successive working concepts were generated during this stage. Each concept is sketched upon brainstorming sessions. The creation of multiple distinctive concepts assisted in better identifying the sub-functional requirements. Based on the sketches, semi-detailed CAD models are created to demonstrate the interaction of sub-systems, and furthermore, pros, and cons of each working concept.

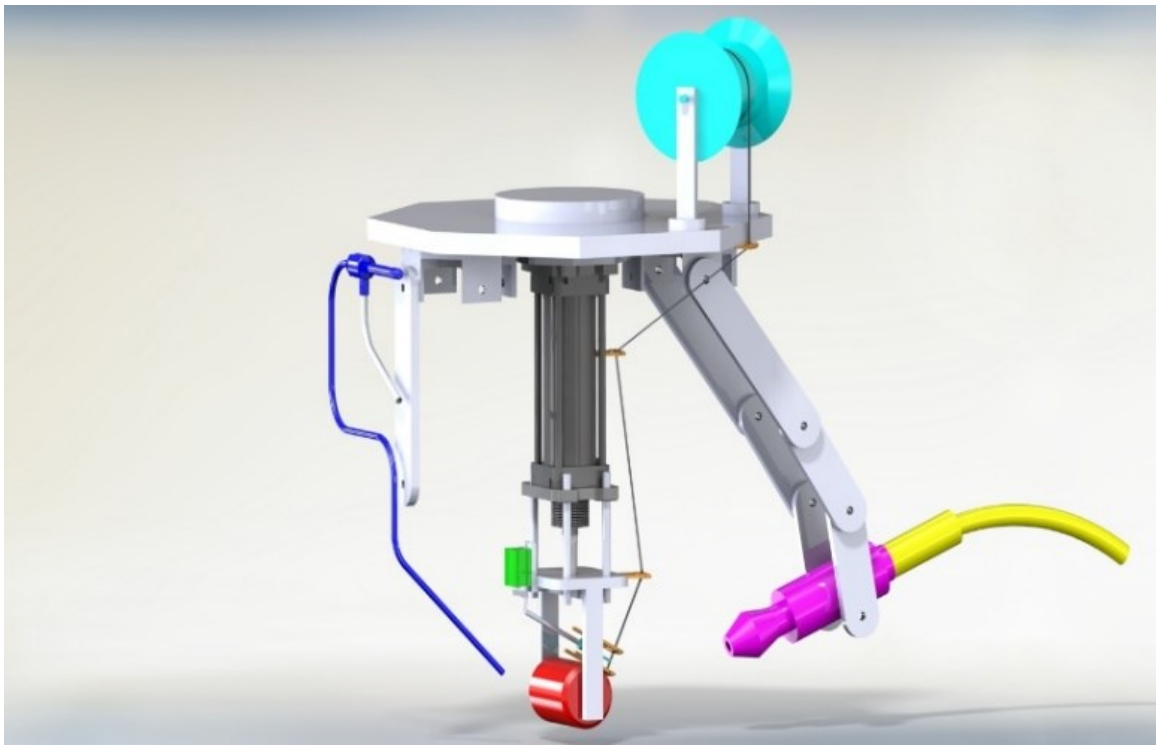

Figure 13: End-effector: Concept 1

The first concept demonstrated in Figure 1 has a frame which allows for the mounting of the apparatus on the CANCOM Kuka robotic arm. It employs a 25.4-mm (1.0-inch) aluminum base plate to hold the actuator and other components of the apparatus better demonstrated in the CAD model in Figure 13. The compaction force is applied through a double acting pneumatic actuator with a 152-mm (6-inch) long stroke. A conformable silicon roller transforms the load to the nip point. The laser processing module is attached to the metallic links for easy positional adjustment. The spool is mounted on the top of the plate while the tape is guided toward the nip point at a fixed incoming angle. An infrared sensor can be installed to detect slit in the tape. A smaller pneumatic actuator cuts the tape and is mounted on the roller base plate. A vortex chilling mechanism is also considered to cool the roller and the tape past the NIP point.

The second concept is shown below attempts to address the shortcoming of the laser positioning in the initial concept. The advantage of having the laser module and the roller mounted to the same assembly as the roller is to synchronize their movement. However doing so requires a much bulkier roller assembly set up to withstand the 4kg weight of the laser

processing module cantilevered at a rather long distance away from the nip point. It is also recognized that the actuator must be guided so to avoid the deviation from the vertical axis. A hollow 152-mm (6.0-inch) cylindrical steel pipe is used as the mandrel. The steel mandrel is to have less deflection under the working temperature compared to an aluminum mandrel.

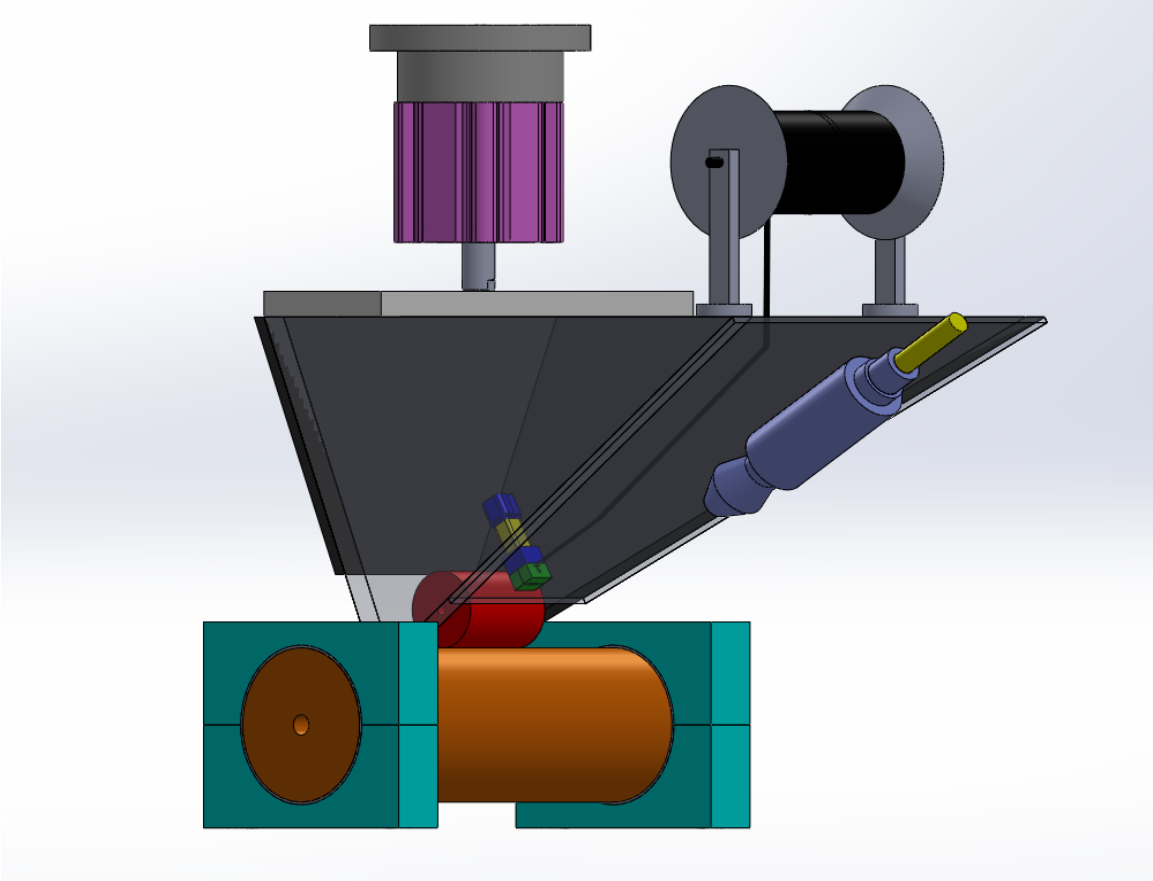

Figure 14: End-Effector Concept 2

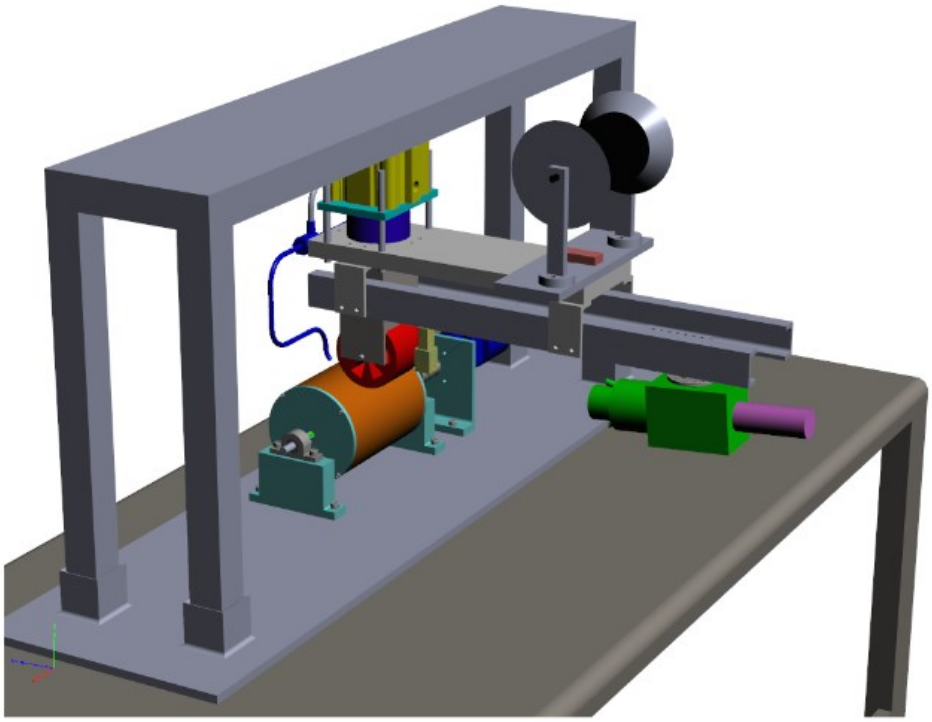

Figure 15: End-Effector Concept 3

For the third concept, the setup is mounted on top of a workbench using a welded, or preferably weld-free frame. The laser module is installed on two c-channels which are then connected to the roller assembly. The use of the c-channel assists in reducing deflection due to the cantilever weight of the laser module hung 12 inch away from the nip point. This assembly is thought to be much lighter than the one used in the second concept and allows for further positioning of the laser module away from the nip point. The double-acting pneumatic actuator has a larger bore diameter and a shorter stroke. A larger diameter bore pneumatic actuator is less responsive but can apply a more stable load. The shorter actuator stroke would allow for smaller overall setup size which would better suit the purpose. A load cell is also added to the actuator assembly to measure the applied magnitude and direction of the compaction force. The load cell is required for accurate measurement of the compaction force as there are losses associated with the pneumatic actuator, frame deflection, mandrel deflection and the direction of the applied force which may not be ideally vertical. The mandrel is rested on two pillow block bearings and

supported by a steel shaft instead of the two large bushings in the previous design. A reduction gearbox and a speed controlled brushless DC motor drive the mandrel at a high torque and low rpm range. The required torque of the motor shall be larger than the maximum desired torque of the air actuated slip clutch mounted on the spool shaft.

3.2 System Level Design

The functionality of sub-assemblies and their interaction with other components are defined at this stage. Decisions such as remote control and monitoring of the set-up led to the design of the sub-assemblies around the main components. Modular design is considered throughout the design. Modularity in design was an important consideration at such early stage of the development phase since the details of sub-systems were unknown. Modularity brought flexibility to the design which accommodated changes with the least impact on the overall system.

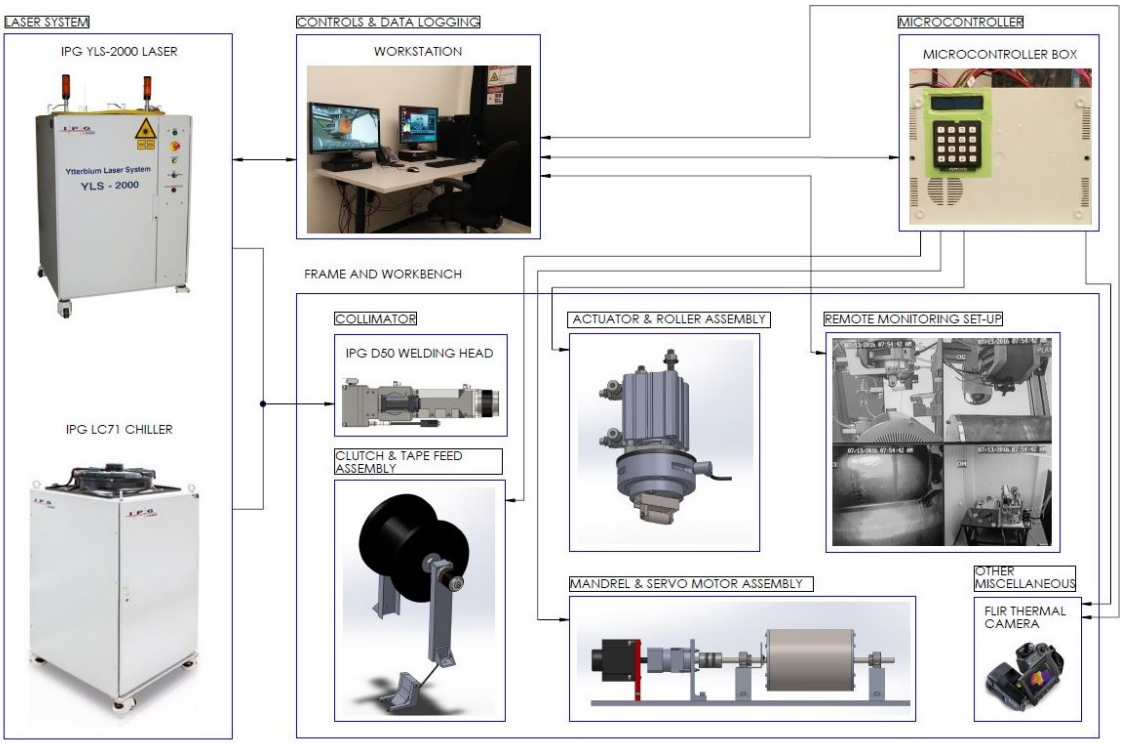

Figure 16: System Interaction Diagram

3.3 Sub-assembly Design

The overall setup is divided into 9 sub-assemblies. The design and function, and interaction of each sub-assembly is elaborated below. Detailed drawings of all components and assemblies are included in the *Final Drawing Package*, which is provided as an addendum to this report.

3.3.1 Mandrel Assembly

The mandrel is made of a 152-mm (6-inch) diameter, 6.3-mm (¼-inch) thick hollow steel cylinder. The advantage of the steel mandrel is its low coefficient of thermal expansion compared to that of Aluminum. Xie reported large dimensional deviation of the rings made at the NSERC AFP facility on the aluminum mandrel [6]. The coefficient of thermal expansion of Aluminum (23.7 ppm/°K) is almost two times compared to that of alloy steel 4130 (12.2 ppm/°K) at room temperature. The mandrel is estimated to reach up to 150 ºC during the manufacturing of the ring.

The other advantage of alloy steel is its high stiffness. Minimum deflection underline loading is desired for this application. The displacement and safety factor of the design is calculated through Solidworks Simulation FEA modeling. Due to the limitation of available cylinder wall thicknesses, minimum deflection is achieved through the design of two parameters: the support span, and the diameter of the shaft. The distance between the two support bearings is reduced from 415 mm to 315 mm. The shaft diameter is reduced from ¾ inch to ½ inch while remaining above the deflection limit of 0.1 mm, and safety factor of 4 for a local linear pressure of 40 MPa. Reducing the shaft size to ½ inch diameter permitted the use of a smaller coupler, bearings, and retaining rings which led to a considerable cost saving; a factor which had to be considered during the development of the setup.

A schematic of the mandrel assembly is shown below. The main components are labeled and are listed in Table 2 with their functionality and interaction within the assembly.

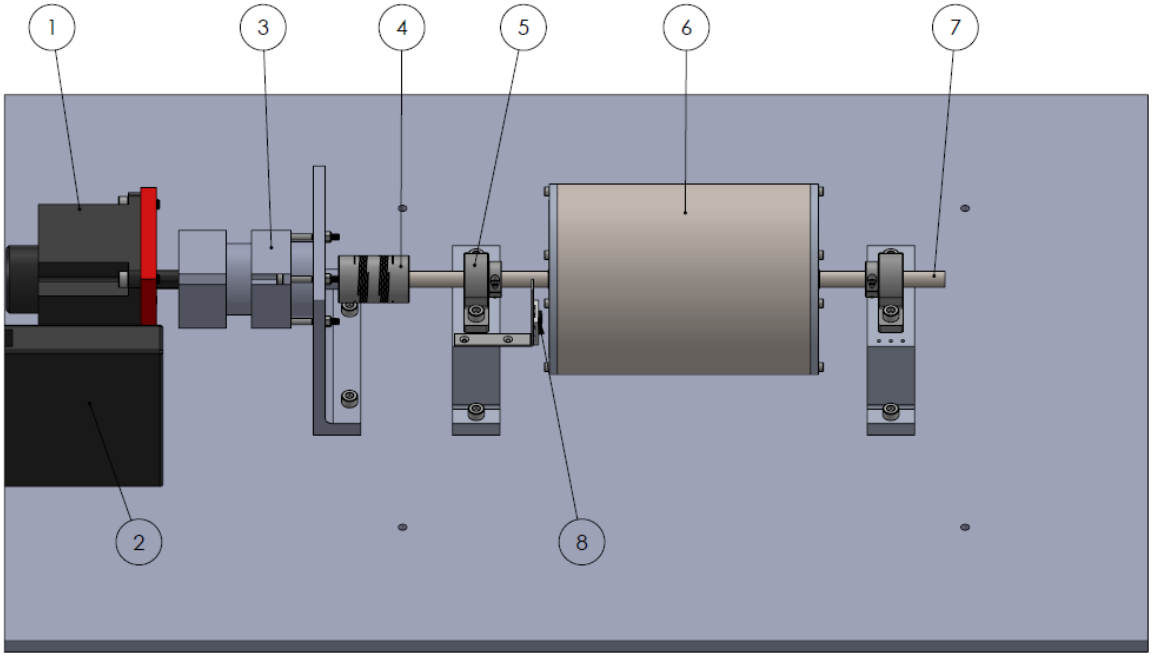

Figure 17: Mandrel Assembly

Table 2: Mandrel Assembly Main Components Description, Function, and Interaction

#	Part Description	Function	Interaction
1	½ hp stepper motor	drives mandrel	connected to motor driver
2	Driver motor	controls motor speed	connected to micro controller
3	8.2:1 Planetary reduction gearbox	reduces motor speed and increase torque	coupled to the motor and mandrel shaft
4	16mm to ½ inch flexible coupler	transmits torque from the gearbox to mandrel shaft	couples the gearbox and the mandrel shaft
5	½ inch Pillow housing bearing	supports radial loading	bolted to the pillow blocks
6	6D x 8L x ¼W inch alloy steel cylinder	layup tool	key mounted on the mandrel shaft
7	½ alloy steel shaft	mounts mandrel	coupled to the gearbox shaft
8	Infrared sensor	monitors mandrel speed	connected to the micro controller

Every ring is extracted or removed from the mandrel. The mandrel is therefore designed to be easily assembled and disassembled on the set-up as demonstrated in the animated image below. To extract the ring, the mandrel is clamped, and a shear force is applied to the side of the ring to slide it off of the tool surface.

However, the use of the available extractor machine for such a small size mandrel was not feasible. Hence manufactured rings are cut using a rotary tool with a diamond cutting blade at 5000 to 5500 rpm and then peeled off of the tool surface. The CFRTP pre-preg tape does not bond to the polished surface of the tool and application of a release agent is not necessary.

3.3.2 Actuator & Roller Assembly

A pneumatic guided actuator applies compaction force for the laser-assisted setup. A guided actuator is necessary to apply controlled vertical force. The double acting actuator can apply force in both directions and has a 63.5-mm (2.5-inch) long stroke. The meter-out flow control valves are used for smooth application and release of the compaction force. The rate of ascent and decent of the actuator can be tightly adjusted using the control valve knobs which regulate the passage of air in one direction. The flow control valves also prevent jerky movement of the actuator and the pressure loss due to the expansion of air inside the cylinder. The expansion of air occurs due to breakaway force being larger than the force required to keep the load moving. Once the breakaway force is reached, the air expands and pushes away the piston forward, faster than the incoming air. The result is a pressure drop inside the cylinder, and therefore stoppage of the piston. The process is repeated when sufficient pressure is built up inside the cylinder to overcome the breakaway force [50]. The two meter-out flow controls prevent the expansion of air inside the cylinder by regulating the exit flow.

A multi-axis transducer is mounted on the actuator to measure the magnitude and direction of the applied force. The transducer is connected to its controller box which measures the change in resistance of the strain gauges and converts the data to force and torque components. The converted data are then transferred to the computer using a serial port. The force and torque components are monitored and recorded on the serial channel using Putty, a freeware program. Before initiation of any measurement, all the force and torque components must be zeroed using SB command. A list of commands and a guideline on how to setup the

transducer are outlined in the user manual. Upon calibration of the load cell a scaler of 57.7 is used to convert the received data to the SI unit of force, N.

The design of the roller is similar to that of HGT AFP setup installed at CONCOM. For a valid comparison study, it was important that the laser-assisted setup resembles the same process parameters of the HGT AFP machine such as the roller size, roller material, tape incoming angle, etc. The roller is mounted on the roller adaptor. The configuration shown in Figure 18 is a 12.7-mm (½-inch) steel alloy roller used for 0-degree ply layup. The roller is supported by bearings and is mounted on a 1/8 inch diameter shaft. Retaining rings on opposite side of the bearings keep the shaft in place. The assembly is then bolted to an aluminum plate which is mounted on the frame. The description and specification of the main components are given in the table below.

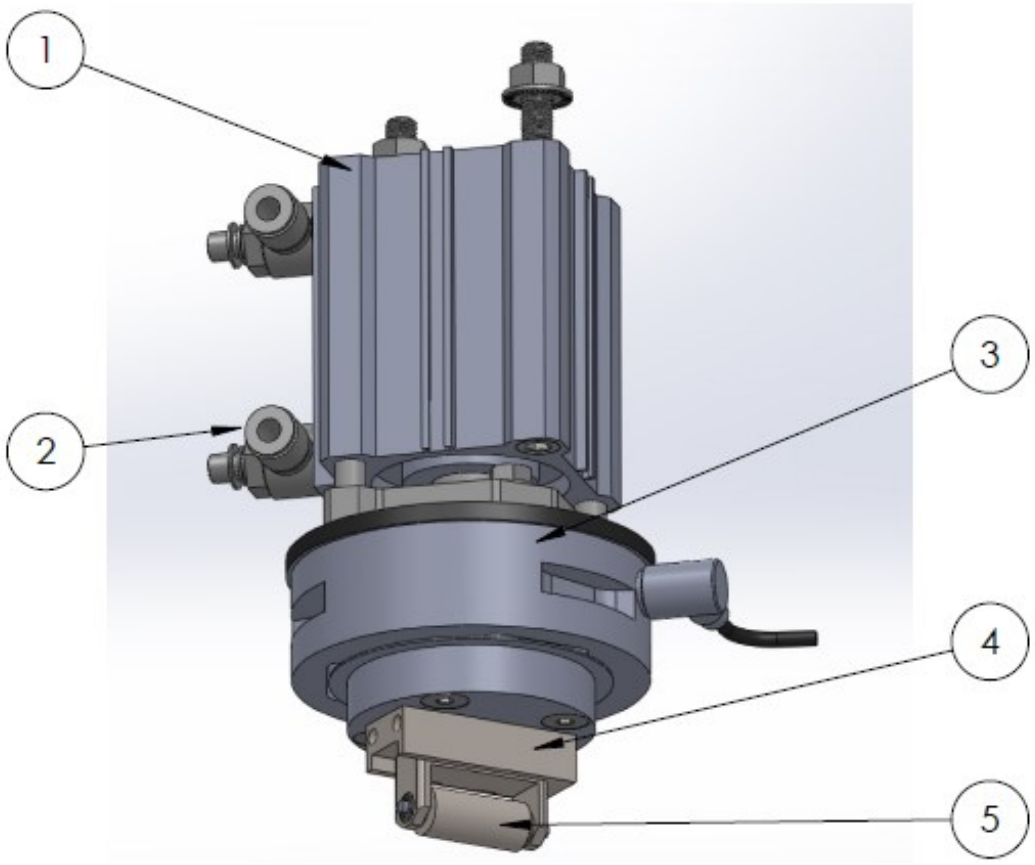

Figure 18: Actuator and Roller Assembly

Table 3: Actuator and Roller Assembly Main Components Description, Function, and Interaction

#	Part Description	Function	Interaction
1	Guided double acting pneumatic actuator	Applies vertical compaction force	bolted to the frame, connected to the pneumatic valves
2	Meter-out control valve	adjusts the stroke rate	installed on both actuator inlet
3	Load cell	measures compaction force	connected to the transmitter
4	Roller bracket	mounts the roller	installed on the loadcell
5	½ × ½ inch steel roller	applies compaction force	Air cooled; mounted on a 1/8 inch shaft

3.3.3 Clutch and Tape Guide System

A pneumatic clutch is installed on the spool shaft to keep the tape in tension. The thermoplastic tape is quite stiff. It does not require tension to retain stiffness at room temperature. However, upon heating the tape beyond its transition temperature Tg, the polymer softens and acts as a viscous fluid. If there is no force to keep the tape in tension, the fibers become wavy and miss-aligned. The waviness issue becomes more pronounced if preheating of the tape takes place further away from the nip point. Sufficient tension is then required to keep the fibers aligned before the tape is processed. Combination of tension and friction at the nip point aligns the fibers during the in-situ consolidation. The clutch shaft is supported by a ball bearing and inserted into the matching machined slot of the 22mm threaded rod. The clutch and bearing housing are bolted to the 0.32 mm (1/8 inch) thick c-channel.

A temporarily ABS 3D printed tape guide is used on the setup. The tape guide is preferably made of a metallic or ceramic material due to the abrasiveness of the CFRTP tape surface. The controlled and localized heating of the laser however, permits the use of the ABS part which is located as close as 2.5 cm (1 inch) away from the nip point.

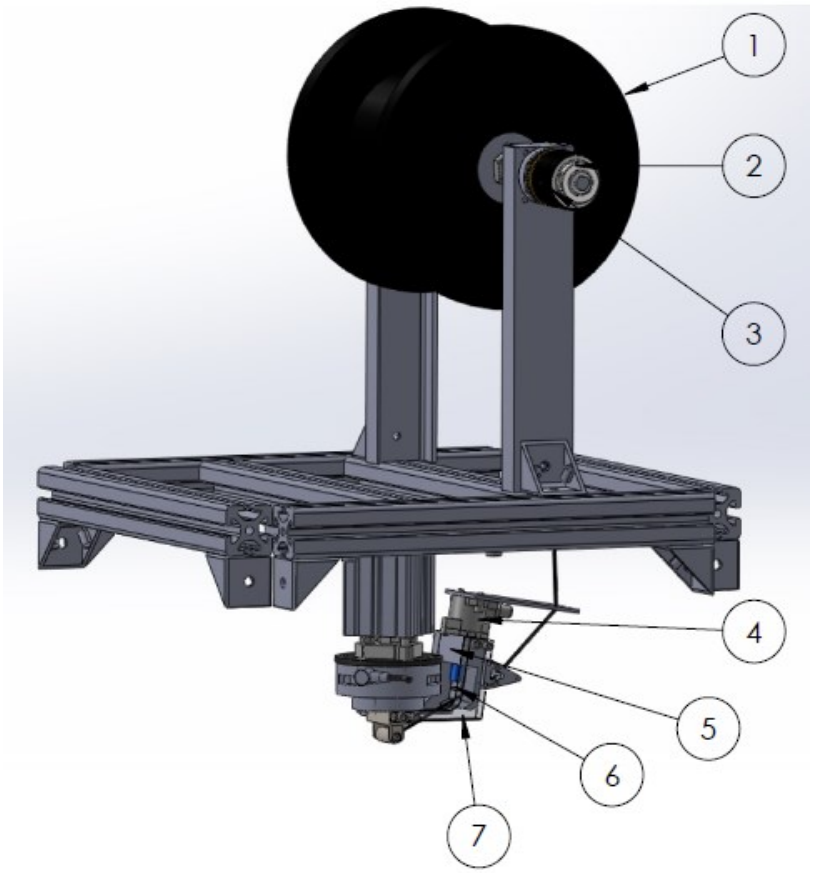

Figure 19: Clutch and Tape Guide Assembly

Table 4: Clutch and Tape Guide Assembly Description, Function, and Interaction

#	Part Description	Function	Interaction
1	Tape Spool	holds material	mounted on the spool rod
2	Pneumatic Clutch	provides tension to the tape	coupled to the spool shaft
3	Bearing housing	supports clutch shaft	Mounted on the c-channel
4	cutter actuator	cuts the tape	installed on the roller assembly
5	tape guide	directs the tape	bolted to the support brackets
6	Blade housing	holds the blade	mounted on the cutter actuator
7	Support bracket	mounts the assembly	bolted to the roller bracket

3.3.4 Pneumatic Valves and Regulators

The main actuator, the slip clutch, the cutter, and the air jet are controlled using solenoids and air regulators. The function of the solenoid valves are to allow the passage of the flow, while the regulators control the back pressure. The flow rate, which controls the speed of an actuator stroke, can also be adjusted using measure-out control valves. The diagram below shows the routing of the solenoids, regulators, and control valves used in the current set-up. During the manufacturing of the rings for the optimization study, an air compressor with a reservoir tank, regulator, and air filter was used as the main source. The volumetric flow rate of the source shall be greater than the sum of all individual routing to avoid pressure drop. The reservoir tank is therefore used to keep the source pressure higher than the maximum required pressure of any individual routing. The fittings of the pneumatic components are in imperial. Imperial hosing, tubing, and fittings are best suited for the pneumatic set-up.

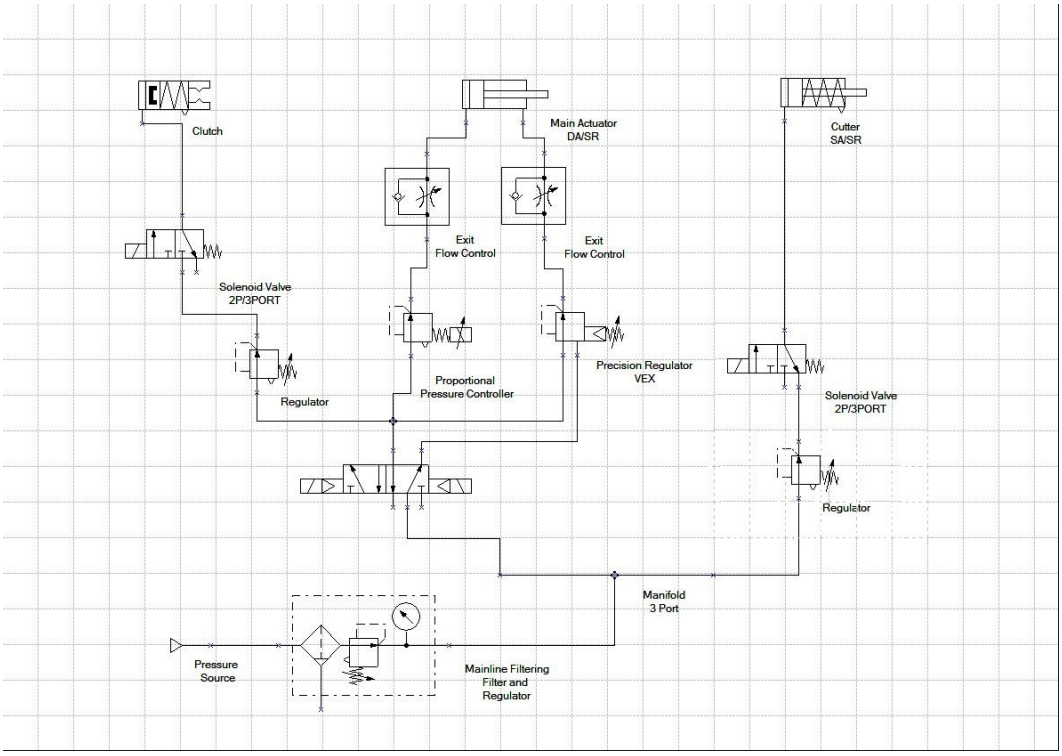

Figure 20: Pneumatic Routing, Valves, Actuators, and Regulators

3.3.5 Microcontroller

A microcontroller and a set of relays are used to remotely control the step motor and pneumatic powered components. The microcontroller can be controlled through the workstation computer or using the installed keypad on the control box shown in the figure below. Open source Arduino IDE is used to upload programs to the microcontroller. To simplify troubleshooting wires and relays are labeled inside the microcontroller box. For safety considerations, the operator shall not remain in the NHZ zone when the laser is in standby mode. As a result, the unit is connected to the computer with a 6m long USB cable, through the programming port, and is operated from the workstation outside the NHZ.

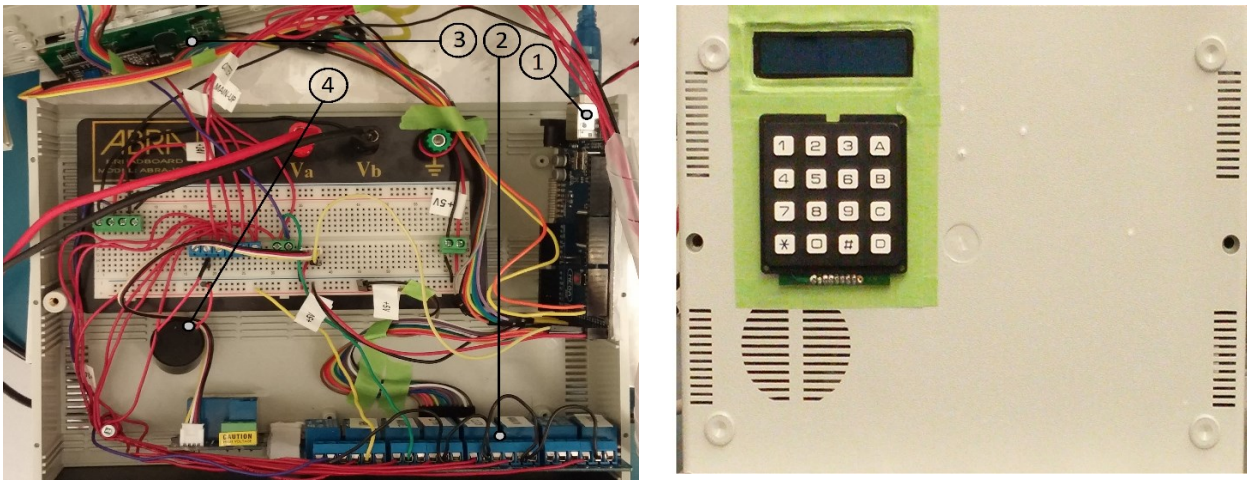

Figure 21: microcontroller box

Table 5: microcontroller box main components description, function, and interaction

#	Part Description	Function	Interaction
1	Microcontroller	automates setup control	connected to the computer
2	Relays	electrically operated switches	connected to MC digital I/O ports
3	Touch pad screen	displays input text	connected to MC digital I/O ports
4	Siren	beeps before the start and end of the operation	connected to MC digital I/O ports

Figure 22 shows the work-flow diagram of the microcontroller for a complete ring manufacturing cycle. The program is written to loop between the end and the start of the process. The operation initiates after the number of layers is inputted. At the end of each run, the main

actuator retracts to release the pressure on the tape, and the program asks for the user input again. The main code consists of the run function which carries out the procedure shown below. Several different functions are written to test individual components for troubleshooting and calibration purposes. The programs can be located in appendix A.

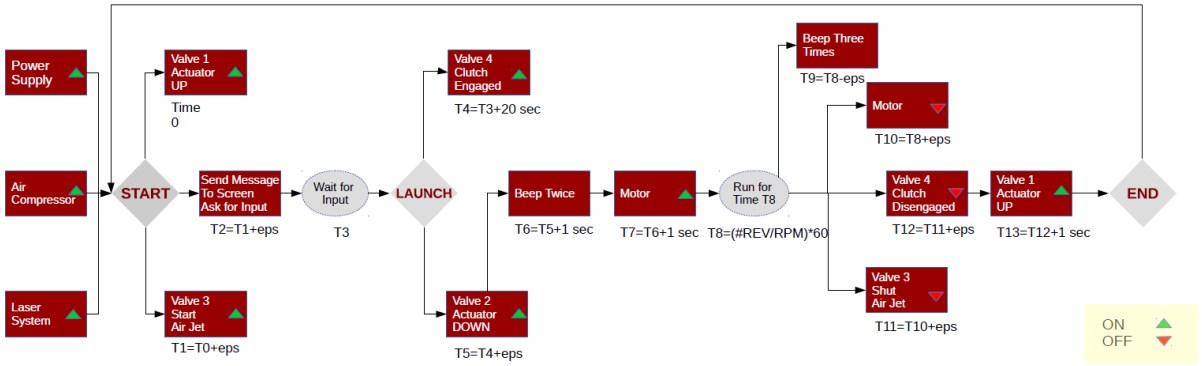

Figure 22: Microcontroller Diagram

3.3.6 Thermal Camera

A thermal imaging camera, FLIR T540, is used to record the hot spot at the nip point and off the ceramic conversion screen for subsequent beam calibration experiment. The thermal camera does not provide accurate measurement of the nip point as it cannot detect direct reflection near the nip point of the substrate or the incoming tape. However, it is used as a qualitative measure of beam profile shape and intensity. The analysis of the thermal images is done through *FLIR Tools* software. Average temperature, maximum, minimum, and room temperature are measured and reported for a local hot spot zone defined by the user.

3.3.7 Infrared Cameras

Four cameras are installed to remotely live monitor the process from the workstation. The cameras detect heat reflected off the nip point and display it as a violet light on the screen. Each camera is critical for monitoring the process. They are positioned to view the tape lay-up, nip point, roller assembly, and the overall set-up. The operator observes all four channels during the process for any potential issue. In case of an issue, the laser emission and standby mode is switched off. The laser power is set to zero, and the microcontroller is restarted from the computer by uploading the basic code. At this point, it is safe to enter NHZ with proper safety

equipment and begin troubleshooting of the system. The eight-channel camera receiver records and stores videos up to 200 GB.

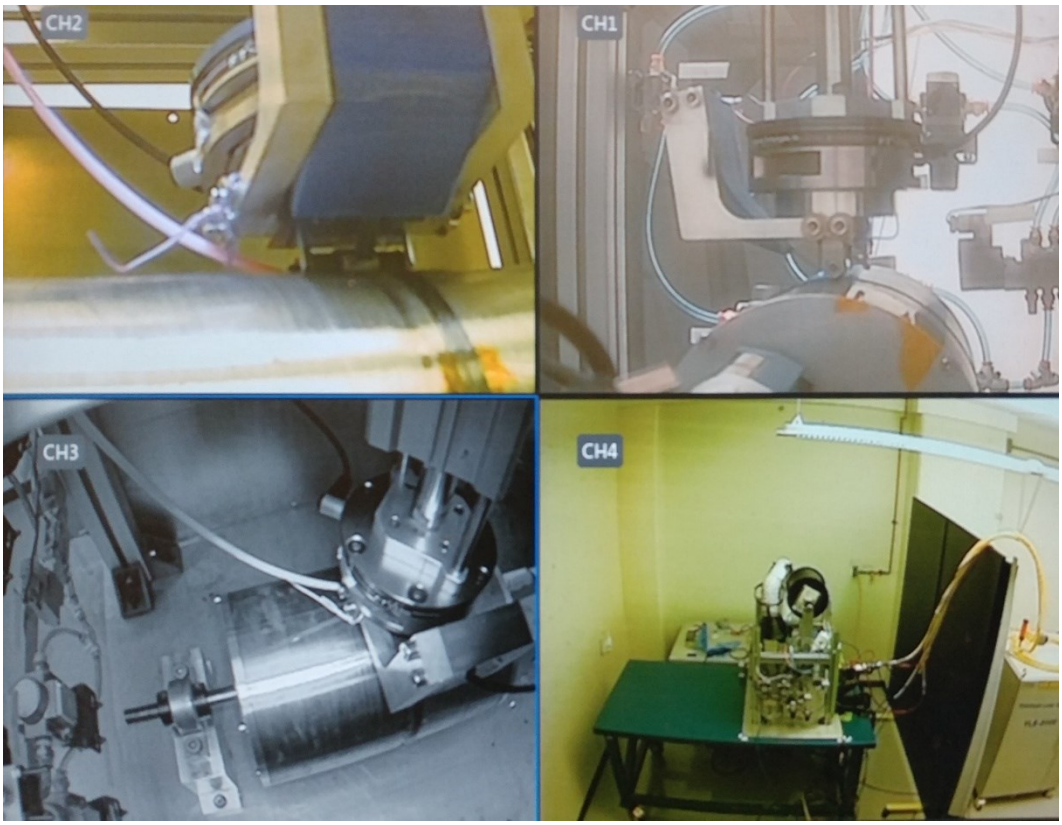

Figure 23: Monitoring the process using four infrared cameras

3.3.8 Laser System and Chiller

The laser system is a diode-pumped continuous wave Ytterbium fiber laser with a nominal output of 2000W. The Ytterbium laser emits a near-infrared light of 1064 nm wavelength. The laser is water cooled using water to air chilling unit. The supplied chilled de-ionized (DI) water cools down the laser modules, power supply, and the accessories such as the collimator unit. The laser operates at 480 volts and a minimum threshold of 10% of its nominal output power (200W). The diameter of the beam inside the 5 m long feeing fiber is 50 µm. It is outputted using an HLC-8 connector.

The emitted NIR light is invisible to human eye. Screen conversion plates can be used for alignment of the beam. The laser is also equipped with a 40 µW power laser guide beam for on-spot alignment.

The laser is classified as a high power class IV instrument under 21 CFR 1040.10. The total light energy radiated from the optical output is greater than the nominal output power of the device per optical port according to the IPG laser User Guide. Severe damage to the eye or skin may be caused at this at this emission level. For safety reasons, the unit operates with multiple interlocks in place. Refer to customer interfacing connections in the user manual for a list of interlock interfaces and required connections to operate the laser.

The laser unit is connected to the workstation computer through Ethernet interface and is controlled using laser net software. The laser power is manually adjusted through control tab. It can also be analog controlled, externally controlled using a microcontroller or programmed for automatic operation. Both the laser and the chiller shall be properly maintained as laid out in the user guide to prevent any damages to the units or deterioration in their performance.

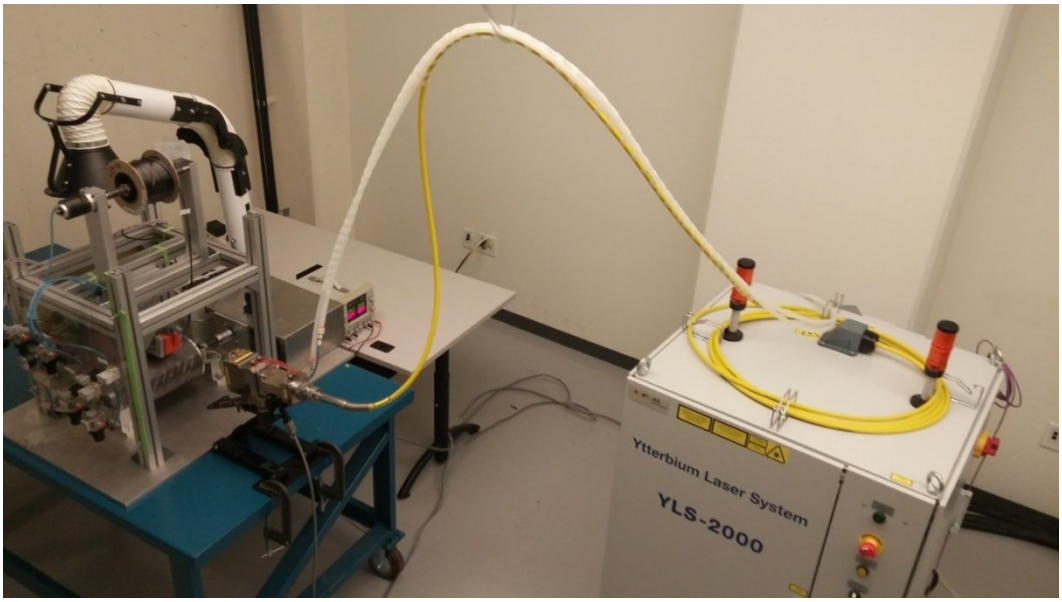

Figure 24: YLS2000 Laser System Plugged to D50 Welding Head

3.3.9 Collimator Module

The collimator module is a standalone configuration, model D50, laser welding head purchased from IPG Photonics. The main components of the D50 welding head are labeled in Figure 25 are as follows:

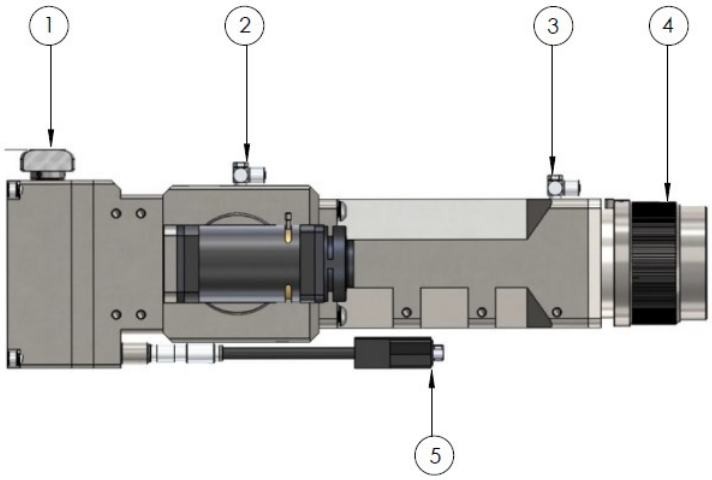

Figure 25: IPG Standalone D50 Laser Welding Head

The laser light travels through a fiber cable with a Bayonet (quick connect head) at one end. The Bayonet is plugged into FCH-8 fiber receiver and is locked into place. The modules of the collimator are water-cooled. The LC71 chiller cools both laser and collimator module. A removable cover slide assembly houses a protective lens. The lens prevents contamination and damage to the focusing, shaping, and collimating lens and shall be cleaned and maintained with the IPG supplied cleaning products. Finally, the 9-Pin D-sub Connector can be either connected to an IPG Welding Window Sense Board or a microcontroller to monitor the temperature of the lenses and warrant if the cover glass is present. This feature has not been configured for the current set-up.

Table 6: IPG Welding Head Main Components: Part Description, Function, and Interaction

#	Part Description	Function	Interaction
1	Removable cover lens	protects collimator lens	installed in slider cover assembly
2	Focusing lens	focuses the beam	water cooled
3	Collimator lens	collimates the beam	water cooled
4	Double lock FCH-8	outputs fiber laser	connected to the collimator
5	9 Pin D-sub Connector	sensor interface	not connected

3.4 Overall Assembly

Figure below demonstrates the overall assembly of the ring manufacturing set-up. To further simplify the design, the collimator is mounted independent of the roller assembly. The independent mount design results in slight variation of the beam position bias as the plies are built-up. This compromise is signified for thicker parts. The cooling mechanism in the below set-up is through compressed air. While the current set-up provides sufficent cooling for the steel roller, additional cooling is deemed necessary for the conformable roller. The use of a vortex tube to supply additional cooling is therefore recommended.

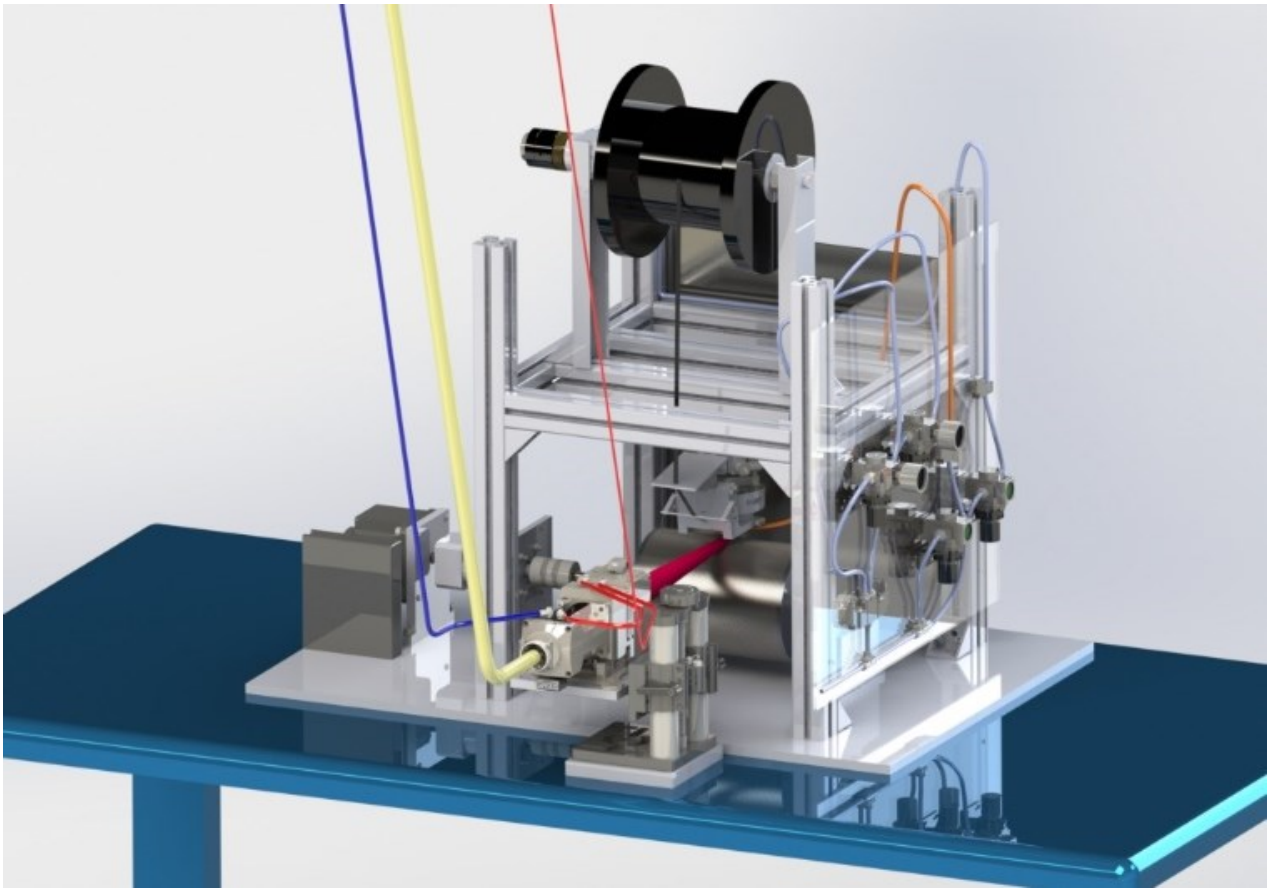

Figure 26: Final CAD model of the ring manufacturing set-up

CHAPTER 4: EXPERIMENTAL INVESTIGATION

Several studies are carried out to investigate the effect of main process parameters and different heating systems on the inter-laminar bond strength of carbon fiber reinforced thermoplastic (CFRTP) composite rings.

First, a DOE optimization using Taguchi method with three four-level factors is designed to study the effects of placement rate, laser power and compaction force on the inter-laminar shear strength of 20-ply rings made of TenCate Cetex® TC1200 AS4/PEEK unidirectional tape.

Second, the optimum processing window identified to form the DOE study is used to compare the bond strength of rings made using laser heating and hot gas torch heating placement. Two different material systems namely: CYTEC AS4/APC-2 and TenCate Cetex® TC1200 AS4/PEEK tapes are the subjects of the comparison study here.

Third, the placement rate and its effect on the bond strength for a wide range of processing temperatures is investigated using CYTEC AS4/APC-2 tape. The adoption of an expanded laser spot size and the use of a conformable roller is considered to reach a better degree of bonding at higher placement rates. Hence the effectiveness and intensity of the laser beam away from the working distance is characterized. A silicone conformable roller is also designed and fabricated to study the feasibility of its implication.

Finally, the thermal history of the laser heating process is measured. Short beam shear test is used throughout the studies to provide a measure of bonding in terms of inter-laminar shear strength. The force vs. displacement for every coupon is recorded. The coefficient of variation and the standard deviation for each batch is reported. The failure mode is analyzed using micrograph images. The compaction force, the laser power, and the placement rate are measured a 6-axis ATI transducer, the laser-net software, and the mandrel motor driver respectively.

The context of section 4.1 is published in proceedings 3rd International Symposium on Automated Composites Manufacturing, Montreal, Canada 2017 April 20 [51]. As well as the context of sections 4.2, 4.3, 4.4 which are presented at CANCOM 2017 – Canadian International Conference on Composite Materials. Ottawa, Canada 2017 July 17-20 [52].

4.1 DOE Parameter Optimization

A Design of Experiment (DOE) using Taguchi method is carried out to find near-optimum condition within the processing window. Mechanical properties of rings made of 6.35 mm (¼ inch) wide TenCate Cetex® TC1200 AS4/PEEK thermoplastic tape are investigated by examining three factors: laser power, feed rate, and compaction pressure. Four levels are selected for each factor to provide the most information on the non-linear behavior of factors. To assure the repeatability of the process three samples of each ring are made at different times. Short beam shear test is performed to measure the bond strength in terms of ILSS.

4.1.1 Optimization Using the Taguchi Approach

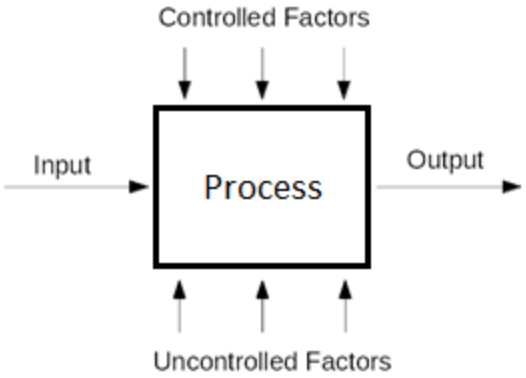

Figure 27: Definition of Taguchi Process

A statistical optimization method, the Taguchi approach is employed to investigate the effect of influential process parameters on bond strength; as well as identifying the optimum processing conditions based on the SBS test results. Taguchi is a standardized fractional factorial method using a special set of orthogonal arrays to minimize the required number of experiments. Improved reproducibility of results is also expected with using orthogonal arrays because the

influence of all present factors is accounted for when analyzing the main effect of factors [53] [54].

Once the methodology is determined, the experimental planning is carried out according to recommended steps in ref [53]. The laser-assisted placement process can be defined as a system shown in Figure 27 in which a unidirectional carbon fiber thermoplastic tape is the input. The laser-assisted placement process can be defined as a system shown in Figure 27 in which a unidirectional carbon fiber thermoplastic tape is the input. Bond quality measured by short beam shear SBS test is the response of the system here. Multiple controlled factors are identified; namely laser power, placement rate, compaction force, tape tension, roller geometry, laser beam size, beam position, and angle of the incoming tape. Finally, roller temperature, substrate temperature, and room temperature are identified as uncontrollable factors.

4.1.2 Identification of the Process Window

To specify the levels for each factor the Taguchi, it is necessary to identify a process window where an effective bonding would take place. The effective bonding degree is assessed qualitatively here by peeling away the outer ply at 90 degrees. If the ply is peeled away easily, then the inter-laminar bonding is deemed weak, and not to be effective; whereas for an effective bonding the outer ply demonstrates good resistance to the peeling force resulting in the unprocessed tape to break.

Consequently, the boundaries of the process window are identified. For example, very low bonding takes place at a placement rate of 168-mm/s (6.6-in/s) and 235-W, hence 240-W defines the lower boundary of the laser power. On the other hand at 114-mm/s (4.5-in/s) and 260-W week bonding results due to substantial degradation. Therefore 117-m/s is selected as the lower boundary of the placement rate. Also, a 135-N force is determined to be the minimum compaction force to have a good bonding. Any compaction force beyond 535-N (120-lbs) results in substantial deflection of the mandrel and is, therefore, the limit here.

4.1.3 Experimental Procedure

6.35-mm (¼-inch) wide TenCate Cetex® TC1200 AS4/PEEK tape is used to make 20-ply 152-mm (6.0-inch) diameter rings using a 12.7-mm (½-inch) diameter steel roller. A modified Taguchi L16 orthogonal array is used to study the effect of three, four-level factors, tabulated in

Table 7. Four level design is used here to gather more information on non-linear effects of factors. Studying more factors could have been beneficial but would have increased the complexity of the experiments. However other controllable factors could be the subject of future studies as they may have a significant influence on the process outcome.

Table 7: List of Factor and Their Corresponding Levels as Input of L16 Orthogonal Array

Level	A Placement-rate mm/s (in/s)	B Laser Power W	C Compaction Force N (lbs)
1	117 (4.6)	240	135 (30)
2	132 (5.2)	245	270 (60)
3	145 (5.9)	250	400 (90)
4	168 (6.6)	255	535 (120)

Since lack of reproducibility voids the experiment, three rings of each combination are made at different times to assure the ring manufacturing apparatus is capable of experimenting. Therefore forty-eight rings with sixteen different combinations are made. At least three samples from each ring are cut and tested for SBS according to ASTM-D2344M standard. The force versus displacement data is recorded and plotted by Hoskin Scientific Apparatus. The first maximum load is recorded, and the ILSS is calculated as follows:

$$F^{SBS} = 0.75 \times \frac{P_m}{b \times t} \tag{4.1.1}$$

whereas P_m is the maximum load, b is the specimen width, and t is the specimen thickness.

To prepare the samples, the sides of the ring are first sanded to attain parallel edges. A diamond blade and a jig are then used to cut few coupons from random locations around the ring. The coupons are loaded as shown in Figure 28. Two flat blocks, placed equidistance with respect to the center of the loading nose, support the curved coupon with a span of 12 mm. The loading

nose, 6mm in diameter, is dropped at a constant rate of 1mm/min. A 5 kN load cell measures the applied force without any noticeable noise.

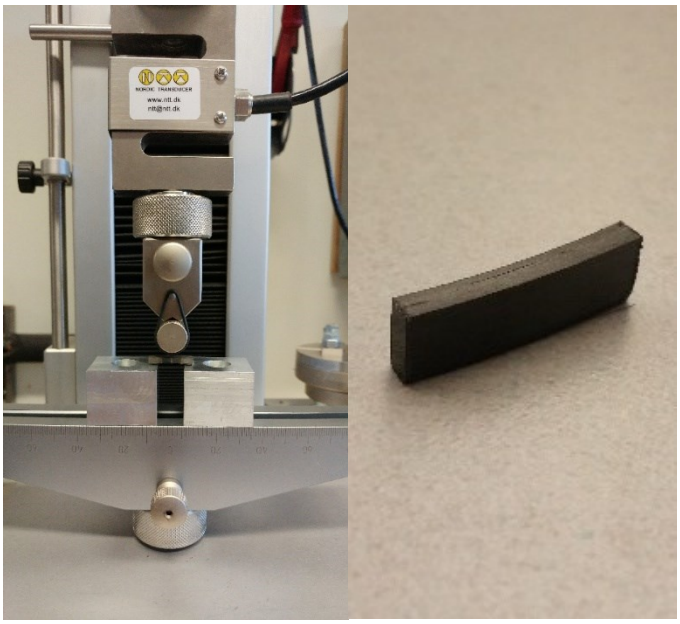

Figure 28: Short Beam Shear Test Coupon and Setup

Table 8: Result of SBS Test, Standard Deviation, and Coefficient of Variation for All Conditions

Trial	Factor A	Factor B	Factor C	Ring 1	Ring 2	Ring 3	SD	% CV
#	**Placement-rate mm/s (in/s)**	**Laser Power W**	**Compaction Force N (lbf)**	**Ave SBS MPa**	**Ave SBS MPa**	**Ave SBS MPa**	**All**	**All**
1	117 (4.6)	240	135 (30)	32.0	37.7	31.5	3.4	10.2
2	117 (4.6)	245	270 (60)	33.3	37.0	33.6	2.1	5.9
3	117 (4.6)	250	400 (90)	32.1	38.4	37.4	3.4	9.4
4	117 (4.6)	255	535 (120)	40.3	43.0	43.2	1.6	3.8
5	132 (5.2)	240	270 (60)	27.9	26.1	32.1	3.1	10.7
6	132 (5.2)	245	135 (30)	29.3	27.9	30.8	1.5	4.9
7	132 (5.2)	250	535 (120)	28.7	30.4	32.5	1.9	6.3
8	132 (5.2)	255	400 (90)	31.6	26.4	28.0	2.7	9.3
9	145 (5.9)	240	400 (90)	22.7	27.6	27.9	2.9	11.1
10	145 (5.9)	245	535 (120)	30.9	27.0	24.1	3.4	12.5
11	145 (5.9)	250	135 (30)	27.7	27.5	28.0	0.3	0.9

12	145 (5.9)	255	270 (60)	27.3	30.2	27.4	1.6	5.8
13	168 (6.6)	240	535 (120)	16.9	21.4	18.8	2.3	11.9
14	168 (6.6)	245	400 (90)	24.4	23.0	25.6	1.3	5.5
15	168 (6.6)	250	270 (60)	20.9	21.7	27.2	3.4	14.7
16	168 (6.6)	255	135 (30)	22.1	23.2	25.2	1.6	6.8

4.1.4 Reproducibility of Data

The result of SBS test for the 16 combinations is tabulated above. Three rings with three samples from each ring are tested for every condition. The coefficient of variation CV for the majority of the population is below10%, and thus the experiment is capable of reproducing data.

4.1.5 Studying the Factor Effects

The effect of parameters is studied with two different methods. The first is by calculating the average of effects based on the population mean. The other is to evaluate the signal to noise S/N ratio of parameter effects and thus calculating the average of effects based on S/N ratio. The S/N ratio is a logarithmic transformation of mean squared deviation MSD which measures the variation of a population from the target. Therefore S/N ratio compares both location and variation of two or more population [54]. For this study, the target is to maximize the response. Therefore MSD is calculated for a target response of infinity as follows:

$$MSD = (\frac{1}{n})(\frac{1}{Y_1^2} + \frac{1}{Y_2^2} + \cdots + \frac{1}{Y_n^2}) \tag{4.1.2}$$

$$S/N = -10\, log_{10}(MSD) \tag{4.1.3}$$

whereas $\bar{Y}$ is the mean of response and n is 16, the number of conditions. For comparison purposes, it is always desired to maximize S/N ratio regardless of target characteristic. Depending on the method used, the average effect of a factor thus is the average of population means or S/N ratios corresponding to that factor.

Table 9: Average Effects of Factors

Level	Means of Means [Mpa]			Means of S/N Ratio [Mpa]		
	A	B	C	A	B	C
1	36.6	26.9	28.6	31.2	28.3	29.0
2	29.3	28.9	28.7	29.3	29.5	29.0
3	27.4	29.4	28.8	29.1	29.2	29.0
4	22.5	30.7	29.8	26.9	29.5	29.5

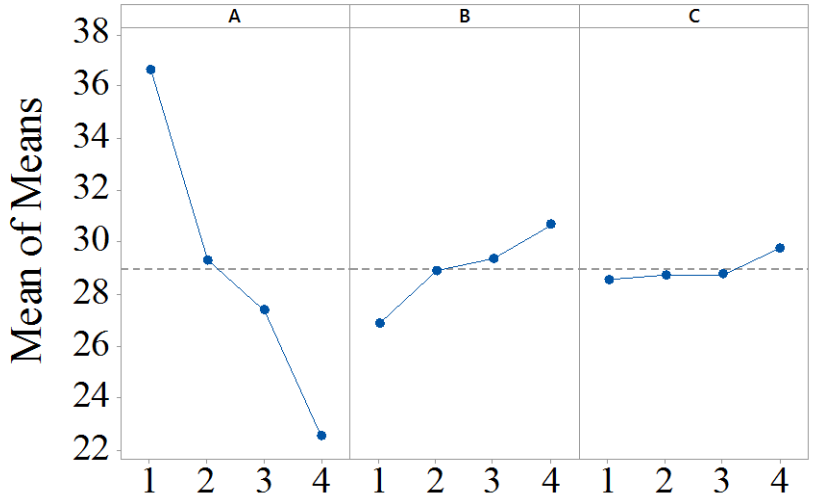

Figure 29: Main Effect Plots: Means of Means

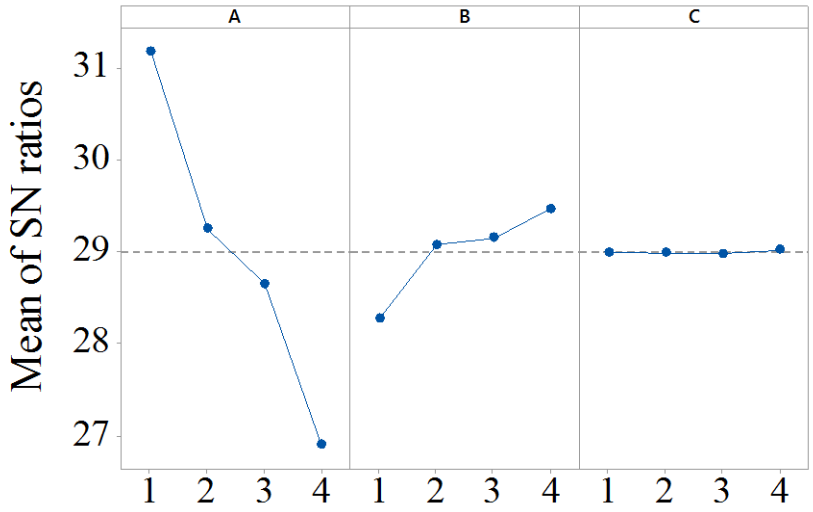

Figure 30: Main Effect Plot: Means of Signal to Noise Ratio

The result is shown in Figure 29, and Figure 30. Either method suggests a similar behavior of factors except for compaction force. Main effects plot based on average performance indicates better bonding is achieved at compaction force of 400-N (90-lbs) or more. However, this is not the case as variation about the target is not taken into account by the first method. There is no contribution made by higher pressure as can be seen from S/N ratio plot. It can, therefore, be noted that the S/N ratio is a more appropriate term to compare two populations. Meanwhile, the bond quality is highly influenced by a change in placement rate. An increase in placement rate significantly diminishes the bond strength while an increase in laser power improves it; indicating an indirect interaction between the two parameters and that inadequate laser power inhibits proper bonding.

4.1.6 Relative Influence of Parameters

Relative influence of parameters is obtained through the analysis of variance ANOVA according to Roy [53]. A general linear model is fitted for the ANOVA.

The relative influence for a 95% confidence level CL is calculated as follows:

A = 86.3% B = 6.2% C = 0.7% Error = 6.8%

whereas the error term represents experimental error, noise factor, and controllable factors which are not considered in the experiment.

Relative influence can be interpreted as a quantitative measure of parameter effect. It is the measure of individual parameter influence on total variation. A parameter which has a high relative influence is deemed significant. Therefore placement rate (A) is a significant factor influencing variation. Contrarily compaction force (C) can be neglected due to its low relative influence. The analysis is then reevaluated with factor C being omitted. Consequently, the results are as follows:

A = 86.3% B = 6.2% Error = 7.5%

It is important to interpret the relative influence with care as the population variation depends largely on the process window. A finer range of placement rate would have decreased its influence on variation. Therefore the relative influences are valid for the process window defined in this experiment. Hence better understanding of the interaction amongst factors is required to enhance robustness.

4.1.7 Expected Response at Optimum Condition

To estimate the optimum condition, the contribution of all factors are simply added to the grand average of performance, denoted by $\overline{T}$. Thus the response at optimum condition based on average performance is as follows.

$$Y_{OPT} = \bar{T} + (\bar{A}_1 - \bar{T}) + (\bar{B}_4 - \bar{T}) + (\bar{C}_4 - \bar{T}) = 39.2\ MPa \tag{4.1.4}$$

The estimated optimum condition for the linear model is 39.2-MPa with 95% confidence interval CI of 34.7 to 43.7-MPa. The actual optimum SBS of 42.1-MPa obtained at condition four falls within the 95% CI.

4.2 Laser-Assisted vs. Hot Gas Torch Heating

Upon identifying the laser-heating process window, it is of particular interest to gauge the optimum bonding quality of the laser heating placement against the hot gas torch placement setup. A valid comparison study is plausible as the two setups can produce identical processing conditions.

Based on the previous optimization work performed on the HGT placement setup at CONCOM it is known that any two material systems do not exhibit the same performance under similar process conditions [6]. Therefore both available tape systems namely: A) TenCate Cetex® TC1200 AS4/PEEK, and B) CYTEC AS4/APC-2 are the subject of the study here.

4.2.1 Experimental Procedure

20-ply, 152-mm (6.0-inch) in diameter, 6.35-mm (¼-inch) wide carbon fiber thermoplastic rings are made using two different AFP systems: CONCOM's hot-gas-torch placement system, and the laser-heating setup shown in Figure 31.

The rings made using HGT are processed at a speed of 76-mm/s (3-in/s). The ones made using fiber laser setup are processed at the placement rate of 115-mm/s (4.5-in/s). A constant compaction force of 400N (90lbf) is applied for all the trials. SBS test is carried out according to ASTM D2344. The force versus displacement data is recorded and plotted by Hoskin Scientific Apparatus.

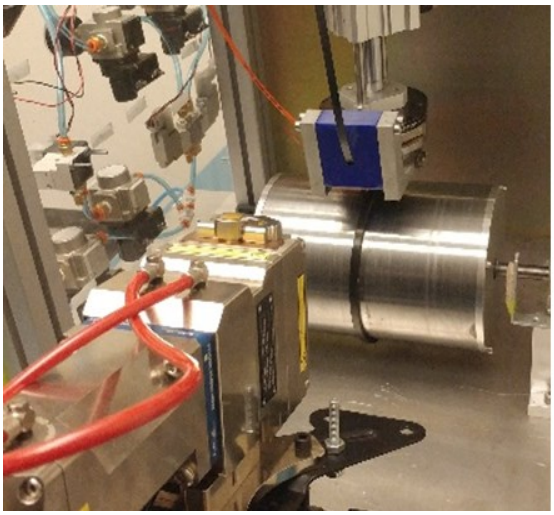

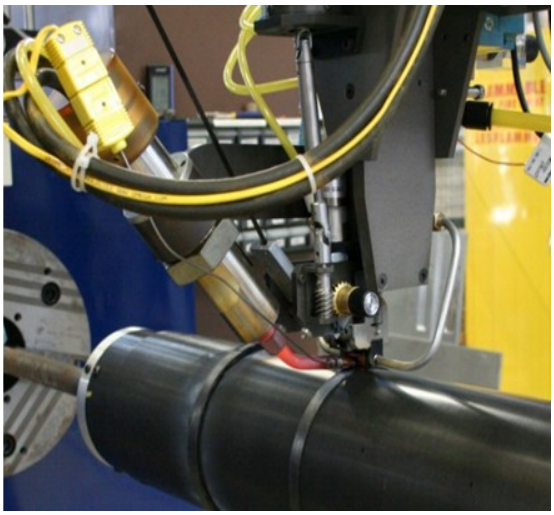

Figure 31: Left: Laser-Heating Setup; Right: Hot Gas Torch Setup

The first maximum load is recorded and the ILSS is calculated as per equation 4.1. A list of experimental trials and their associated ILSS results are tabulated below:

Table 10: Rings manufactured using HGT and fiber laser source heating

Trial #	Material ID	Heating Source	Placement Rate [mm/s]	Laser Power [W]	ILSS [MPa]	Standard Deviation	CV %
1	B	Laser	115	240	35.4	0.91	2.58
2	B	Laser	115	245	42.8	1.67	3.89
3	B	Laser	115	250	40.9	1.27	3.10
4	B	Laser	115	255	40.3	2.30	5.70
5	B	Laser	115	260	44.9	1.68	3.75
6	B	Laser	115	265	40.3	2.20	5.47
7	B	Laser	115	258	45.4	2.21	4.87
8	B	Laser	115	262	39.2	0.98	2.49
9	A	HGT	76	NA	27.7	2.86	10.3
10	B	HGT	76	NA	45.4	2.99	6.57
11	A	Laser	115	255	42.2	1.6	3.80

4.2.2 ILSS at Optimum Condition: laser heating vs. HGT

It is noted that material “A” and “B” exhibit similar performance when rings are made using the laser heating placement. Both materials reaches optimum ILSS for the laser power of 255-260 W. Material “B” however shows 7.6% improvement compared to material “A.” A notable difference between the two materials is their surface roughness. It is believed that a higher degree of mechanical bonding is achieved due to the higher surface roughness of material “B.” Also, tape “B” has a resin rich and a fiber-rich surface. During the placement process, the dry side of the tape is placed against the roller while the resin rich side faces the substrate. At elevated processing temperatures, the roller temperature also increases. The tape is therefore likely to bond to the roller surface, thus peeling away from the substrate. The dry side of the tape has an inferior bonding interface and delays this bond development; hence allowing material “B” to be processed at higher temperatures. The higher processing temperature enhances the degree of autohesion, and therefore better overall bonding is reached for material B. This limitation is emphasized for the HGT placement process where the roller interface temperature is raised to a much greater extent due to the blast of the hot gas. Hence it is the main reason for material “A” to exhibit a poor ILSS at trial nine where the tape bonded to the roller and was peeled away from the substrate.

Moreover, lower coefficient of variation and standard distribution of the ILSS data is indicative of a more uniform quality of samples. Less variation can be seen in the stiffness modulus shown in Figure 32 compared to ones in Figure 33 and Figure 34. More uniform quality of the laser-heating samples is mainly deemed to be due to the steady, uniform irradiance of the fiber laser as opposed to the unsteady blast of the hot gas through the nozzle.

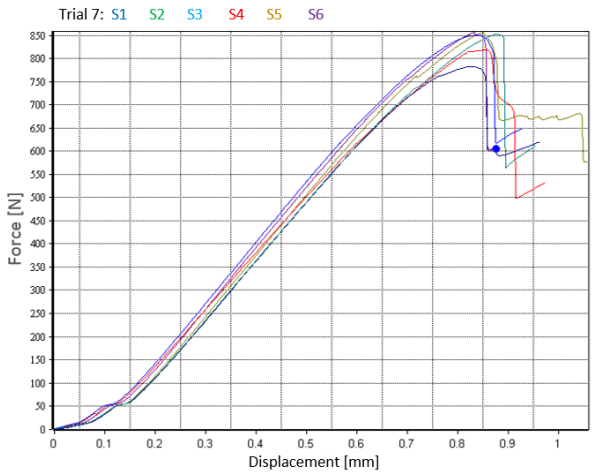

Figure 32: Trial 7: Material “B” Processed with Fiber Laser

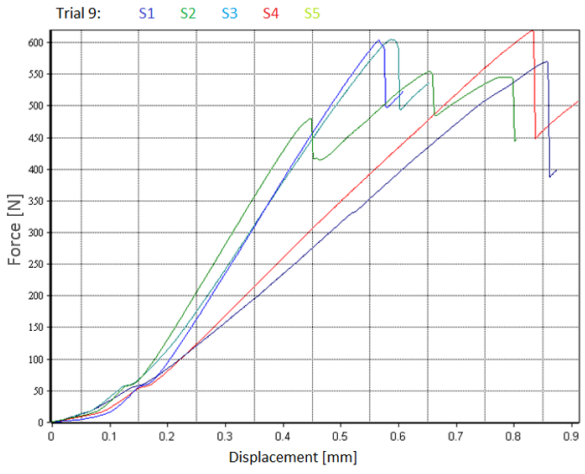

Figure 33: Trail 9: Material “A” processed with HGT

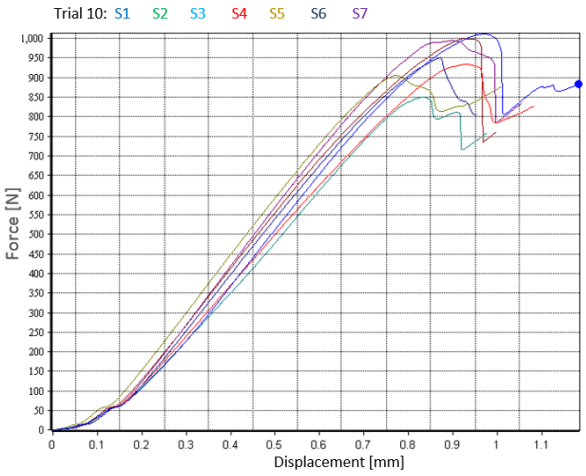

Figure 34: Trail 10: Material "B" processed with HGT

Lastly, it is noted that at the optimum condition (trial 7) the SBS test result of material “B” processed using fiber laser is matched to the SBS results of material “B” processed using HGT at trial 10, However material “B” is processed at 50% higher placement rate using fiber

laser heating compared to HGT. Since the heating system was the only variable of the study, it is fair to say that the fiber laser heating is at least 50% more efficient compared to HGT.

4.3 Increased Placement Rate and Its Effect on the Bond Strength

A rigid 12.7-mm (½-inch) steel roller is used to process the tape. Rings manufactured at 115-mm/s (4.6-in/s) using laser-assisted setup matched the quality of those processed at 3 in/s using the HGT system. 50% increase in lay-up speed without deterioration of quality, and overall, more uniform mechanical properties obtained earlier, is promising. Furthermore, a set of experiments are conducted to investigate the bond quality at higher placement rates.

4.3.1 Experimental Procedure

Based on the previous result the two variables selected for this study are the laser power and the placement rate. The CYTEC APC-2/AS4 tape system is used as the tape system due to exhibiting superior performance compared to TenCate PEEK/AS4 tape. All other variables remained unchanged such as the compaction force, tape tension, laser angle, etc. Table 11 lists the different processing conditions examined for this experiment. Placement rates of 90 to 150-mm/s, and laser power of 200 to 330-W are examined. 5 to 7 specimen per each ring are prepared for SBS test. The average ILSS obtained from SBS test, the standard deviation and the coefficient of variation are reported. The effective consolidation is determined similarly as described per the DOE experiment. To reach higher processing temperatures, the roller external cooling rate is doubled for trial 9, 10, and 11 to prevent the bond development between the incoming tape and the roller interface.

Table 11: Result of ILSS for various placement rates and laser power

Trail #	Factor A **Placement-rate mm/s (in/s)**	Factor B **Laser Power W**	Constant **Compaction Force N (lbf)**	ILSS **AVG 5 Samples MPa**	SD	% CV
1	89 (3.5)	200	400 (90)	36.5	1.23	3.4
2	89 (3.5)	210	400 (90)	39.1	2.18	5.6
3	89 (3.5)	215	400 (90)	39.9	1.44	3.6
4	89 (3.5)	220	400 (90)	38.6	3.17	8.2
5	102 (4.0)	200	400 (90)	35.9	4.41	12.3
6	102 (4.0)	210	400 (90)	35.4	1.81	5.1
7	102 (4.0)	215	400 (90)	31.4	1.22	3.9
8	102 (4.0)	220	400 (90)	42.0	1.95	4.5
*9	102 (4.0)	225	400 (90)	38.7	2.22	5.7
*10	102 (4.0)	230	400 (90)	39.0	1.11	2.8
*11	102 (4.0)	240	400 (90)	37.4	2.52	6.7
12	102 (4.0)	250	400 (90)	[NA]	[NA]	[NA]
13	127 (5.0)	255	400 (90)	32.2	1.77	5.5
14	127 (5.0)	270	400 (90)	34.0	3.03	8.9
15	127 (5.0)	280	400 (90)	42.7	4.19	9.8
16	127 (5.0)	290	400 (90)	[NA]	[NA]	[NA]
17	152 (6.0)	280	400 (90)	29.5	2.66	9.0
18	152 (6.0)	290	400 (90)	31.2	3.35	10.7
19	152 (6.0)	300	400 (90)	34.3	2.00	5.8
20	152 (6.0)	310	400 (90)	37.1	1.04	2.8
21	152 (6.0)	320	400 (90)	42.0	2.32	5.5
22	152 (6.0)	330	400 (90)	33.0	3.29	10.0
*	Trials with star are tested with twice the roller cooling rate					
[NA]	Matrix degraded due to excessive heat/Tape stuck to the roller/ ILSS not measured					

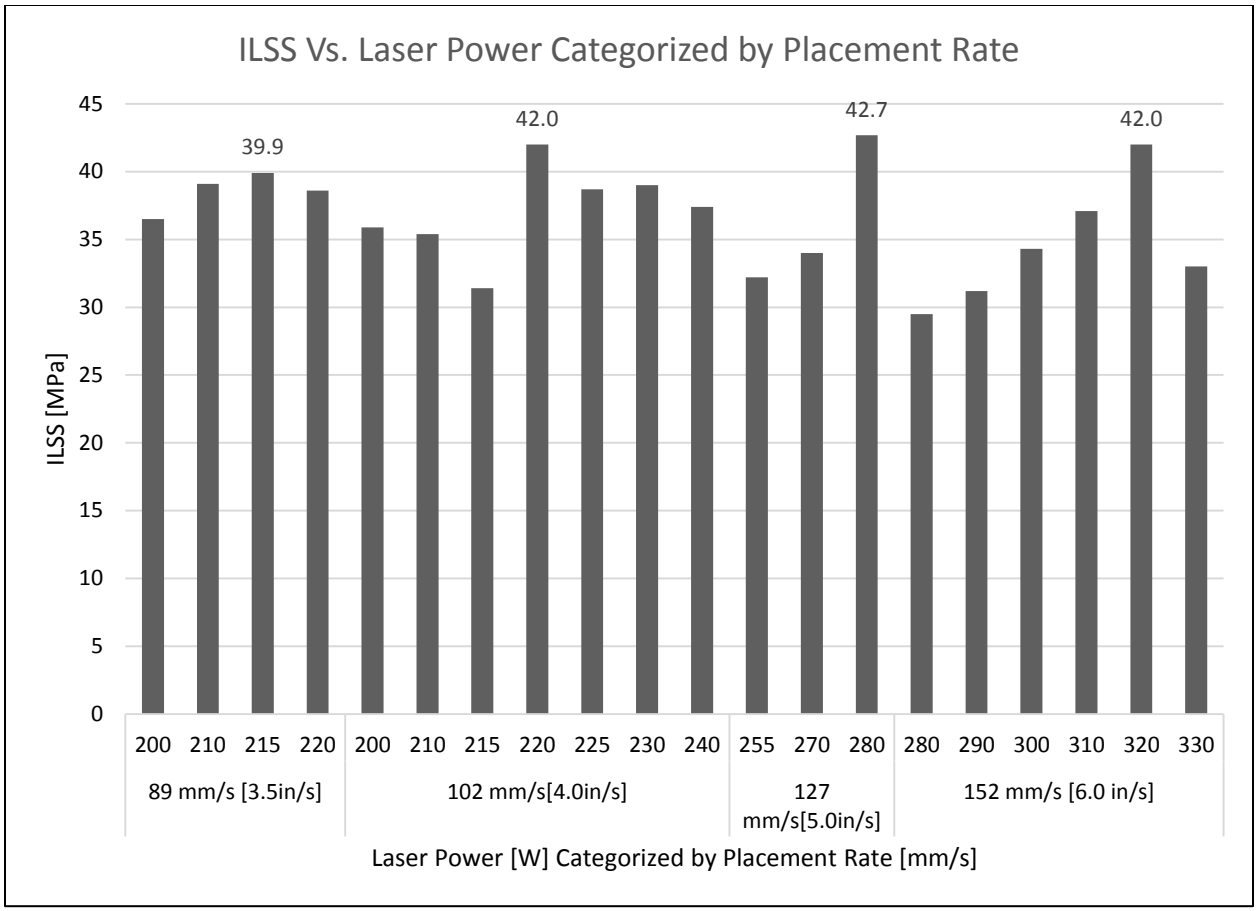

Figure 35: ILSS result for Laser Power vs. Placement Rate

Figure 35 summarizes the result of the above experiment. ILSS obtained from SBS test is plotted vs. Laser power, and Placement rate indicate that for each placement rate there exist a narrow range of laser power that results in an optimum ILSS. The increased heating rate was examined at about 100 mm/s placement rate. The increased heating resulted in higher matrix temperature which would have enhanced both the degree of intimate contact and Autohesion. However, the ILSS dropped for the laser power of 225W, 230W, and 240W most probably due to excessive heat which resulted in degradation of matrix, especially for the last few plies. It is recognized that the processing temperature increases for every successive ply for the winding – like process. Moreover, an excessive heat flux may have raised the temperature of the sub ply matrix beyond the glass transition temperature (T_g). Without any subsequent annealing raising, sub-ply temperature beyond T_g retards crystallization and would deteriorate the bond quality.

4.3.2 Photomicrograph Analysis

The failure mode of the selected specimen is analyzed using photomicrograph. Samples at optimum condition, near optimum, and least optimum based on ILSS results are selected for the analysis.

The specimen is cut at a plane perpendicular to the fiber direction using a diamond blade as shown in Figure 36.

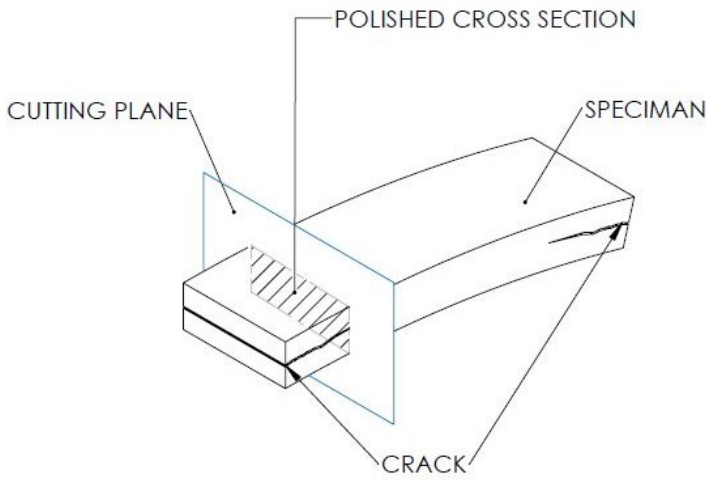

Figure 36: SBS specimen prepared for Micrograph Imaging

The cross-section is then polished and studied under the microscope as shown below. Both inter-laminar and intra-laminar failure modes are observed for the selected specimen. For samples processed at optimum or near-optimum processing conditions, intra-laminar failure is observed. Crack is propagated within the plies and crosses over the interface of adjacent plies. This is similar to results reported by Xiao for samples made using HGT placement setup [6]. However, the failure mode is different for those that are processed at non-optimum conditions. The intra-laminar failure mode transforms to inter-laminar as the non-optimum conditions are approached. This is to be expected as weaker inter-laminar bond exists for non-optimum conditions. Photo Micrograph analysis thus confirms the trend seen in the SBS test. Few micrograph images are included in appendix B.

4.3.3 Laser Power vs. Placement Rate at Optimum ILSS

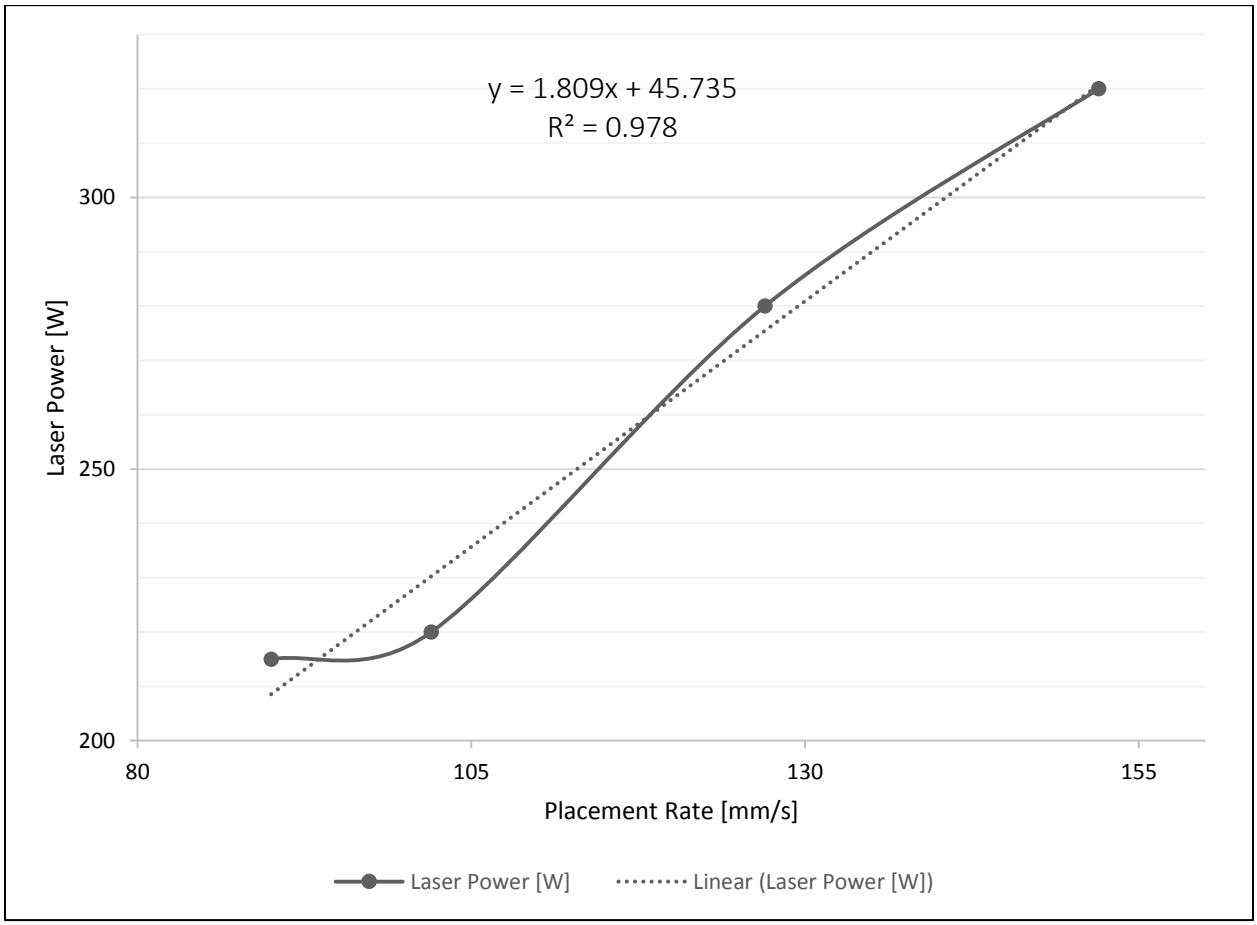

Figure 37: Plot of laser power [W] vs Placement rate [mm/s] at Optimum ILSS

Plotting the ILSS at optimum condition for the four placement rate studied above suggest a near-linear increase of laser power vs. the placement rate. Based on the above, it can be concluded that the effect of forced convection is negligible for the moderate placement rates. However, it is fair to note that the degree of intimate contact is not maintained and decreases with the increase in placement rate for the rigid roller. The challenge of maintaining the degree of intimate contact at higher placement rate can be addressed by using a conformable roller to increase the dwell time of the tape under compaction. Also, a higher processing temperature may be reached by de-localizing the heating. The current laser design produces a square spot size of 7 by 7 mm. It is recommended to expand the beam to a rectangle shape with an aspect ratio of 3 to 5 while maintaining a uniform intensity profile.

4.4 Laser Light Delivery and Effectiveness

To maintain bond quality at increased placement rates, it is recommended to de-localize the laser beam by expanding the current square spot size to a larger rectangular beam with 3 to 5 aspect ratio. The Gaussian beam leaving the optical cable is a highly divergent beam with a small diameter of 50 μm. To process the composite tape, however, the beam must be collimated, focused, and widened to at least match the width of the tape being processed. Additionally, a diffractive optical element (DOE) beam shaping lens is used to –ideally- transform a Gaussian beam with a conical profile to a square top-hatted beam with uniform intensity at the working distance.Hence an attempt is made to characterize the beam shape, and quality near, and away from the working distance.

4.4.1 Diffractive Optical Element Lens

The DOE lens is placed in the optical field of the beam and has a microstructure surface profile. "The micro-structured surface relief profile has two or more surface levels. The surface structures are either etched in fused silica or other glass types or embossed in various polymer materials" [55]. The profile is engineered to route the photons based on the shape and size of the spot. The spot shape could be elliptical, round, or rectangular. The resolution of the end-product depends on the design of DOE optic and the quality of the beam.

4.4.2 Experimental Procedure

An IPG is collimating and beam shaping module with water cooling is used here to expand the beam as shown in Figure 38. For the current set-up, a working distance (WD) of 300mm and a square beam of 6.5mm is targeted. The ideal profile of a square top-hatted beam is shown in Figure 39. However, the real output of the beam at the WD may deviate from the ideal profile depending on the design of the optics. The shape, uniformity, and sensitivity of the beam characterize the beam quality.

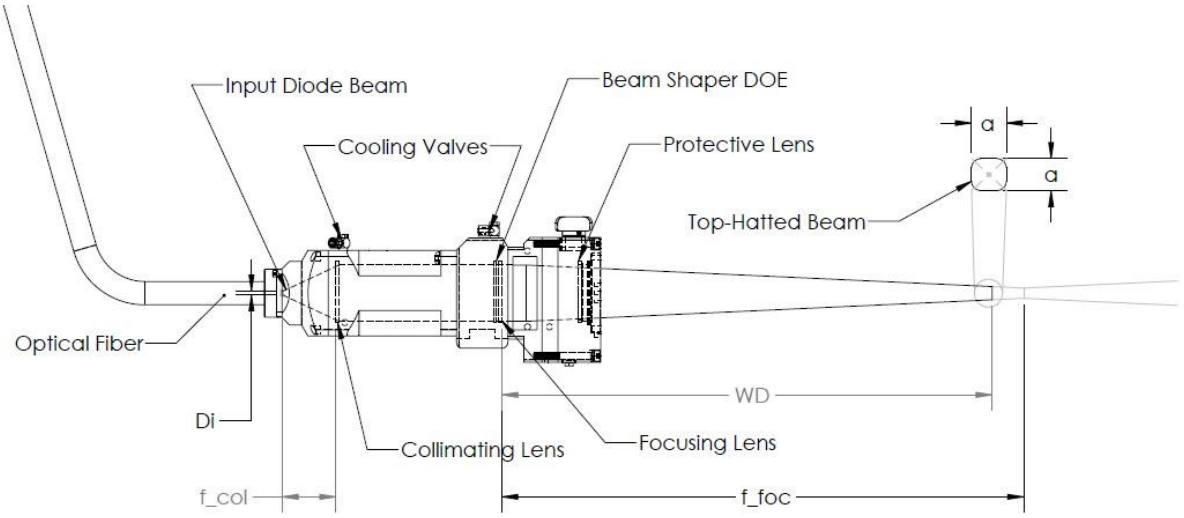

Figure 38: Collimating and beam shaping module for the Ring Manufacturing setup

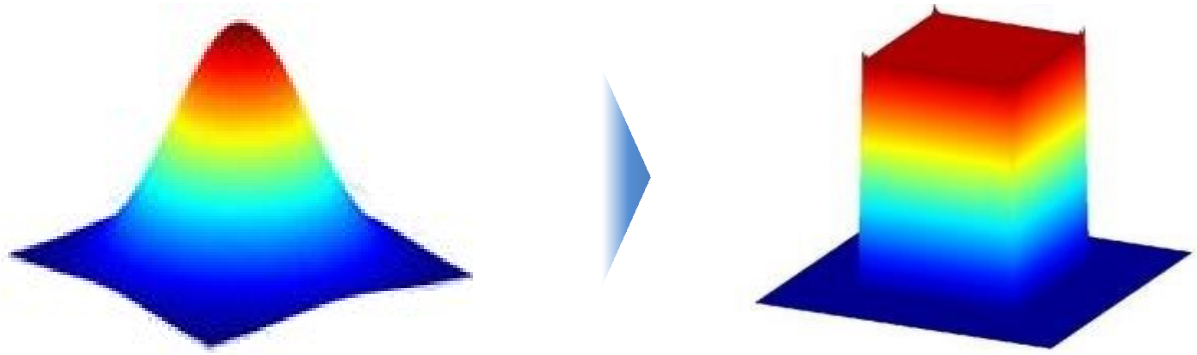

Figure 39: Transformation of a Gaussian beam (left) to top-hatted beam (right)

To measure the beam intensity and uniformity, a ceramic IR conversion screen rated for radiation of up to 3kW/cm^2 is used. The conversion screen absorbs two or more photons of the infrared radiation of 1064 nm wavelength light and emits a green light of a shorter 530 nm wavelength. A process which is referred to as “photon up conversion” effect. The green light is on the visible spectrum, and the reflected spot can be used to align the beam.

A FLIR thermal camera is employed to capture the 2D radiance profile of the beam reflected from the conversion screen at locations in front, and behind of the working distance.

The surface temperature of the conversion screen is recorded for 10 seconds of continuous wave emission of 220 W. The surface temperature reaches a steady state during this time. The image is then analyzed using FLIR thermal image software. The spot size, room temperature, average spot temperature, as well as the minimum (cold) spot and maximum (hot) spot temperature are recorded. The images of the radiance profile at various axial distances from the nip point are presented in the figure below.

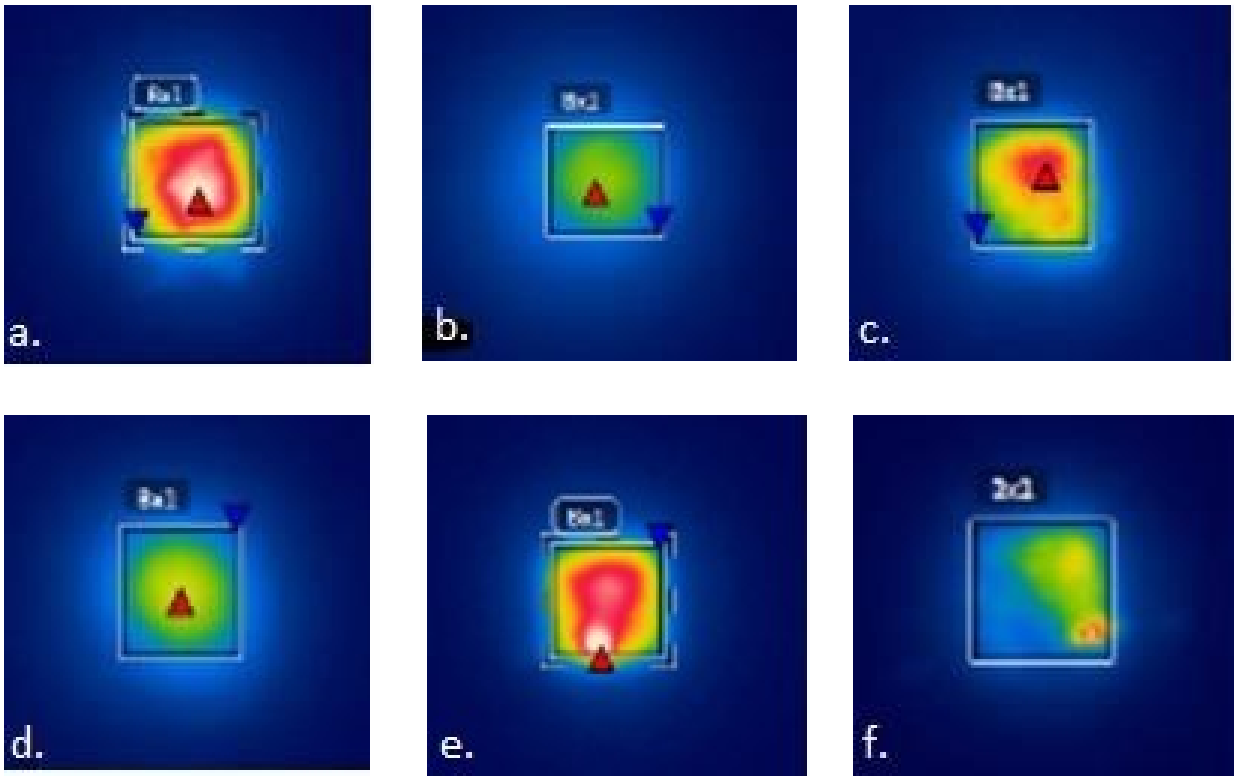

Figure 40: Conversion screen surface temperature at various distances from the working distance

Table 12: Axial position of the laser beam spot away from the working distance

a.	At WD	b.	-25.4-mm (- 1.00-inch)	c.	+19.0-mm (+.75-inch)
d.	+25.4-mm (+1.00-inch)	e.	+50.8-mm (+2.00-inch)	f.	+76.2-mm (+3.00-inch)

4.4.3 Gaussian Beam Profile Intensity Variation

The 2D profile measurement of the beam at various axial locations shows that the beam intensity and uniformity are quite sensitive to axial distance variation. The absolute temperatures tabulated below are used for comparison of the radiance profiles and are not the actual surface temperatures of the ceramic screen. For the actual measurement, a laser beam profiler is required. For a comparison study however only the delta average temperature is of interest. The percentage difference in the average temperature tabulated below shows the reduction in the average flux radiance and consequently laser effectiveness η_n:

$$\eta_n = \frac{P_{eff}}{P_{in}} \tag{4.4.1}$$

Table 13: Temperatures recorded for different radiance profiles

Location	Hot Spot Temp. [°C]	Cold Spot Temp. [°C]	Average Temp. [°C]	Delta Ave. Temp. [%]	Laser Effectiveness η_n
a.	150	64	115	0	0.95
b.	90	52	77	-33	0.63
c.	134	56	97	-16	0.80
d.	98	56	80	-30	0.66
e.	177	60	114	0	0.95
f.	136	44	66	-43	0.54

Assuming a 5% losses through optics, η_n is calculated for the radiance profiles. It is noted that the shape and the intensity of the profile is sensitive to variation from the working distance. Also that there is a large gradient between the cold and hot spot detected by the FLIR camera. The non-uniformity of the beam resulting from this gradient can cause resin degradation at the hot spot and inadequate consolidation around the cold spot. Both of which will deteriorate the mechanical properties of the beam.

The beam at the nip point is off-focused, and there are two distinct locations at which the radiance is near-uniform: one behind the beam waist, and one after as shown in Figure 41. The intensity fades away as the distance increases from the WD. This introduces a limitation on the size of the beam. A large rectangular shaped beam is often used to preheat the tape and the substrate to enhance bonding. Better bonding is achieved due to the larger wetted area which

increases the thermal efficiency. Thermal efficiency is the ratio of the amount of heat required to raise the matrix temperature above T_m to the total amount of heat delivered:

$$\eta_{th} = \frac{vS_m C_m}{P_{eff}} \tag{4.4.2}$$

whereas v is the placement rate; S is the cross sectional area of the molten matrix; and C is the heat content per unit volume of the molten matrix [56].

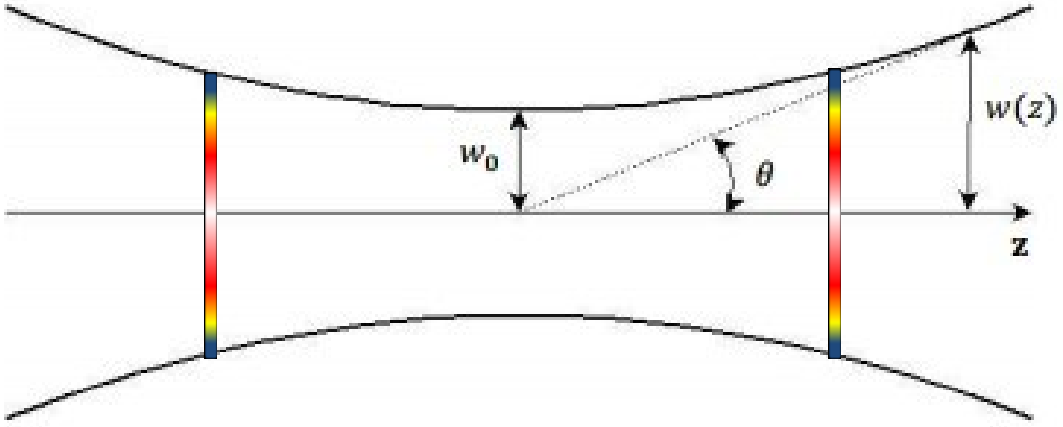

Figure 41: Gaussian beam axial propagation and the location of two unique, focused spots

However the larger the beam, the larger will be the wetted area away from the WD, and the weaker will be the area averaged beam intensity as a result. The variation in intensity follows a Super-Gaussian radiance intensity:

$$I(P, r, z, n) = \frac{P_{in}}{\frac{\pi}{2}\omega^2(z)} e^{-2(\frac{r}{\omega(z)})^n} \tag{4.4.3}$$

where P_{in} is the Gaussian beam power; ω is the beam radius; z is the axial distance from the beam waist; r is the beam radial location; and n is the order of a Super-Gaussian beam. As the order n increases the Gaussian beam transforms toward a flat, top-hatted beam with sharp edges [57]. For on-axis intensity:

$$I_{axis}(z) = \frac{P_{in}}{\frac{\pi}{2}\omega^2(z)} \tag{4.4.4}$$

where $\omega(z)$ *is the beam waist at any axial location*:

$$\omega(z) = \omega_o \sqrt{1 + (\frac{z}{z_R})^2} \tag{4.4.5}$$

By knowing $I_{axis}(z)$ and I_o the laser effectiveness η_n can be measured at any axial distance. A uniform intensity radiance assumption for any thermal model would be an over simplification of the process. Estimation of the effectiveness is in fact necessary to have a representative process thermal model.

In practice, Effectiveness can be improved by increasing the angle of the incoming tape, away from the substrate. However, this is achieved at the cost of a reduction in the wetted area. An alternative approach is to reduce the sensitivity of the beam. The sensitivity of the beam can be characterized using Rayleigh length, z_R which is the axial distance from the waist to where the beam width is doubled:

$$z_R = \frac{\pi {\omega_o}^2}{M^2\lambda} \tag{4.4.6}$$

whereas ω_o is the beam waist, λ is the beam wavelength, and M^2 factor is the deviation of the laser beam from a perfect Gaussian beam. The profile is less sensitive to axial distance variation for a large Rayleigh length. To maximize z_R the beam waist is to be maximized and M^2 factor to be minimized. This is achieved by having a larger input beam diameter D_i for the same magnification power (MP):

$$\omega_o = MP \times D_i = \frac{f_{foc}}{f_{col}} D_i \tag{4.4.7}$$

whereas f_{foc} and f_{col} are the focal length of the focusing lens, and of the collimating lens respectively. Lastly the divergent angle θ as shown in Figure 7 is:

$$\theta = \frac{M^2 \lambda}{\pi \omega_o} \tag{4.4.8}$$

The current laser setup has an input diameter of 50 μm, magnification of 4.2 and M^2 factor of 1.11 resulting in a long Rayleigh range of 107mm. The sensitivity could be further reduced by increasing the magnification power which presently is constrained due to the hardware design.

4.5 Silicone roller: Material Characterization and Fabrication

It is known that the degree of intimate contact decreases with the increase in placement rate according to the equation 2.6 derived by Mantel from Lee and Springer intimate contact model. As a result of the degree of bonding which is a product of the degree of intimate contact and degree of autohesion (healing) diminutions. To prevent the decline in the degree of intimate contact at higher placement rates, the compaction area is often increased using conformable silicone rollers in the laser heating process as shown below. The silicone material can be transparent to NIR light of 1064 nm wavelength emitted from the Ytterbium element. With sufficient air or water cooling, the silicone material can withstand the extreme processing temperatures of the nip point.

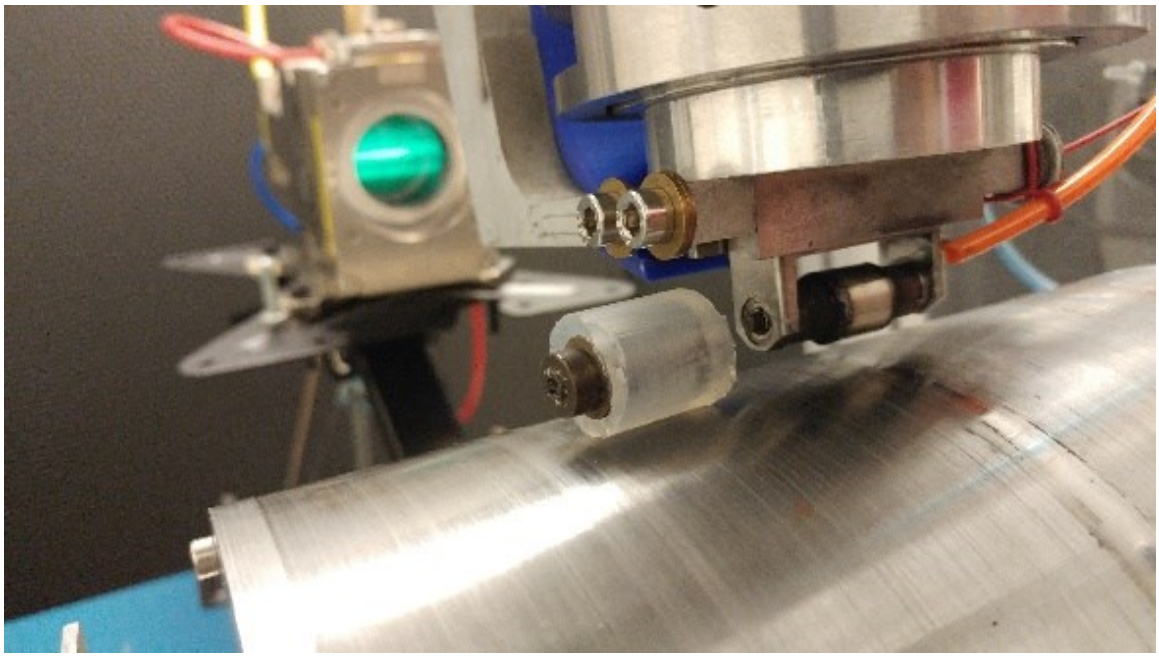

Figure 42: Silicone roller vs. rigid steel roller installed on the laser heating setup

4.5.1 Silicone Roller Fabrication

A colorless silicone material is used for fabrication of a conformable roller. BLUESIL™ RTV 3040, distributed by Freemen Manufacturing and Supply Co. is a clear high strength, addition cure silicone rubber compound used in this experiment. RTV3040 has a relatively low viscosity (50000-mPa.s) which makes the product feasible for molding applications. It can be mixed with several catalysts to produce hardness from 20 to 45 Shore A. The current catalyst provides a hardness of 38 ShoreA cured at room temperature, and a service temperature of negative 54 to 204 ºC.

Due to low hardness of the silicone rubber, a 50.8 mm (½ inch) diameter steel roller is used as a core to provide adequate stiffness to the 19.0 mm (¾ inch) rubber roller as shown in Figure 42. However, this is not desired as the steel roller absorbs the laser light, and can heat up excessively inside the roller.

The mold of the silicone roller is 3D printed using ABS plastics. The resulting surface of the roller is rough and should be polished, machined using a lathe. To machine the rubber, it is recommended to cool the material using liquid nitrogen until it hardens. However, the material used here is shattered upon freezing inside liquid nitrogen. Hence the surface remains unfinished.

Another noteworthy limitation is the size of the roller of 19.0 mm diameter which is the largest that could be installed using the current roller bracket. A larger roller bracket should be machined to accommodate larger conformable roller size.

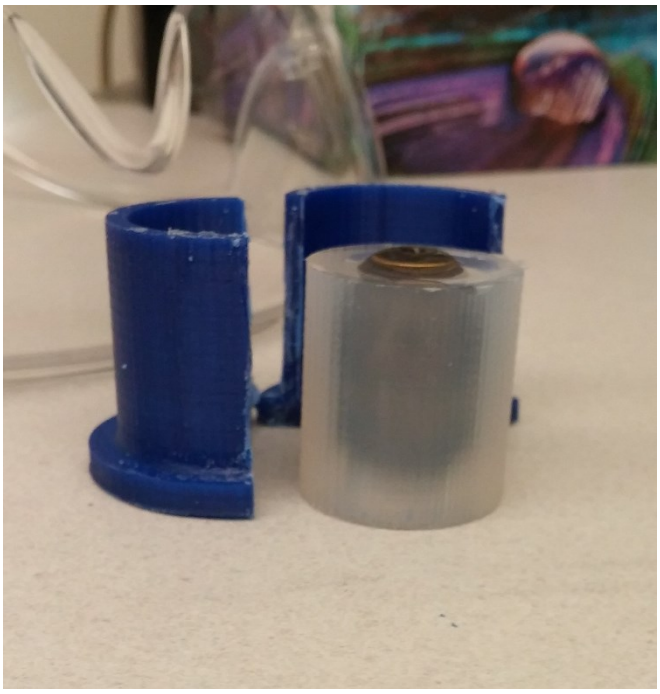

Figure 43: Silicone roller molded around a steel roller core

4.5.2 Material Characterization Using Spectrophotometry

It is important for the silicone material to be transparent to NIR light. Cary 5000 UV-Vis-NIR Spectrophotometer (Varian) is used to measure the transmittance of the RTV3040 silicone rubber compound. The instrument used here can measure transmittance for light ranging from 190 to 3300 nm. The result of transmittance measurements for the light rang of 900 to 1100 nm is presented in appendix C. For 1064 nm NIR light the transmittance is 38.1%.

The result obtained here suggests that the RTV3040 is semi-transparent and may not be suitable for the leaser-heating process. A more transparent silicone roller is preferred for fabrication of the conformable roller. Few attempts are made to process the tape using the conformable roller. Despite external air cooling, the silicone softens after the placement of 8 to 10 successive plies after which the compaction force is deemed ineffective.

It is also believed that the silicone roller has a different operating interface temperature than the steel roller. The roller acts as a heat sink in this process, and the different thermal

characteristic would result in a variation of processing temperatures. To identify this difference, the thermal history is measured.

4.6 Nip Point Temperature Measurement

Based on the result obtained in section 4.4 it is shown that the ILSS is highly sensitive to the laser power. The laser power determines the processing temperature at the nip point. In fact, there exist only a narrow range of processing temperature that would result in an optimum ILSS. Insufficient or excessive heat is shown to deteriorate the bonding.

The degree of bonding is a function of the nip-point temperature, placement rate, compaction force, and compaction time according to equations 2.3.6, 2.3.13, and 2.3.15. It is necessary to obtain the process temperature, as well as the thermal history of the winding-like placement process to assess the degree of bonding using the Lee and Springer thermal model.

4.6.1 Experimental Procedure

Two 0.127-mm (5thou-in) fine wire thermocouples (TC) are used to measure the processing temperature at the nip point. The placement rate is fixed at 117-mm/s (4.6-in/s), and the TCs are placed 15-Hz distant from each other on the substrate surface. Measurements are made for laser power of 220 and 260-W. Thermocouples joints are shielded using insulating polyimide Kapton-H® films. An Omega OMB-DAQ-2408 data acquisition unit is used to process, and transmit thermal measurements at 15-Hz. The DAQ unit has a built-in cold junction compensation (CJC) to compensate for electromagnetic field noise from connecting TC to the device terminal block. Once the Analog and CJC data is collected, the data is linearized an averaged out before transmitted to the computer [58]. A differential TC connection is shown in Figure 44. By mounting the DAQ system on the mandrel assembly, and locating a laptop computer beside the setup as shown below thermal measurement data was collected for up to 4 successive layers. The recording of the data started and stopped before the initiation, and after the completion of the placement process when the laser emission is off. The data of channel pairs for each trial is plotted below.

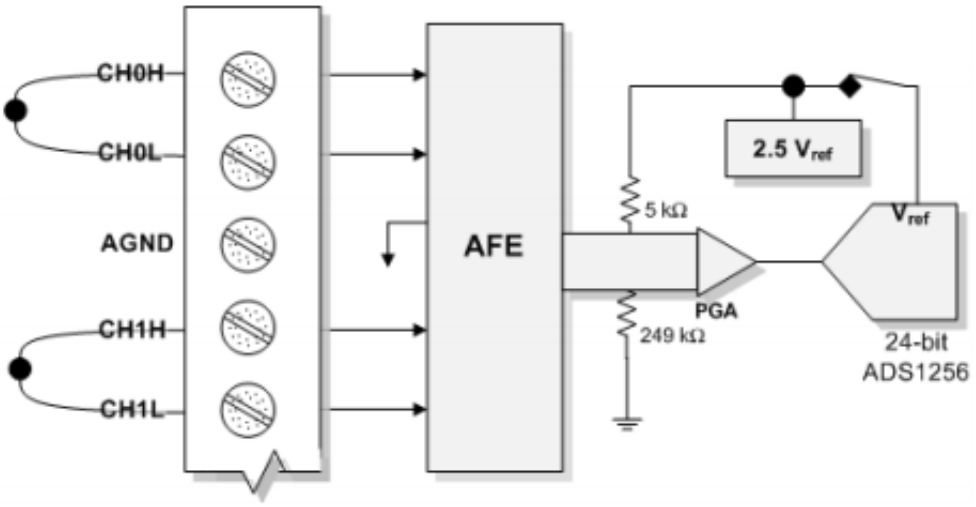

Figure 44: TC connection to OMB-DAQ-2408 *[58]* Figure 7

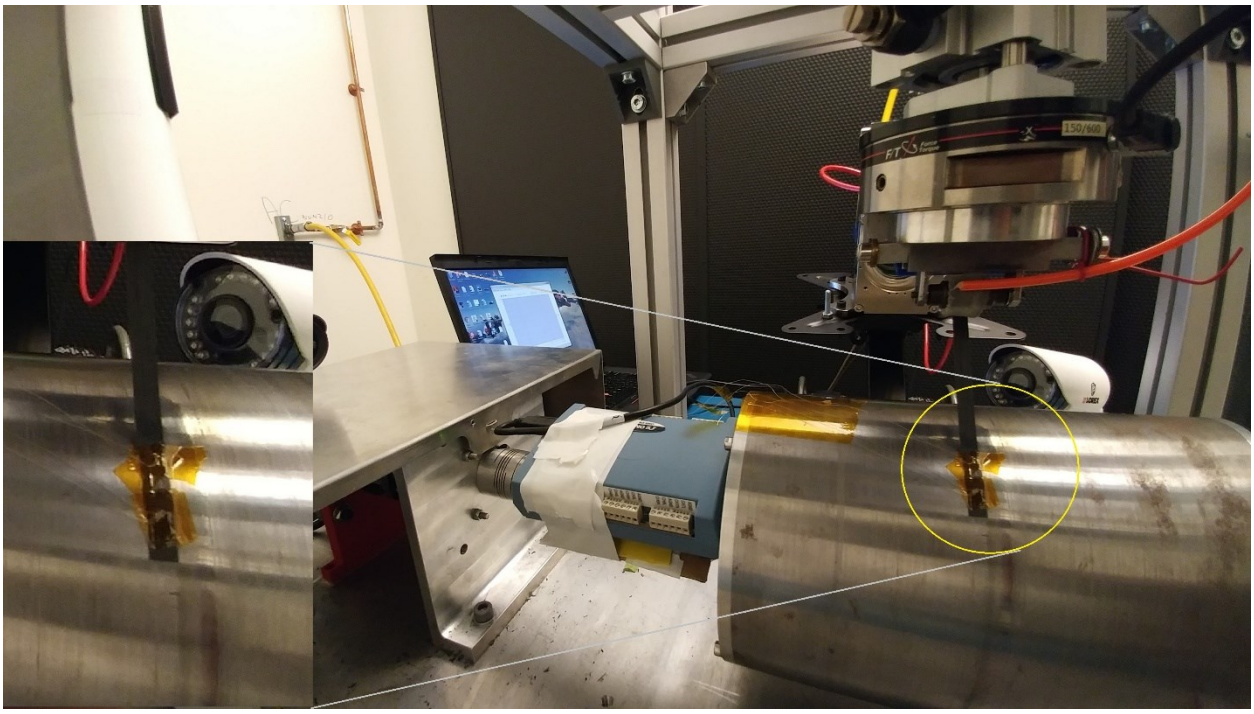

Figure 45: Thermocouple and DAQ unit set-up

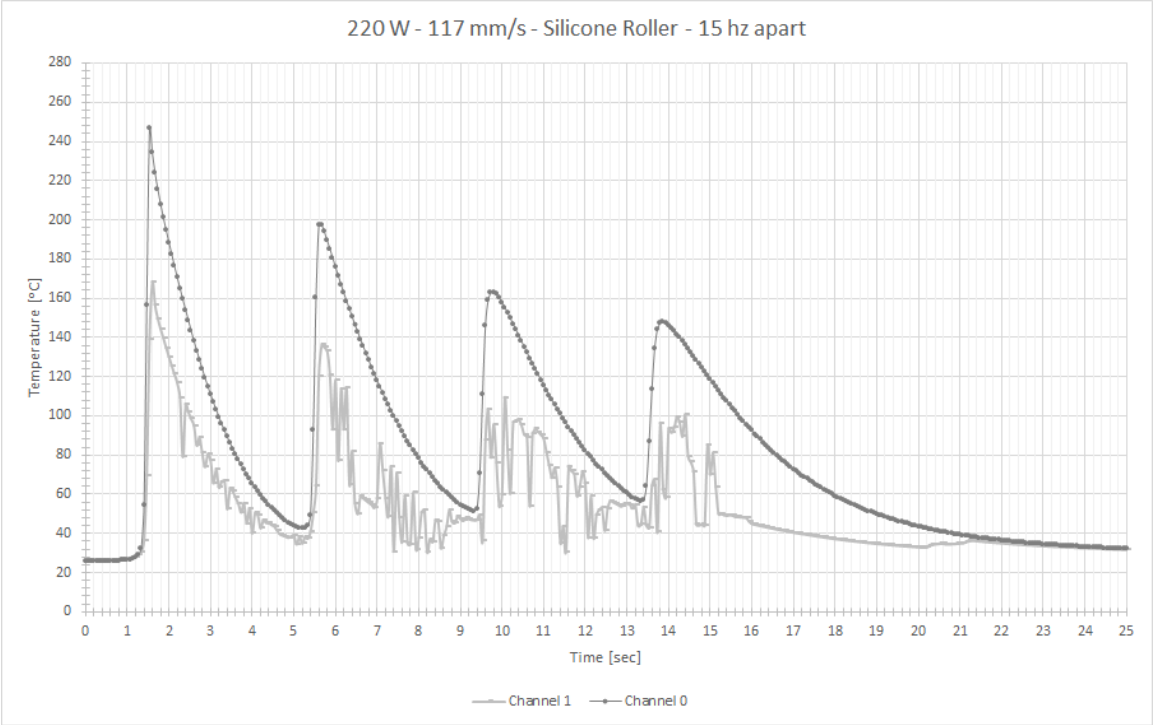

Figure 46: Nip Temperature Measurement - Silicone Roller- 220W- 117 mm/s –TC 15Hz apart

Figure 47: Nip Temperature Measurement - Steel Roller- 220W- 117 mm/s –TC 15Hz apart – Trial 1

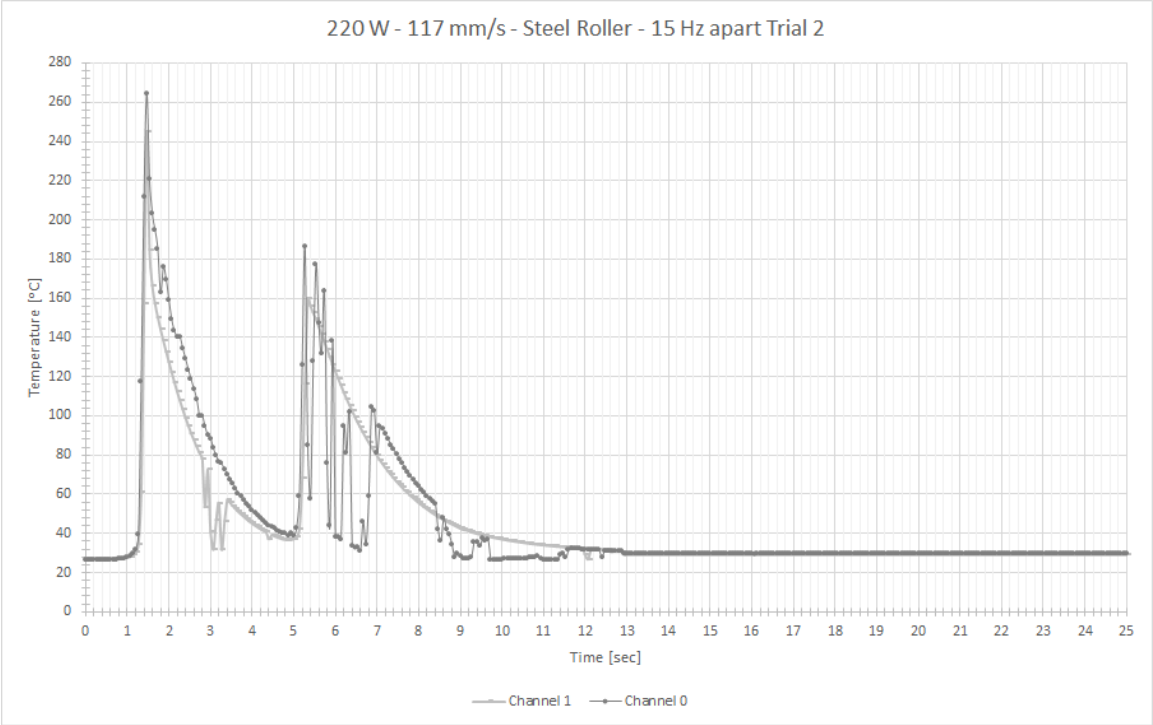

Figure 48: Nip Temperature Measurement - Steel Roller- 220W- 117 mm/s –TC 15Hz apart – Trial 2

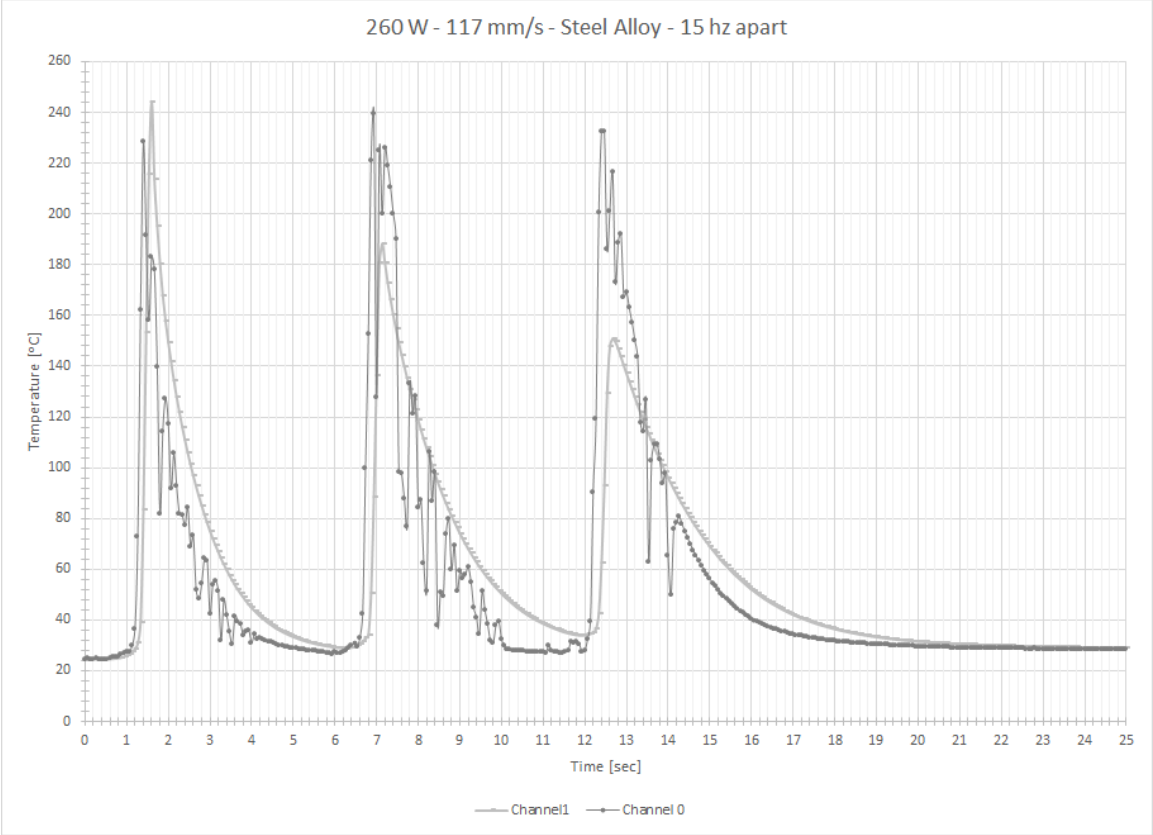

Figure 49: Nip Temperature Measurement- Steel Roller- 260W- 117 mm/s –TC 15Hz apart

4.6.2 Interpretation of the Thermocouple Measurements

The absolute degree of the nip point temperature measured using the 0.127-mm diameter bare wire thermocouples at 15-Hz is far away from the expected nip point temperature. The absolute measured levels remain below 343ºC for both 220 and 260-W which is below the melting temperature of PEEK. If the measured data is accurate one would expect a minimal or no bonding at such temperatures. Moreover, the measured temperature at 260W is lower than those measured at 220W for the same roller material. Hence the absolute measurements are deemed to be inaccurate.

There is also inconsistency in the measurement of the TC pair. At least one TC per trial: channel-1 in Figure 46, channel-0 in Figure 47, channel-0 in Figure 48, and channel-0 in Figure 49 displays inconsistent measurement. This inconsistency is due to the noise and the inadequate response time of the thermocouple as shown below. For a five thou inch diameter wire, the response time is about 0.1 seconds. Implicating that faster data acquisition and processing does not translate to higher measurement resolution.

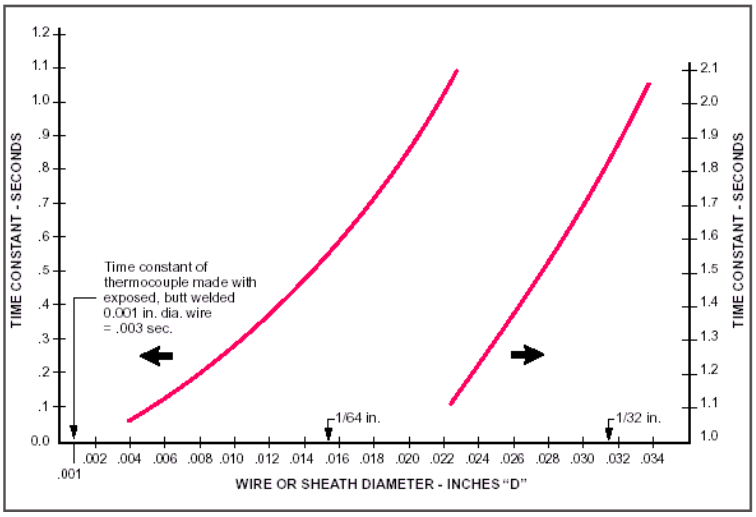

Figure 50: Response time of bare wire thermocouples *[59]*

Where the "time constant" or "response time" is defined as the time required to reach 63.2% of an instantaneous temperature change *[59]*. The material is heated at the nip point for an axial distance of about 3.5-mm. At 117-mm/s the consolidation process takes place in less than 0.03-sec. A TC response time, at least, 10 times lower than the consolidation time is required for attaining adequate resolution. According to the above figure the required resolution can only be

achieved using a 1 thou inch diameter wire thermocouple which may be difficult to handle and install on the current set-up. Moreover, the higher resolution does not guarantee higher accuracy or consistency in the measurement as the noise level increases for a finer gauge TC.

The recorded thermal history for the silicone and the steel roller is as shown below. The selected measurements display consistency and the "right" trend in terms of the absolute levels.

Several observation can be made from the attained results. Firstly, the peak nip point temperature is lower when the silicone roller is used. This result is expected as the silicone roller has lower thermal conductivity and lower light absorbency compared to the steel roller.

Secondly, the substrate temperature increases upon placement of each successive layer. The result suggest that the substrate and/or roller interface are at elevated temperature prior to the placement of each subsequent ply.

Lastly it is noted that the temperature of the preceding layer raises to as high as 80% of its successive layer. This is an important observation which suggests that the bonding of up to two preceding layers may be affected at each pass assuming the processing temperature of 600ºC or above is reached as reported in the literature [46]. Therefore the bond strength is an accumulative sum of multiple passes.

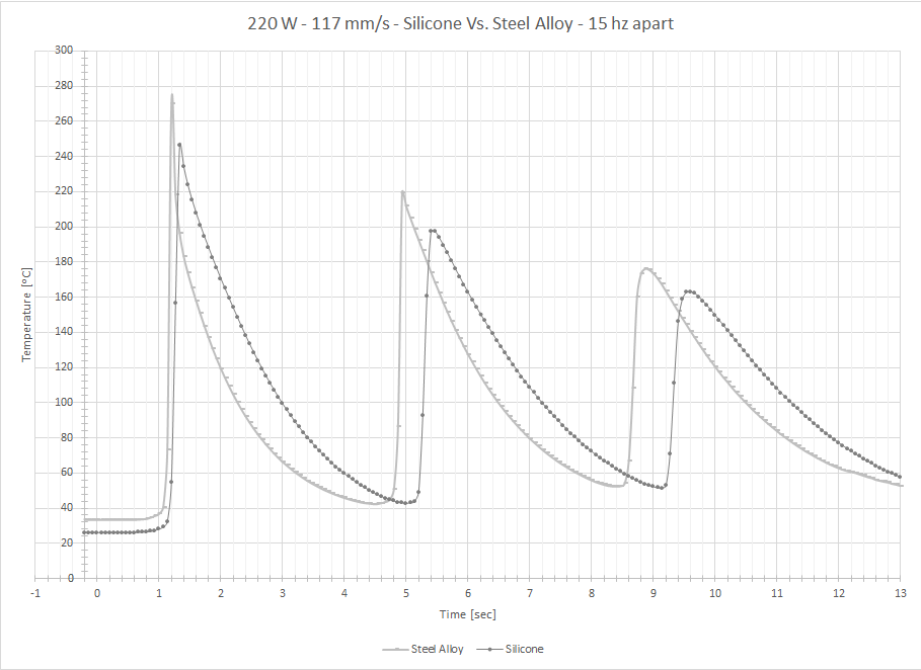

Figure 51: Nip Temperature Measurement – Silicone vs. Steel Roller 220W -117mm/s

CHAPTER 5: CONCLUSION AND FUTURE WORK

A ring manufacturing set-up is designed to investigate the effect of the laser-assisted placement process parameters on the bond strength of CFRTP unidirectional tapes. A high power, 2000-W Ytterbium fiber-laser is used as the heat source to apply a steady, uniform, instantaneous, and localized heat for a more efficient in-situ consolidation.

Design of experiment using the Taguchi approach is employed to efficiently study the combined effect of placement rate, laser power, and compaction force on the ILSS of the rings. It is found that the compaction force beyond a certain degree has a negligible effect on the bonding strength in comparison to the placement rate and the laser power. A near optimum processing window is identified based on the SBS data. Two different material systems are then examined using laser heating and hot gas torch setup. Matching bonding quality is reached at 50% higher placement rate for the rings made using the laser-assisted placement setup. Better uniformity is exhibited at the optimum condition. It is also shown that the two material systems with different characteristics affect the bond quality.

Higher placement rates are further investigated using the laser heating setup. The effect of increased placement rate on bond quality is studied. It is shown that for a rigid roller, the bond quality deteriorates at higher placement rates. To enhance the degree of bonding, the use of a conformable roller and a wider laser beam is recommended to maintain the degree of intimate contact and increase the degree of autohesion respectively. Hence, an attempt is made to fabricate a silicone roller and characterize the laser beam. It is found that a stiffer, more NIR-light transparent silicone roller, with internal cooling is required for an effective pressure application and higher service temperature. It is also noted that the intensity and effectiveness of the light beam diminutions as it expands away from the designed working distance or the nip point. A high Rayleigh range and magnification are required to reduce the sensitivity of the beam at the nip point for a given laser output beam diameter.

Finally, the nip point temperature is measured using fine wire thermocouples. It is noted that due to the low thermal response and high noise, the absolute value of temperatures measured is inconsistent. However, the plot of the thermal history suggests that the nip point temperature increases during the ring manufacturing process for each successive ply. Hence, to sustain the

nip point temperature at a desired level, the laser power shall vary for the winding-like process. The thermal history also indicates that the bondings of up to two proceeding plies are affected during each pass for a recommended processing temperature of 550 to 600ºC. The degree of bonding is therefore an accumulative sum of bond strength of multiple intervals.

The study presented here confirms the higher efficiency of the fiber laser heating source in comparison to the HGT. Similar or better bond strength is achieved using the laser fiber heat source at higher placement rates given all other paramters remain unchanged. While the bond strength provides a good indication of the laminate quality, further studies are required to ensure that the microstructure is not considerably degraded due to the higher placemnet rate. One would expect that the void content and crystallization suffer from the higher placement rate attempted during the laser-heating process. it should be noted however that similar set-up, the same roller geometry and compaction force are used for the comparison study. Also that the bond strength is affected directly by the void content. Hence an increase in interlaminar void content would have translated to a degredation in bond strength. The effect of higher placement rate on the crystallization here is minor. A look at the measured nip temperature data indicates a plus 1000ºC/min cooling for all of the trials. Therefore similar crystallinity is expected for all samples at optimum condition. A qualitative study of the void content using the micrograph analysis could verify the integrity of the samples processed at higher placement rates.

Overall, attaining a robust process is more feasable with the laser fiber as the main heating source is spatial and temperal controlled. However for enhanced efficiency of the process use of multiple tows and lasers can be more effective than over expanding the laser beam or over escalating the power.

For future work the laser-heating set-up may be re-designed to be mounted on a gantry table to make flat laminate. Measurement of the thermal history, and the compaction pressure would become more feasible on a flat tool. Accurate measurements of these paramters are cruicial for developing an optical-thermal model without which, a model would be subjective to a particular end-effector design or a geometry.

A response surface DOE can be designed to study the two-way interaction of parameters in future work. Upon development of a parameterized optical thermal model the use of a

Differential Evolution (DE) model or the application of a sorragate model for constrained and multi objective optmization could be considered.

REFERENCES

[1] Khan M.A., Schledjewski R., "Influencing factors for an online consolidation process," in *17th international conference on composite materials*, Edinburgh, 2009.

[2] M. A. Khan, P. Mitschang, R. Schledjewski, "Parametric Study on Processing Parameters and Resulting Part Quality Through Thermoplastic Tape Placement Process," *Journal of Composite Materials,* vol. 47, no. 4, pp. 485-499, 2012.

[3] Comer A.N., Hammond P.E., Ray D.I., Lyons J.O., Obande W.I., Jones D.A., O'Higgins R.O., McCarthy M.I., "Wedge peel interlaminar toughness of carbon-fibre/PEEK thermoplastic laminates manufactured by laser-assisted automated-tape-placement (LATP)," in *CETEC14*, Finland, 2014.

[4] Stokes-Griffin CM.J., P. Compston, The effect of processing temperature and placement rate on the short beam strength of carbon-fibre-PEEK manufactured using a laser tape placement process, Composite Part A: Applied Science and Manufacturing. 78:247-283., 2015.

[5] C. M. Stokes-Griffin and P. Compston, "Laser-Assisted Tape Placement of Termoplastic Composites: The Effect of Proces Parameters on Bond Strength," in *Sustainable Automotive Technologies 2013 Proceedings of the 5th International Conference ICSAT 2013*, Ingolstadt, 2013.

[6] X. Cai, "Determination of Process Parameters for the Manufacturing of Thermoplastic Composite Cones Using Automated Fiber Placement," A Thesis in Department of Mechanical and Industrial Engineering at Concordia University, Montreal, 2012.

[7] Beyeler E., Phillips W., Güçeri S.I., "Effects of processing on laser assisted thermoplastic tape consolidation," *Composites Part A,* vol. 26, no. 9, pp. 669-673, 1997.

[8] Agrawal V., Mccullough R.L., Schultz J.M., "The thermoplastic laser-assited consolidation process - mechancial and microstructure characterization," *Thermoplastic Composite Materials,* vol. 9, no. 4, pp. 365-380, 1996.

[9] Rosselli F., Santare M.H., Guceri S.I., "Effects of processing on laser assisted thermoplastic tape consolidation," *Composites PartA: Applied Science and Manufacturing,* vol. 28, no. 12, pp. 1023-1033, 1997.

[10] Mazumdar S.K., Hoa S.V., "Application of taguchi method for process enhancement of on-line consolidation technique," *Composites,* vol. 26, no. 9, pp. 669-673, 1995.

[11] S. Grove, "Thermal modelling of tape laying with continuous carbon fibrereinforced thermoplastic," *Composites,* vol. 19 Number 5, 1988.

[12] Yousefpour A., Ghasemi Nejhad M.N., "Experimental and computational study of APC-2/AS4 thermoplastic composite C-rings," *Thermoplastic Composite Material,* vol. 14, no. 2, pp. 129-145, 2001.

[13] Chang I.Y., Lees J.K., "Recent development in thermoplastic composites: A review of matrix systems and processing methods," *Thermoplastic Composite Materials,* vol. 1, no. 3, pp. 277-296, 1998.

[14] Grouve W.J., Warnet L.L., Rietman B., Visser H.A., Akkerman R., "Optimization of the tape placement process parameter for carbon-PPS composites," *Composites Part A: Applied Science and Manufacturing,* vol. 50, no. 1, pp. 44-53, 2013.

[15] Pistor C.M., Yardimci M.A., Güçeri S.I., "On-line consolidated thermoplastic composites," *Composite Materials,* vol. 33, no. 4, pp. 306-324, 1999.

[16] Yassin K., Hojjati M., "Processing of thermoplastic matrixx composites through automated fiber placement and tape laying mathods, A review," *Thermoplastic Composite Materials,* 2017.

[17] R. Schledjewski, Thermoplastic tape placement process - In situ consolidation is reachable, Plastic, Rubber and Composites. 38(9-10): 379-386, 2009.

[18] Williams F., Brown M., "Xenon flashlamp heating for automated fiber placement," in *3rd International Symposium on Automated Composite Manufacturing*, Montreal, 2017.

[19] W.I. Lee, G.S. Springer, "A model of the manufacturing process of thermoplastic matrix composites," *Journal of Composite Materials,* vol. 21, pp. 1017-1055, 1987.

[20] Yang F., Pitchumani R., "A fractal Cantor set based description of interlaminar contact evolution during thermoplastic composite processing," *Material Science,* vol. 36, pp. 4661-4671, 2001.

[21] Mantel S., Springer G., "Manufacturing process models for thermoplastic composites," *Composite Materials,* vol. 26, no. 16, pp. 2348-2377, 1992.

[22] Mark B., Gruber J., Tierney J., Brian J., Jensen et al., "Thermoplastic in situ placement requires better impregnated tapes and tows," in *SAMPE*, Baltimore, 2012.

[23] Yang F., Pitchumani R., "Nonisothermal healing and interlaminar bond strengthevolution during thermoplastic matrix composites," *Polymer Composites,* vol. 24, no. 2, pp. 263-278, 2003.

[24] Sonmez F.O., Hahn H.T., "Analysis of the on-line consolidation process in thermoplastic composite tape placement," *Thermoplastic Composite Materials,* vol. 10, no. 6, pp. 543-572, 1997.

[25] Bastien L.J., Gillespie J.W., "A non-isothermal healing model for strength and toughness of fusion bonded joints of amorphous thermoplastics," *Polymer Engineering & Science,* vol. 31, no. 24, pp. 1720-1730, 1991.

[26] Khan M.A., Mitschang P., Schledjewski R., "Identification of some optimal parameters to achieve higher laminate quality through tape placement process," *Advances in Polymer Technology,* vol. 29, no. 2, pp. 98-111, 2010.

[27] Butler C.A., Mccullough R.L., Pitchumani R., Gillespie Jr. J.W., "An analysis of mechanisms governing fusion bonding of thermoplastic composites," *Thermoplastic Composite Materials,* vol. 11, no. 4, pp. 338-363, 1998.

[28] Ageorges C., Ye L., Mai Y.W., Hou M., "Characteristics of resistance welding of lap shear coupons.: Part II. Consolidation," *Composites Part A: Applied Science and Manufacturing,* vol. 29, no. 8, pp. 911-919, 1998.

[29] Schledjewski R., Miaris A., "Thermoplastic tape placement by means of diode laser heating.," in *SAMPE*, Baltimore, 2009.

[30] Stokes Griffin C.M., Compston P., "Investigation of sub-melt temperature bonding of carbon-fiber/PEEK in an automated laser tape placement process," *Composites Part A: Applied Science and Manufacturing,* vol. 84, pp. 17-25, 2016.

[31] Gao S.L., Kim J.K., "Cooling rate influences in carbon fibre/PEEK composites. Part I: Crystallinity and interface adhesion," *Composites Part A: Applied Science and Manufacturing,* vol. 31, no. 6, pp. 517-530, 2000.

[32] Gao S.L., Kim J.K., "Cooling rate influences in carbon fibre/PEEK composites. Part III: impact damage performance," *Composites Part A: Applied Science and Manufacturing,* vol. 32, no. 6, pp. 775-785, 2001.

[33] Gao S.L., Kim J.K., "Cooling rate influences in carbon fibre/PEEK composites. Part II: interlaminar fracture toughness," *Composites Part A: Applied Science and Manufacturing,* vol. 32, no. 6, pp. 763-774, 2001.

[34] Kumar S., Anderson D.P., Adams W.W., "Crystallization and morphology of poly(aryl-ether-ether-ketone)," *Polymer,* vol. 27, no. 3, pp. 329-336, 1986.

[35] Fazil O. Sonmez, H. Thomas Hahn, "Analysis of the On-Line Consolidation Process in Thermoplastic Composite Tape Placement," *Journal of Thermoplastic Composite Materials,* vol. 10, 1997.

[36] Ranganathan S., Advani S.G., Lamontia M.A., "A non-isothermal process model for consolidation and void reduction during in-situ tow placement of thermoplastic composites," *Composite Materials,* vol. 20, no. 8, pp. 1040-1062, 1995.

[37] Tierney J., Gillespie Jr. J.W., "Modeling of heat transfer and void dynamics for the thermoplastic composite tow-placement process," *Composite Materials,* vol. 37, no. 19, pp. 1745-1768, 2003.

[38] Lamontia M.A., Gruber M.B., Tierney J.J., Gillespie Jr. J.W., Jensen B.J., Cano R.J., "Modelling the accudyne thermoplastic in situ ATP process," in *SAMPE*, Paris, 2009.

[39] Mark B. Gruber, Ira Z. Lockwood, Tracy L. Dolan, Steven B. Funck, John J. Tierney, Pavel Simacek, John W. Gillespie, Jr., Suresh G. Advani, Brian J. Jensen, Roberto J. Cano, Brian W. Grimsley, "Thermoplastic In-Situ Placement Requires Better Impregnated Tapes And Tows," 2009.

[40] A.J. Comer, D. Ray, W.O. Obande, D. Jones, J. Lyons, I. Rosca, R.M. O' Higgins, M.A. McCarthy, "Mechanical characterisation of carbon fibre–PEEK manufactured by laser-assisted automated-tape-placement and autoclave," *Composites Part A: Applied Science and Manufacturing,* vol. 69, pp. 10-20, 2015.

[41] Biggs L., Laser processing of Polyetheretherketone, Newark, Delware: Senior Thesis, University of Delware, 1986.

[42] Eric Beyeler, Walter Philips, Selçuk Güçeri, "Experimental Investigation of Laser-Assisted Thermoplastic Consolidation," *Thermoplastic Composite Materials,* pp. 107-121, 1988.

[43] Agarwal V.,Güçeri S.I., McCullough R.L., Schultz J.M., "Thermal Characterization of the Laser-Assisted Consolidation Process," *Thermoplastic Composite Materials,* vol. 5, 1992.

[44] Francesco Rosselli, Michael H. Santarea and Selcuk. I. Guceri, "Effects of processing on laser assisted thermoplastic tape consolidation," Department of Mechanical Engineering (M/C 251), University of Illinois, Chicago; 1997 Elsevier Science Limited., Chicago, 1997.

[45] A.J. Comer, D. Ray, W.O. Obande, D. Jones, J. Lyons, I. Rosca, R.M. O' Higgins, M.A. McCarthy, "Mechanical characterisation of carbon fibre–PEEK manufactured by laser-assisted automated-tape-placement and autoclave," *Composites Part A: Applied Science and Manufacturing,* vol. 69, pp. 10-20, 2014.

[46] Stokes-Griffin CM.J., Compston P., "The effect of processing temperature and placement rate on the short beam strength of carbon fibre–PEEK manufactured using a laser tape placement process," *Composites Part A: Applied Science and Manufacturing,* vol. 78, pp. 274-283, 2015.

[47] Day M., Cooney JD., Wiles DM., "The thermal stability of poly (aryl-ether–ether-ketone) as assessed by thermogravimetry," *Applied Polymer Science,* vol. 38, no. 2, pp. 323-337, 1989.

[48] Rosselli F., Santare MH., "Comparison of the short beam shear (SBS) and interlaminar shear device (ISD) tests," *Composites Part A: Applied Science and Manufactuirng,* vol. 28, no. 6, pp. 587-594, 1997.

[49] Bush A., "NEWS," Automated Dynamics: Performance in Composites, 26 October 2015. [Online]. Available: http://www.automateddynamics.com/2015/company-news/automated-dynamics-brings-laser-heating-system-to-lift. [Accessed 20 October 2017].

[50] Parr A., Hydraulics And Pneumatics: A technicians's and engineer's guide, Oxford, London: Butterworth-Heinemann Ltd, 1991.

[51] Eimanlou M., Hojjati M., "Automated Fiber Placement of Thermoplastic Composite Using Fiber Lasers," in *Proceedings 3rd International Symposium on Automated Composites Manufacturing*, Montreal, 2017.

[52] Eimanlou M., Hojjati M., "Effect of process parameters on mechanical properties of thermoplastic composite rings manufactured by laser-assisted fiber placement," in *In CANCOM 2017 – Canadian International Conference On Composite Materials*, Ottawa, 2017.

[53] Roy R.K., "Design of experiments using the taguchi approach: 16 steps to product and process improvement," John Wiley & Sons, 2001, pp. 110-133.

[54] Condra L., "Value added manufactuirng with design of experiments," Springer Science & Business Media, 2012, pp. 62-85.

[55] Holoeye Inc., "Diffractive Optics," 08 April 2004. [Online]. Available: https://holoeye.com/diffractive-optics/. [Accessed 20 June 2017].

[56] Grigoruants A.G., Basics of Laser Material Processing, Moscow: Mir Publishers, 1994.

[57] Willstrand O., "Intensity distribution conversion from Gaussian to Top-Hat in a single-mode fiber connector," Lund University, Lund, Sweden, 2013.

[58] "www.omega.com," Omega, [Online]. Available: https://www.omega.com/Manuals/manualpdf/M5048.pdf. [Accessed 20 November 2017].

[59] "Thermocouple Response Time," Omega, [Online]. Available: https://www.omega.com/techref/ThermocoupleResponseTime.html. [Accessed 20 November 2017].

APPENDIX A: MICROCONTROLLER CODE

```
//libraries
#include <Keypad.h>
#include <Wire.h>
#include <LCD.h>
#include <LiquidCrystal_I2C.h>
#define I2C_ADDR  0x3F // Add I2C address here
#define BACKLIGHT_PIN  3
#define En_pin  2
#define Rw_pin  1
#define Rs_pin  0
#define D4_pin  4
#define D5_pin  5
#define D6_pin  6
#define D7_pin  7
//initialize LCDI2C
LiquidCrystal_I2C
lcd(I2C_ADDR,En_pin,Rw_pin,Rs_pin,D4_pin,D5_pin,D6_pin,D7_pin);
//initialize keypad
const byte ROWS = 4; //four rows
const byte COLS = 4; //four columns
char keys[ROWS][COLS] =
 {{'1','2','3','A'},
  {'4','5','6','B'},
  {'7','8','9','C'},
  {'*','0','#','D'}};
byte rowPins[ROWS] = {42, 44, 46, 48}; //connect to the row pinouts of the
keypad
byte colPins[COLS] = {34, 36, 38, 40}; //connect to the column pinouts of the
keypad
Keypad keypad = Keypad( makeKeymap(keys), rowPins, colPins, ROWS,
COLS );
//variables
int relayMainUp = 51;  //Main actuator UP position relay
int relayMainDown =23; //Main actuator DOWN position relay
int relayClutch = 43;  //Clutch relay
int relaySiren = 39; //Siren relay
int relayMandrel = 35; //Mandrel relay
int relayLaser = 22; //Laser relay
int relayCutter = 27; //Cutter relay
int numberOfLayers ; //Number of carbon fiber layers of the ring
int rpm=10; //calculated based on motor speed
int motorSpeed= 2; //PWM Pulse Width Modulation 0-251
int motorCW = 3; //Logic1 HIGH=5v
int motorCCW = 4; //Logic2 HIGH=5v
void setup() {
  // put your setup code here, to run once:
   //write relay HIGH for no contact
pinMode (relayMainUp, OUTPUT);
pinMode (relayMainDown, OUTPUT);
pinMode (relayClutch, OUTPUT);
pinMode (relaySiren, OUTPUT);
pinMode (relayMandrel, OUTPUT);
pinMode (relayLaser, OUTPUT);
pinMode (relayCutter, OUTPUT);
pinMode (motorSpeed, OUTPUT);
pinMode (motorCW, OUTPUT);
pinMode (motorCCW, OUTPUT);
digitalWrite (relayMainUp, HIGH); //initialize relay off
digitalWrite (relayMainDown, HIGH); //initialize relay off
digitalWrite (relayClutch, HIGH); //initialize relay off
digitalWrite (relaySiren, HIGH); //initialize relay off
digitalWrite (relayMandrel, HIGH); //initialize relay off
digitalWrite (relayLaser, HIGH); //initialize relay off
digitalWrite (relayCutter, HIGH); //initialize relay off
analogWrite (motorSpeed, 0);
Serial.begin (9600); //start serial communication with keypad
//LCDI2C communication
lcd.begin (16,2); // column and rows of the LCD
// Switch on the backlight
lcd.setBacklightPin(BACKLIGHT_PIN,POSITIVE);
//////////Clutch on/off
int Clutch (int x)
{
  if (x==1)
  {
  digitalWrite (relayClutch, LOW); //load clutch
  lcd.clear();
  lcd.home();
  lcd.print ("CLUTCH ON");
delay (5000); //let clutch grip
  }
  else if (x==2)
  {
  digitalWrite (relayClutch, HIGH); //unload clutch
  lcd.clear();
  lcd.home();
  lcd.print ("CLUTCH OFF");
  delay (5000); //let clutch grip
  }
}
////////// Siren
int Beep (int x)
{
  for (int i=0; i<x; i++)
  {
  digitalWrite (relaySiren, LOW); //ring Siren once
  delay(250);
  digitalWrite (relaySiren, HIGH); // shut it
  delay (100);
  }
}
//////////Mandrel on/off
int Mandrel(int x)
{
  if (x==1)
  {
  lcd.clear();
  lcd.home();
  lcd.print ("MOTOR ON");
  delay (5000);
  digitalWrite (relayMandrel, LOW);
  analogWrite (motorSpeed, 251); //number should be an input from user
  digitalWrite (motorCW, LOW);
  digitalWrite (motorCCW, HIGH);
  }
  else if (x==2)
  {
  digitalWrite (relayMandrel, HIGH); //turn motor off
  analogWrite (motorSpeed, 0); //cut voltage
  digitalWrite (motorCW, LOW);
  digitalWrite (motorCCW, LOW);
  lcd.clear();
  lcd.home();
  lcd.print ("MOTOR OFF");
  }
}
//////////Laser on/off
int Laser (int x)
{
  if (x==1)
  {
  digitalWrite (relayLaser, LOW);
  lcd.setCursor (0,1);
  lcd.print ("LASER ON");
  }
  else if (x==2)
  {
  digitalWrite (relayLaser, HIGH);
  lcd.setCursor (0,1);
  lcd.print ("LASER OFF");
```

```
lcd.setBacklight(HIGH);
lcd.home (); // go home
}
//functions
//////////////Get Number
int get_number_Keypad (void)
{
  int number =0;
 int count = 0;
 char key = keypad.getKey();
 while (1){
   key = keypad.getKey();
   if (key>= '0' && key <='9')
 {
   lcd.setCursor(count,1);
   lcd.print (key);
   number = number *10 + ((key && 0x0f));
   count ++;
 }
 else {
   if(key=='#'){
   lcd.setCursor(count,1);
   lcd.print (key);
   delay (1000);
 return number;
 }
 }
 }
}
////////////// Actuator Down
int MainActuator(int x)
{
 if (x==1)
 {
 digitalWrite (relayMainDown, LOW); // toggle solenoid main actuator to
down stroke
 delay (50);
 digitalWrite (relayMainDown, HIGH); // main actuator is at low position
 delay(50);
 lcd.clear();
 lcd.home();
 lcd.print ("ACTUATOR DOWN");
 delay(5000);
 }
 else if (x==2)
 {
 digitalWrite (relayMainUp, LOW); // toggle solenoid main actuator to down
stroke
 delay (50);
 digitalWrite (relayMainUp, HIGH); // main actuator is at low position
 delay(50);
 lcd.clear();
 lcd.home();
 lcd.print ("ACTUATOR UP");
 delay(5000);
 }
}
```

```
 }
}
//////////Cut
void Cut()
{
 digitalWrite (relayCutter, LOW); //cut tape
 delay (500);
 digitalWrite (relayCutter, HIGH);
}
////////////// RUN
void Run()
{
 MainActuator (1); //turn actuator on
 Clutch (1); //turn clutch on
 Beep(3); //beep 3 times
 Mandrel(1); //turn mandrel on
 Laser(1); //turn laser on
 lcd.clear();
 lcd.home ();
 lcd.print ("RUNNING");
 lcd.setCursor (0,1);
 lcd.print("RPM:");
 lcd.setCursor (4,1);
 lcd.print(rpm);
 delay((numberOfLayers*60000)/rpm); //operation time
 Cut();
 Mandrel(2);
 Laser(2);
 Clutch(2);
 Beep(2);
 MainActuator(2);
}
//////////////Main Loop/////////////////
void loop() {
 // put your main code here, to run repetitively:
 MainActuator(2);
 lcd.clear();
 lcd.home();
 lcd.print("Enter#ofLayers:");
 numberOfLayers = get_number_Keypad ();
 Serial.end();
 lcd.clear();
 lcd.home();
 lcd.print ("RUNNING IN 20A SEC");
 delay(20000);
 Run();
 Serial.begin(9600);
}
```

APPENDIX B: PHOTO MICROGRAPH

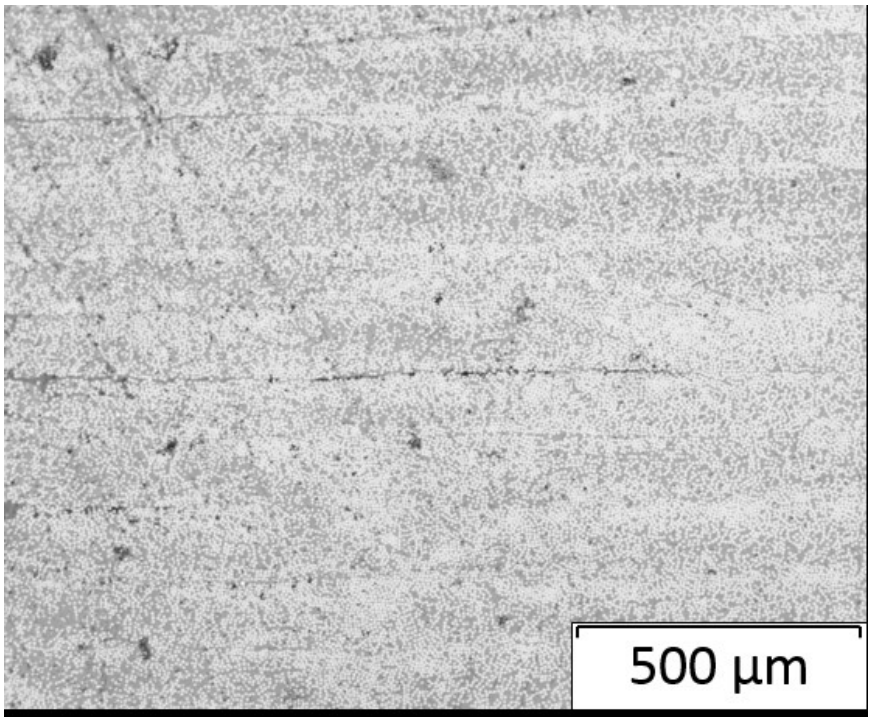

Photo Micrograph Trial 1 – 89 mm/s – 200W – Inter-Laminar Failure

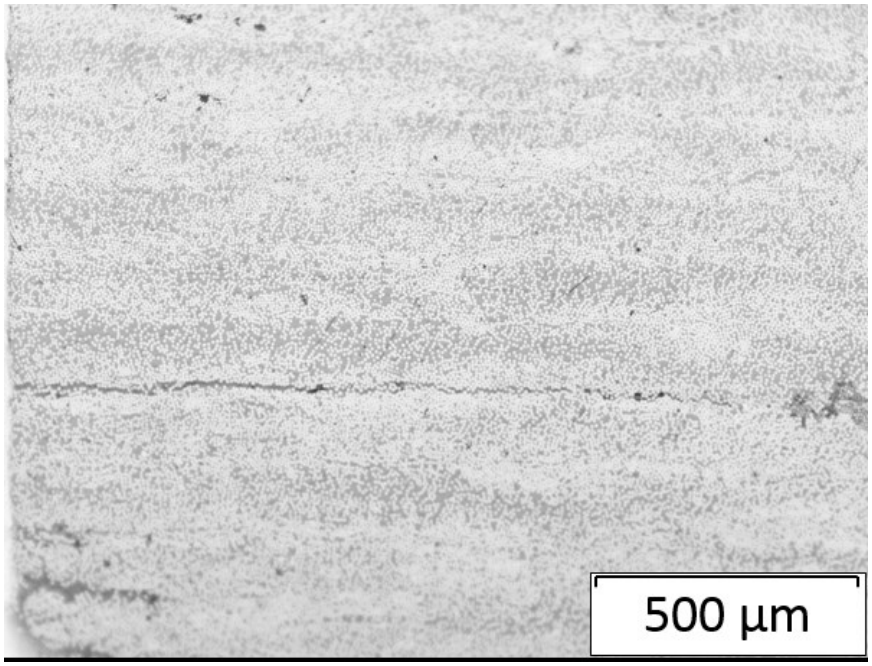

Photo Micrograph Trial 5 – 102 mm/s – 200W – Inter-Laminar Failure

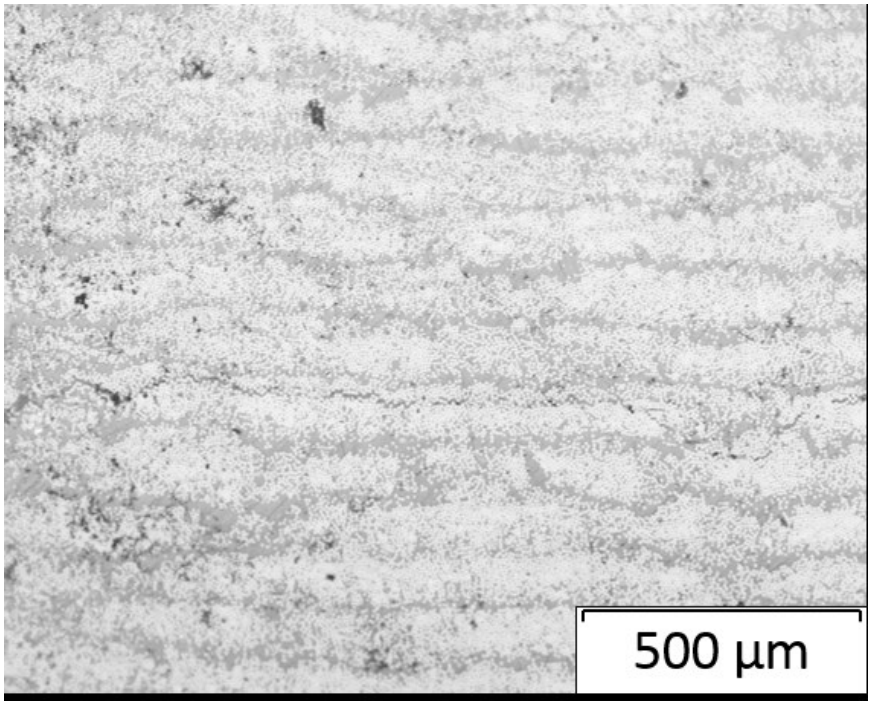

Photo Micrograph Trial 8- 102 mm/s - 220W – Intra-laminar Failure

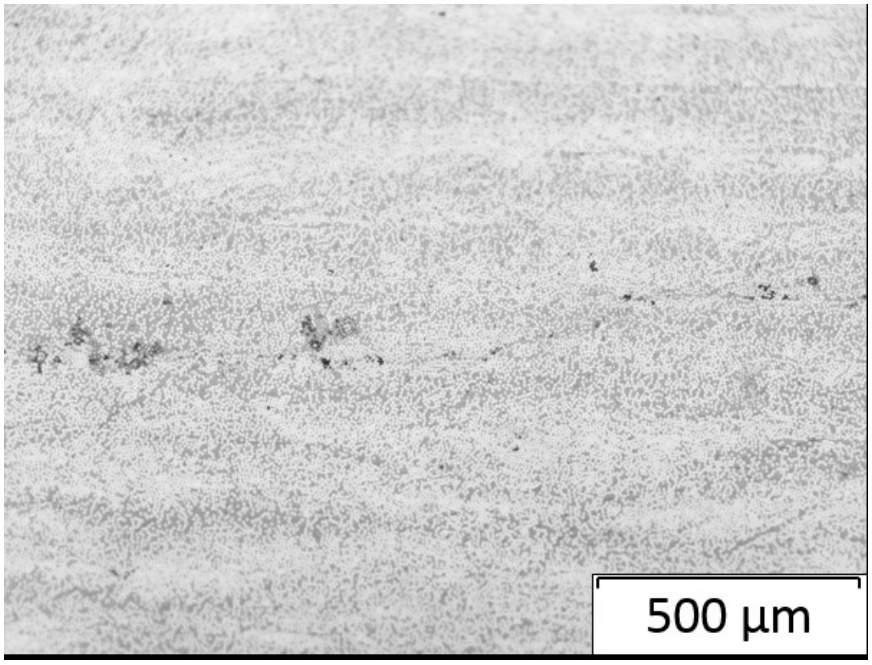

Photo Micrograph Trial 14- 127 mm/s - 270W – Inter-laminar Failure

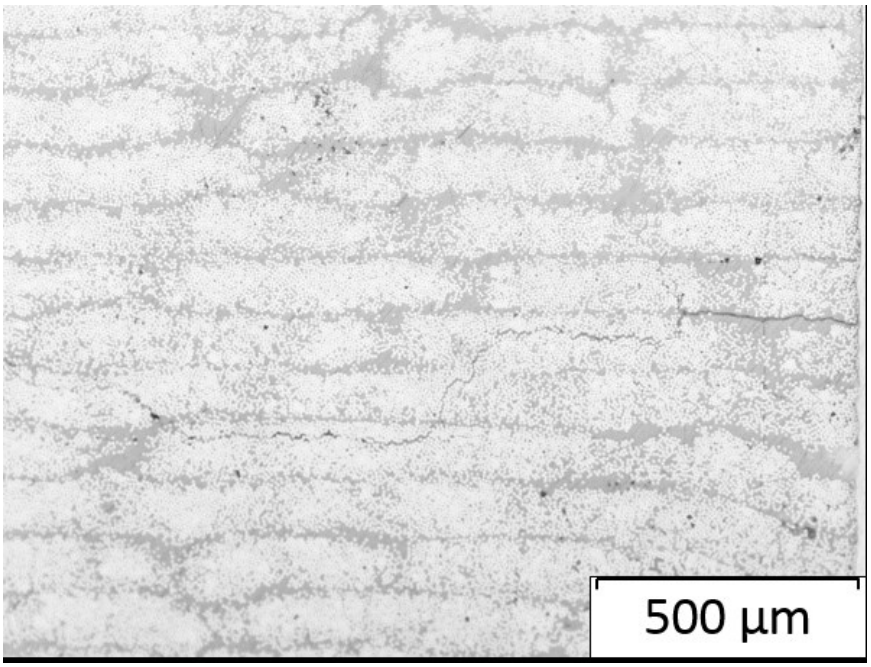

Photo Micrograph Trial 15- 127 mm/s - 280W – Intra-laminar Failure

APPENDIX C: SPECTROPHOTOMETRY RESULT

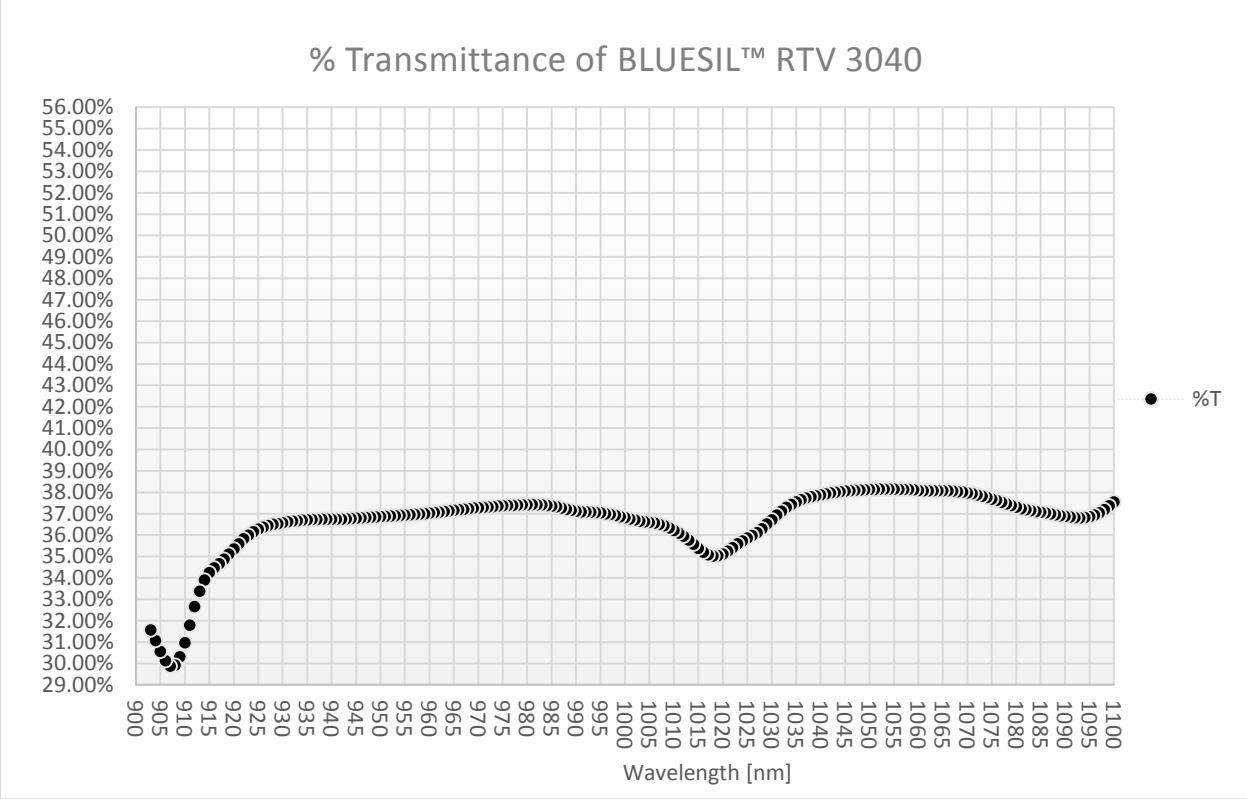

whereas absorbance = log(100/%T)

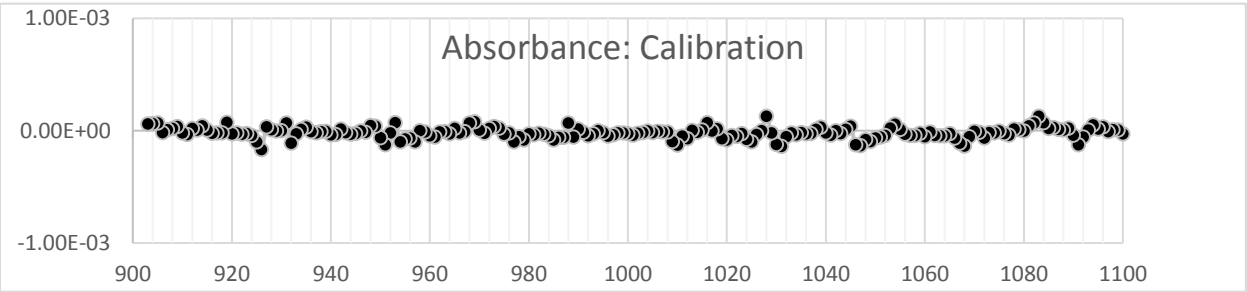

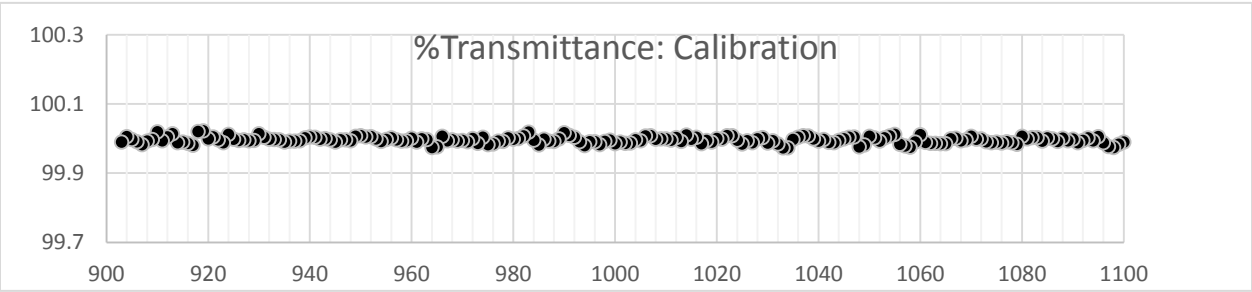

APPENDIX D: LIST OF ITEMS MADE AVAILABLE THROUGH CLOUD STORAGE

CAD FILES:

https://drive.google.com/drive/folders/0B_FlGilmib9xSjVSbzdUaExRNUU?usp=sharing

FINAL DRAWING PACKAGE:

https://drive.google.com/file/d/1hdSwm7hos9jfWIZwk9bTiEvzZg642PHp/view?usp=sharing

EXPERIMENTAL INVESTIGATION DATA:

Sample Tracker Spreadsheet:

https://drive.google.com/file/d/0B_FlGilmib9xWHFCbDJ0YVJvQjQ/view?usp=sharing

SBS Data:

https://drive.google.com/file/d/0B_FlGilmib9xV203emxzVHBVU0U/view?usp=sharing

Force-Displacement Plots:

https://drive.google.com/file/d/0B_FlGilmib9xNUk0LVBUX3FFRFk/view?usp=sharing

Thermocouples Data:

https://drive.google.com/drive/folders/1-DZNU_USdMHqGCOmTPbDvIlKKbBw_XSM?usp=sharing

Spectrometer Data:

https://drive.google.com/drive/folders/0B_FlGilmib9xb2VvVFJILWdCN3c?usp=sharing

Load Cell Transducer Data:

https://drive.google.com/drive/folders/0B_FlGilmib9xeXBqbmxvQ3gxWFk?usp=sharing

LASER LAB SAFETY DOCUMENTS: SOP 2016

https://drive.google.com/file/d/0B_FlGilmib9xWUhzdmFGMi1xY1VCYmhzak90bXdYZERVZjJv/view?usp=sharing

LASER OPERATOR CHECK LIST:

https://drive.google.com/file/d/0B_FlGilmib9xaUlidlZkcDRqSkk/view?usp=sharing